

Bulk Properties of the Medium Produced in Relativistic Heavy-Ion Collisions from the Beam Energy Scan Program

L. Adamczyk,¹ J. K. Adkins,¹⁹ G. Agakishiev,¹⁷ M. M. Aggarwal,³¹ Z. Ahammed,⁵⁰ N. N. Ajitanand,⁴⁰ I. Alekseev,^{15,26} D. M. Anderson,⁴² R. Aoyama,⁴⁶ A. Aparin,¹⁷ D. Arkhipkin,³ E. C. Aschenauer,³ M. U. Ashraf,⁴⁵ A. Attri,³¹ G. S. Averichev,¹⁷ X. Bai,⁷ V. Bairathi,²⁷ A. Behera,⁴⁰ R. Bellwied,⁴⁴ A. Bhasin,¹⁶ A. K. Bhati,³¹ P. Bhattarai,⁴³ J. Bielcik,¹⁰ J. Bielcikova,¹¹ L. C. Bland,³ I. G. Bordyuzhin,¹⁵ J. Bouchet,¹⁸ J. D. Brandenburg,³⁶ A. V. Brandin,²⁶ D. Brown,²³ I. Bunzarov,¹⁷ J. Butterworth,³⁶ H. Caines,⁵⁴ M. Calderón de la Barca Sánchez,⁵ J. M. Campbell,²⁹ D. Cebra,⁵ I. Chakaberia,³ P. Chaloupka,¹⁰ Z. Chang,⁴² N. Chankova-Bunzarova,¹⁷ A. Chatterjee,⁵⁰ S. Chattopadhyay,⁵⁰ X. Chen,³⁷ J. H. Chen,³⁹ X. Chen,²¹ J. Cheng,⁴⁵ M. Cherney,⁹ W. Christie,³ G. Contin,²² H. J. Crawford,⁴ S. Das,⁷ L. C. De Silva,⁹ R. R. Debbé,³ T. G. Dedovich,¹⁷ J. Deng,³⁸ A. A. Derevschikov,³³ L. Didenko,³ C. Dilks,³² X. Dong,²² J. L. Drachenberg,²⁰ J. E. Draper,⁵ L. E. Dunkelberger,⁶ J. C. Dunlop,³ L. G. Efimov,¹⁷ N. Elsey,⁵² J. Engelage,⁴ G. Eppley,³⁶ R. Esha,⁶ S. Esumi,⁴⁶ O. Evdokimov,⁸ J. Ewigleben,²³ O. Eyser,³ R. Fatemi,¹⁹ S. Fazio,³ P. Federic,¹¹ P. Federicova,¹⁰ J. Fedorisin,¹⁷ Z. Feng,⁷ P. Filip,¹⁷ E. Finch,⁴⁷ Y. Fisyak,³ C. E. Flores,⁵ L. Fulek,¹ C. A. Gagliardi,⁴² D. Garand,³⁴ F. Geurts,³⁶ A. Gibson,⁴⁹ M. Girard,⁵¹ D. Grosnick,⁴⁹ D. S. Gunarathne,⁴¹ Y. Guo,¹⁸ A. Gupta,¹⁶ S. Gupta,¹⁶ W. Guryn,³ A. I. Hamad,¹⁸ A. Hamed,⁴² A. Harlenderova,¹⁰ J. W. Harris,⁵⁴ L. He,³⁴ S. Heppelmann,³² S. Heppelmann,⁵ A. Hirsch,³⁴ G. W. Hoffmann,⁴³ S. Horvat,⁵⁴ T. Huang,²⁸ B. Huang,⁸ X. Huang,⁴⁵ H. Z. Huang,⁶ T. J. Humanic,²⁹ P. Huo,⁴⁰ G. Igo,⁶ W. W. Jacobs,¹⁴ A. Jentsch,⁴³ J. Jia,^{3,40} K. Jiang,³⁷ S. Jowzaee,⁵² E. G. Judd,⁴ S. Kabana,¹⁸ D. Kalinkin,¹⁴ K. Kang,⁴⁵ K. Kauder,⁵² H. W. Ke,³ D. Keane,¹⁸ A. Kechechyan,¹⁷ Z. Khan,⁸ D. P. Kikola,⁵¹ I. Kisel,¹² A. Kisiel,⁵¹ L. Kochenda,²⁶ M. Kocmanek,¹¹ T. Kollegger,¹² L. K. Kosarzewski,⁵¹ A. F. Kraishan,⁴¹ P. Kravtsov,²⁶ K. Krueger,² N. Kulathunga,⁴⁴ L. Kumar,³¹ J. Kvapil,¹⁰ J. H. Kwasizur,¹⁴ R. Lacey,⁴⁰ J. M. Landgraf,³ K. D. Landry,⁶ J. Lauret,³ A. Lebedev,³ R. Lednicky,¹⁷ J. H. Lee,³ X. Li,³⁷ C. Li,³⁷ W. Li,³⁹ Y. Li,⁴⁵ J. Lidrych,¹⁰ T. Lin,¹⁴ M. A. Lisa,²⁹ H. Liu,¹⁴ P. Liu,⁴⁰ Y. Liu,⁴² F. Liu,⁷ T. Ljubicic,³ W. J. Llope,⁵² M. Lomnitz,²² R. S. Longacre,³ S. Luo,⁸ X. Luo,⁷ G. L. Ma,³⁹ L. Ma,³⁹ Y. G. Ma,³⁹ R. Ma,³ N. Magdy,⁴⁰ R. Majka,⁵⁴ D. Mallick,²⁷ S. Margetis,¹⁸ C. Markert,⁴³ H. S. Matis,²² K. Meehan,⁵ J. C. Mei,³⁸ Z. W. Miller,⁸ N. G. Minaev,³³ S. Mioduszewski,⁴² D. Mishra,²⁷ S. Mizuno,²² B. Mohanty,²⁷ M. M. Mondal,¹³ D. A. Morozov,³³ M. K. Mustafa,²² Md. Nasim,⁶ T. K. Nayak,⁵⁰ J. M. Nelson,⁴ M. Nie,³⁹ G. Nigmatkulov,²⁶ T. Niida,⁵² L. V. Nogach,³³ T. Nonaka,⁴⁶ S. B. Nurushev,³³ G. Odyniec,²² A. Ogawa,³ K. Oh,³⁵ V. A. Okorokov,²⁶ D. Olivett Jr.,⁴¹ B. S. Page,³ R. Pak,³ Y. Pandit,⁸ Y. Panebratsev,¹⁷ B. Pawlik,³⁰ H. Pei,⁷ C. Perkins,⁴ P. Pile,³ J. Pluta,⁵¹ K. Poniatowska,⁵¹ J. Porter,²² M. Posik,⁴¹ A. M. Poskanzer,²² N. K. Pruthi,³¹ M. Przybycien,¹ J. Putschke,⁵² H. Qiu,³⁴ A. Quintero,⁴¹ S. Ramachandran,¹⁹ R. L. Ray,⁴³ R. Reed,²³ M. J. Rehbein,⁹ H. G. Ritter,²² J. B. Roberts,³⁶ O. V. Rogachevskiy,¹⁷ J. L. Romero,⁵ J. D. Roth,⁹ L. Ruan,³ J. Rusnak,¹¹ O. Rusnakova,¹⁰ N. R. Sahoo,⁴² P. K. Sahu,¹³ S. Salur,²² J. Sandweiss,⁵⁴ M. Saur,¹¹ J. Schambach,⁴³ A. M. Schmah,²² W. B. Schmidke,³ N. Schmitz,²⁴ B. R. Schweid,⁴⁰ J. Seger,⁹ M. Sergeeva,⁶ P. Seyboth,²⁴ N. Shah,³⁹ E. Shahaliev,¹⁷ P. V. Shanmuganathan,²³ M. Shao,³⁷ A. Sharma,¹⁶ M. K. Sharma,¹⁶ W. Q. Shen,³⁹ Z. Shi,²² S. S. Shi,⁷ Q. Y. Shou,³⁹ E. P. Sichtermann,²² R. Sikora,¹ M. Simko,¹¹ S. Singha,¹⁸ M. J. Skoby,¹⁴ N. Smirnov,⁵⁴ D. Smirnov,³ W. Solyst,¹⁴ L. Song,⁴⁴ P. Sorensen,³ H. M. Spinka,² B. Srivastava,³⁴ T. D. S. Stanislaus,⁴⁹ M. Strikhanov,²⁶ B. Stringfellow,³⁴ T. Sugiura,⁴⁶ M. Sumner,¹¹ B. Summa,³² Y. Sun,³⁷ X. M. Sun,⁷ X. Sun,⁷ B. Surrow,⁴¹ D. N. Svirida,¹⁵ A. H. Tang,³ Z. Tang,³⁷ A. Taranenko,²⁶ T. Tarnowsky,²⁵ A. Tawfik,⁵³ J. Thäder,²² J. H. Thomas,²² A. R. Timmins,⁴⁴ D. Tlusty,³⁶ T. Todoroki,³ M. Tokarev,¹⁷ S. Trentalange,⁶ R. E. Tribble,⁴² P. Tribedy,³ S. K. Tripathy,¹³ B. A. Trzeciak,¹⁰ O. D. Tsai,⁶ T. Ullrich,³ D. G. Underwood,² I. Upsal,²⁹ G. Van Buren,³ G. van Nieuwenhuizen,³ A. N. Vasiliev,³³ F. Videbæk,³ S. Vokal,¹⁷ S. A. Voloshin,⁵² A. Vossen,¹⁴ G. Wang,⁶ Y. Wang,⁷ F. Wang,³⁴ Y. Wang,⁴⁵ J. C. Webb,³ G. Webb,³ L. Wen,⁶ G. D. Westfall,²⁵ H. Wieman,²² S. W. Wissink,¹⁴ R. Witt,⁴⁸ Y. Wu,¹⁸ Z. G. Xiao,⁴⁵ W. Xie,³⁴ G. Xie,³⁷ J. Xu,⁷ N. Xu,²² Q. H. Xu,³⁸ Y. F. Xu,³⁹ Z. Xu,³ Y. Yang,²⁸ Q. Yang,³⁷ C. Yang,³⁸ S. Yang,³ Z. Ye,⁸ Z. Ye,⁸ L. Yi,⁵⁴ K. Yip,³ I. -K. Yoo,³⁵ N. Yu,⁷ H. Zbroszczyk,⁵¹ W. Zha,³⁷ Z. Zhang,³⁹ X. P. Zhang,⁴⁵ J. B. Zhang,⁷ S. Zhang,³⁷ J. Zhang,²¹ Y. Zhang,³⁷ J. Zhang,²² S. Zhang,³⁹ J. Zhao,³⁴ C. Zhong,³⁹ L. Zhou,³⁷ C. Zhou,³⁹ X. Zhu,⁴⁵ Z. Zhu,³⁸ and M. Zyzak¹²

(STAR Collaboration)

¹AGH University of Science and Technology, FPACS, Cracow 30-059, Poland

²Argonne National Laboratory, Argonne, Illinois 60439

³Brookhaven National Laboratory, Upton, New York 11973

⁴University of California, Berkeley, California 94720

⁵University of California, Davis, California 95616

- ⁶University of California, Los Angeles, California 90095
⁷Central China Normal University, Wuhan, Hubei 430079
⁸University of Illinois at Chicago, Chicago, Illinois 60607
⁹Creighton University, Omaha, Nebraska 68178
¹⁰Czech Technical University in Prague, FNSPE, Prague, 115 19, Czech Republic
¹¹Nuclear Physics Institute AS CR, 250 68 Prague, Czech Republic
¹²Frankfurt Institute for Advanced Studies FIAS, Frankfurt 60438, Germany
¹³Institute of Physics, Bhubaneswar 751005, India
¹⁴Indiana University, Bloomington, Indiana 47408
¹⁵Alikhanov Institute for Theoretical and Experimental Physics, Moscow 117218, Russia
¹⁶University of Jammu, Jammu 180001, India
¹⁷Joint Institute for Nuclear Research, Dubna, 141 980, Russia
¹⁸Kent State University, Kent, Ohio 44242
¹⁹University of Kentucky, Lexington, Kentucky, 40506-0055
²⁰Lamar University, Physics Department, Beaumont, Texas 77710
²¹Institute of Modern Physics, Chinese Academy of Sciences, Lanzhou, Gansu 730000
²²Lawrence Berkeley National Laboratory, Berkeley, California 94720
²³Lehigh University, Bethlehem, PA, 18015
²⁴Max-Planck-Institut für Physik, Munich 80805, Germany
²⁵Michigan State University, East Lansing, Michigan 48824
²⁶National Research Nuclear University MEPhI, Moscow 115409, Russia
²⁷National Institute of Science Education and Research, Bhubaneswar 751005, India
²⁸National Cheng Kung University, Tainan 70101
²⁹Ohio State University, Columbus, Ohio 43210
³⁰Institute of Nuclear Physics PAN, Cracow 31-342, Poland
³¹Panjab University, Chandigarh 160014, India
³²Pennsylvania State University, University Park, Pennsylvania 16802
³³Institute of High Energy Physics, Protvino 142281, Russia
³⁴Purdue University, West Lafayette, Indiana 47907
³⁵Pusan National University, Pusan 46241, Korea
³⁶Rice University, Houston, Texas 77251
³⁷University of Science and Technology of China, Hefei, Anhui 230026
³⁸Shandong University, Jinan, Shandong 250100
³⁹Shanghai Institute of Applied Physics, Chinese Academy of Sciences, Shanghai 201800
⁴⁰State University Of New York, Stony Brook, NY 11794
⁴¹Temple University, Philadelphia, Pennsylvania 19122
⁴²Texas A&M University, College Station, Texas 77843
⁴³University of Texas, Austin, Texas 78712
⁴⁴University of Houston, Houston, Texas 77204
⁴⁵Tsinghua University, Beijing 100084
⁴⁶University of Tsukuba, Tsukuba, Ibaraki, Japan,
⁴⁷Southern Connecticut State University, New Haven, CT, 06515
⁴⁸United States Naval Academy, Annapolis, Maryland, 21402
⁴⁹Valparaiso University, Valparaiso, Indiana 46383
⁵⁰Variable Energy Cyclotron Centre, Kolkata 700064, India
⁵¹Warsaw University of Technology, Warsaw 00-661, Poland
⁵²Wayne State University, Detroit, Michigan 48201
⁵³World Laboratory for Cosmology and Particle Physics (WLCAPP), Cairo 11571, Egypt
⁵⁴Yale University, New Haven, Connecticut 06520

We present measurements of bulk properties of the matter produced in Au+Au collisions at $\sqrt{s_{NN}} = 7.7, 11.5, 19.6, 27,$ and 39 GeV using identified hadrons (π^\pm, K^\pm, p and \bar{p}) from the STAR experiment in the Beam Energy Scan (BES) Program at the Relativistic Heavy Ion Collider (RHIC). Midrapidity ($|y| < 0.1$) results for multiplicity densities dN/dy , average transverse momenta $\langle p_T \rangle$ and particle ratios are presented. The chemical and kinetic freeze-out dynamics at these energies are discussed and presented as a function of collision centrality and energy. These results constitute the systematic measurements of bulk properties of matter formed in heavy-ion collisions over a broad range of energy (or baryon chemical potential) at RHIC.

PACS numbers: 25.75.Gz, 25.75.Nq, 25.75.-q, 25.75.Dw

I. INTRODUCTION

Exploring the Quantum Chromodynamics (QCD) phase diagram is one important goal of high-energy

heavy-ion collision experiments [1–4]. The QCD phase diagram is usually plotted as temperature (T) versus

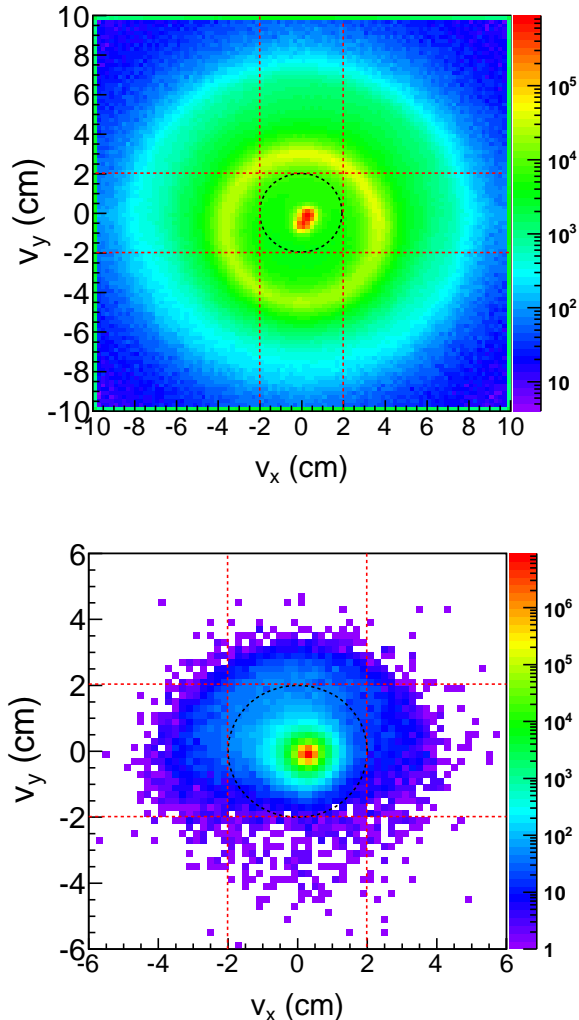


FIG. 1: The x and y positions of the reconstructed event vertices in Au+Au collisions at $\sqrt{s_{NN}} = 7.7$ (top panel) and 39 GeV (bottom panel). The events involving beam-pipe interactions are rejected by applying a cut of less than 2 cm on the transverse radial position of the event vertex. See text for more details.

baryon chemical potential (μ_B). Assuming a thermalized system is created in heavy-ion collisions, both of these quantities can be varied by changing the collision energy [5–7]. Theory suggests that the phase diagram includes a possible transition from a high energy density and high temperature phase called Quark Gluon Plasma (QGP) phase, dominated by partonic degrees of freedom, to a phase where the relevant degrees of freedom are hadronic [8–10]. Several observations at the top RHIC energy i.e. at $\sqrt{s_{NN}} = 200$ GeV have been associated with the existence of a phase with partonic degrees of freedom in the early stages of heavy-ion collisions [1–4, 11–16]. Examples of such observations include the suppression of high transverse momentum (p_T) hadron production in Au+Au collisions relative to scaled $p+p$ collisions [1–4, 11–14], large elliptic flow (v_2) for hadrons

with light, as well as heavier strange valence quarks, and differences between baryon and meson v_2 at intermediate p_T in Au+Au collisions [17].

Lattice QCD calculations indicate that a system produced at $\mu_B = 0$ MeV evolves through a rapid crossover at the parton-hadron phase transition [18, 19]. Calculations from lattice QCD [20] and from several QCD-based models [21–24] suggest that for a system created in collisions corresponding to larger values of μ_B , the transition is first order. The point in the (T, μ_B) plane where the first order phase transition ends, is the QCD critical point [25, 26]. Searching for the critical point and phase boundary in the QCD phase diagram is currently a focus of experimental and theoretical nuclear physics research. To this end, RHIC has undertaken the first phase of the BES Program [27–31]. The idea is to vary the collision energy, thereby scanning the phase diagram from the top RHIC energy (lower μ_B) to the lowest possible energy (higher μ_B), to look for the signatures of the QCD phase boundary and the QCD critical point. To look for the phase boundary, we study the established signatures of the QGP formation at 200 GeV as a function of beam energy. Turn-off of these signatures at a particular energy would suggest that a partonic medium is no longer formed at that energy. Near the critical point, there would be enhanced fluctuations in multiplicity distributions of conserved quantities (net-charge, net-baryon number, and net-strangeness) [32–35]. These observables would suggest the existence of a critical point if they were to show large fluctuations or divergence from a baseline in a limited collision energy region. However, before looking for these signatures, it is important to know the (T, μ_B) region of the phase diagram we can access. The spectra of produced particles and their yield ratios allow us to infer the T and μ_B values at freeze-out. In addition, bulk properties such as dN/dy , $\langle p_T \rangle$, particle ratios, and freeze-out properties may provide insight into the particle production mechanisms at these energies. The systematic study of these bulk properties may reveal the evolution and change in behavior of the system formed in heavy-ion collisions as a function of collision energy.

II. EXPERIMENT AND DATA ANALYSIS

A. STAR experiment

The results presented here are based on data taken with the STAR experiment [36] in Au+Au collisions at $\sqrt{s_{NN}} = 7.7, 11.5, 19.6, 27$ and 39 GeV. The 7.7, 11.5 and 39 GeV data were collected in the year 2010, while the 19.6 and 27 GeV data were collected in the year 2011. These data sets were taken with a minimum bias trigger, which was defined using a coincidence of hits in the zero degree calorimeters (ZDCs) [37], vertex position detectors (VPDs) [38], and/or beam-beam counters (BBCs) [39, 40].

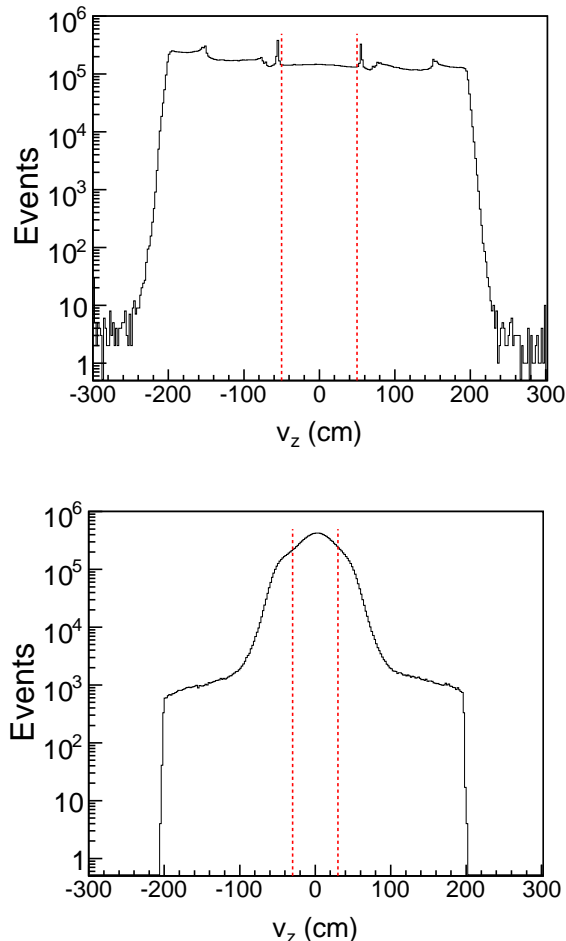


FIG. 2: Distributions of the z -position of the reconstructed primary vertex (V_z) in Au+Au collisions at $\sqrt{s_{NN}} = 7.7$ (top panel) and 39 GeV (bottom panel).

The main detectors used to obtain the results on p_T spectra, yields and particle ratios for charged hadrons are the Time Projection Chamber (TPC) [41] and Time-Of-Flight detectors (TOF) [42]. The TPC is the primary tracking device at STAR. It is 4.2 m long and 4 m in diameter. It covers about ± 1 units of pseudorapidity (η) and the full azimuthal angle. The sensitive volume of the TPC contains P10 gas (10% methane, 90% argon) regulated at 2 mbar above atmospheric pressure. The TPC resides in a nearly constant magnetic field of 0.5 Tesla oriented in the longitudinal (z) direction. The TPC data is used to determine particle trajectories, thereby their momenta, and particle types through ionization energy loss (dE/dx). The TOF is based on Multi-gap Resistive Plate Chamber (MRPC) technology and is used to identify particles at relatively high momenta. The details of the design and other characteristics of the STAR detectors can be found in Ref. [36].

TABLE I: Total number of events analyzed for various energies obtained after all the event selection cuts are applied.

$\sqrt{s_{NN}}$ (GeV)	No. of events (million)
7.7	4
11.5	8
19.6	17.3
27	33
39	111

B. Event Selection

The primary vertex for each event is determined by finding the most probable point of common origin of the tracks measured by the TPC. Figure 1 shows, as examples, the transverse x, y positions of the primary vertices in 7.7 and 39 GeV Au+Au collisions. In order to reject background events which involve interactions with the beam pipe of radius 3.95 cm, the event vertex radius (defined as $\sqrt{V_x^2 + V_y^2}$ where V_x and V_y are the vertex positions along the x and y directions) is required to be within 2 cm of the center of STAR (see Fig. 1). The yellow ring in the top panel of the figure corresponds to collisions between the beam nuclei and the beam pipe. This type of background is more significant in low energy data.

The distributions of the primary vertex position along the longitudinal (beam) direction (V_z) are shown in Fig. 2 for 7.7 (top panel) and 39 GeV (bottom panel). The lower energy vertex distribution is flat near zero while that at 39 GeV is peaked. The wide z -vertex distribution at lower energies is due to the fact that the beams are more difficult to focus at lower energies. The V_z distributions for other BES energies are also flattened relative to higher energies. Only those events which have a V_z within 50 cm of the nominal collision point (center of the detector) are selected for the 7.7 GeV analysis, while for the other data sets, events within 30 cm were selected for the analysis. These values are chosen in order to achieve uniform detector performance and sufficient statistical significance of the measured observables. Table I shows the total number of events that are used for the analysis at each energy after the above-mentioned event selection cuts.

C. Centrality Selection

Centralities in Au+Au collisions at $\sqrt{s_{NN}} = 7.7$ –39 GeV are defined by using the number of primary charged-particle tracks reconstructed in the TPC over the full azimuth and pseudorapidity $|\eta| < 0.5$. This is generally called the “reference multiplicity” in STAR. For each energy, a correction is applied to the standard definition by: removing bad runs, applying acceptance and effi-

TABLE II: The average number of participating nucleons ($\langle N_{\text{part}} \rangle$) for various collision centralities in Au+Au collisions at $\sqrt{s_{NN}} = 7.7\text{--}39$ GeV. The numbers in parentheses represent the uncertainties.

% cross section	$\langle N_{\text{part}} \rangle$				
	7.7 GeV	11.5 GeV	19.6 GeV	27 GeV	39 GeV
0-5	337 (2)	338 (2)	338 (2)	343 (2)	342 (2)
5-10	290 (6)	291 (6)	289 (6)	299 (6)	294 (6)
10-20	226 (8)	226 (8)	225 (9)	234 (9)	230 (9)
20-30	160 (10)	160 (9)	158 (10)	166 (11)	162 (10)
30-40	110 (11)	110 (10)	108 (11)	114 (11)	111 (11)
40-50	72 (10)	73 (10)	71 (10)	75 (10)	74 (10)
50-60	45 (9)	44 (9)	44 (9)	47 (9)	46 (9)
60-70	26 (7)	26 (7)	25 (7)	27 (8)	26 (7)
70-80	14 (4)	14 (6)	14 (5)	14 (6)	14 (5)

TABLE III: Track selection criteria at all energies.

$ y $	DCA	No. of fit points	No. of fit points No. of possible hits	No. of dE/dx points
< 0.1	≤ 3 cm	≥ 25	≥ 0.52	≥ 15

ciency corrections to reference multiplicity for different z -vertex positions, and performing corrections for trigger inefficiencies (only important for low reference multiplicity events) for different z -vertices.

The centrality classes are obtained as fractions of the reference multiplicity distribution. The events are divided into following centrality classes 0–5%, 5–10%, 10–20%, 20–30%, 30–40%, 40–50%, 50–60%, 60–70%, and 70–80%. The mean values of the number of participating nucleons $\langle N_{\text{part}} \rangle$ corresponding to these centrality classes are evaluated using a Glauber model and are given in Table II for various energies. More details on centrality and $\langle N_{\text{part}} \rangle$ values estimations can be found in Refs. [27, 43].

D. Track Selection

Track selection criteria for all analyses are presented in Table III. In order to suppress admixture of tracks from secondary vertices, a requirement of less than 3 cm is placed on the distance of closest approach (DCA) between each track and the event vertex. Tracks must have at least 25 points used in track fitting out of the maximum of 45 hits possible in the TPC. To prevent multiple counting of split tracks, at least 52% of the total possible fit points are required. This is a standard cut in STAR analysis, but does not impose further cut beyond the stricter cut of 25 points implemented for track fitting used here. A condition is placed on the number of dE/dx points used to derive dE/dx values. The results presented here are within rapidity $|y| < 0.1$ and have the

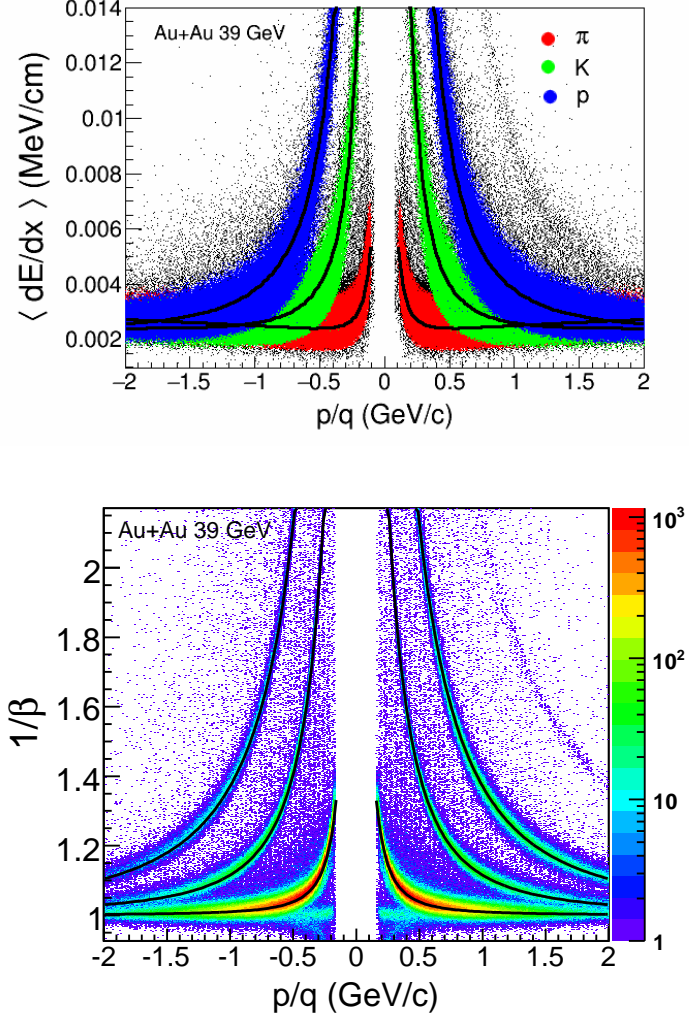


FIG. 3: Top: The $\langle dE/dx \rangle$ of charged tracks at midrapidity ($|y| < 0.1$) plotted as function of rigidity (p/q) in Au+Au collisions at $\sqrt{s_{NN}} = 39$ GeV. The curves represent the $\langle dE/dx \rangle$ of the corresponding particles. The red band corresponds to π^\pm , green corresponds to K^\pm , and blue corresponds to p and \bar{p} . Bottom: $1/\beta$ from TOF vs. rigidity at same energy. The curves, from low to up, show the expected mean values of pions, kaons, and (anti-) protons, respectively.

same track cuts for all energies.

E. Particle Identification

Particle identification is accomplished in the TPC by measuring the dE/dx . Figure 3 (top panel) shows the average dE/dx of measured charged particles plotted as a function of “rigidity” (i.e. momentum/charge) of the particles. The curves represent the Bichsel [44] expectation values. It can be seen that the TPC can identify pions (π^\pm), kaons (K^\pm), and protons (p) and anti-protons

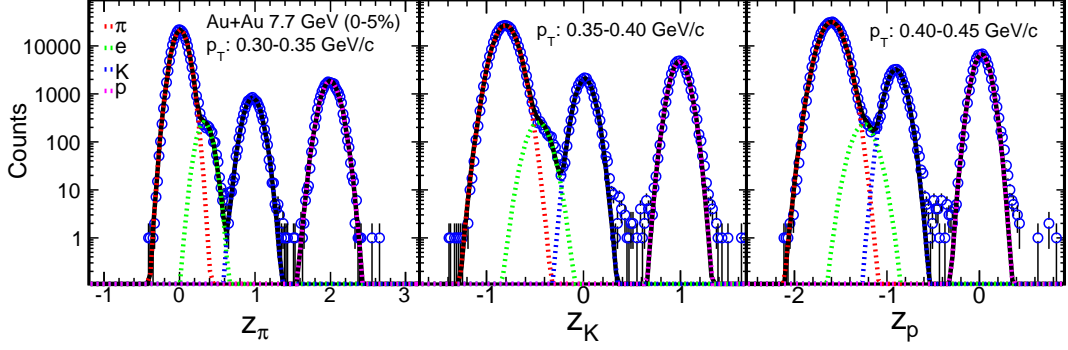


FIG. 4: The z_π , z_K , and z_p distributions for positively charged hadrons (π , K , and p) at midrapidity ($|y| < 0.1$) in the TPC for various p_T ranges in Au+Au collisions at $\sqrt{s_{NN}} = 7.7$ GeV. The curves are Gaussian fits representing contributions from pions (dotted-red), electrons (dotted-green), kaons (dotted-blue), and protons (dotted-magenta). Uncertainties are statistical only.

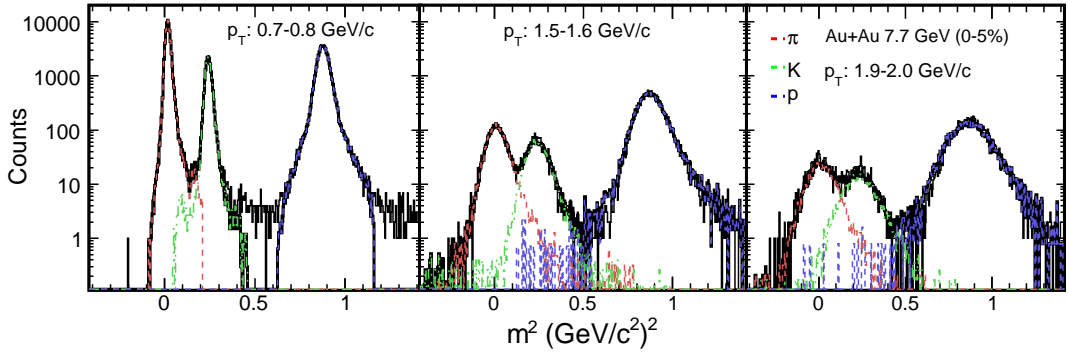


FIG. 5: The m^2 distributions for positively charged hadrons used to extract raw yields for pions, kaons, and protons in $|y| < 0.1$ for Au+Au collisions at 7.7 GeV at three different p_T ranges. The curves are predicted m^2 fits representing contributions from pions (dashed-red), kaons (dashed-green), and protons (dashed-blue).

(\bar{p}) at low momentum as illustrated by the color bands. We note that the color bands are only used for illustration here. The quantitative technique to extract particle yields is discussed in detail later.

For higher momentum, we use time-of-flight information to identify particles. The TOF particle identification for this analysis is used above $p_T = 0.4$ GeV/c. Figure 3 (bottom panel) shows the inverse of particle velocity in unit of the speed of light $1/\beta$, as a function of rigidity. The expectation values for pions, kaons, and protons are shown as the curves. As seen in the figure, there is a band representing $1/\beta < 1$ or $\beta > 1$ at low momentum. This non-physical band is the result of a charged hadron and a photon converted electron hitting in the same TOF cluster. The conversion may happen in the TPC Outer Field Cage or TOF tray box. Due to high occupancy, these TOF hits are accidentally matched to hadron tracks in the TPC, resulting in the wrong time of flight. They have a negligible effect on charged hadron yields.

The $\langle dE/dx \rangle$ distribution for a fixed particle type is not Gaussian [45]. It has been shown that a better Gaussian variable, for a given particle type, is the z -

variable [45], defined as

$$z_X = \ln \left(\frac{\langle dE/dx \rangle}{\langle dE/dx \rangle_X^B} \right) \quad (1)$$

where X is the particle type (e^\pm, π^\pm, K^\pm, p , or \bar{p}) and $\langle dE/dx \rangle_X^B$ is the corresponding Bichsel function [44]. The most probable value of z_X for the particle X is 0.

The z_X distribution is constructed for a given particle type in a given p_T bin within $|y| < 0.1$. Figure 4 shows the z_π , z_K , and z_p distributions for positively charged particles at different p_T bins in central Au+Au collisions at $\sqrt{s_{NN}} = 7.7$ GeV. To extract the raw yields in a given p_T bin, a multi-Gaussian fit is applied to the z_X distributions as shown in Fig. 4. The Gaussian area corresponding to the particle of interest (i.e. the Gaussian with centroid at zero) gives the yield of that particle in the given p_T bin. At low p_T , the peaks of pion, kaon, and proton distributions are well separated. However, at higher p_T these distributions start to overlap. In the overlap p_T region, the sigma of the Gaussian fits are constrained by the values from the lower p_T bins. Further details on extraction of raw yields for identified hadrons

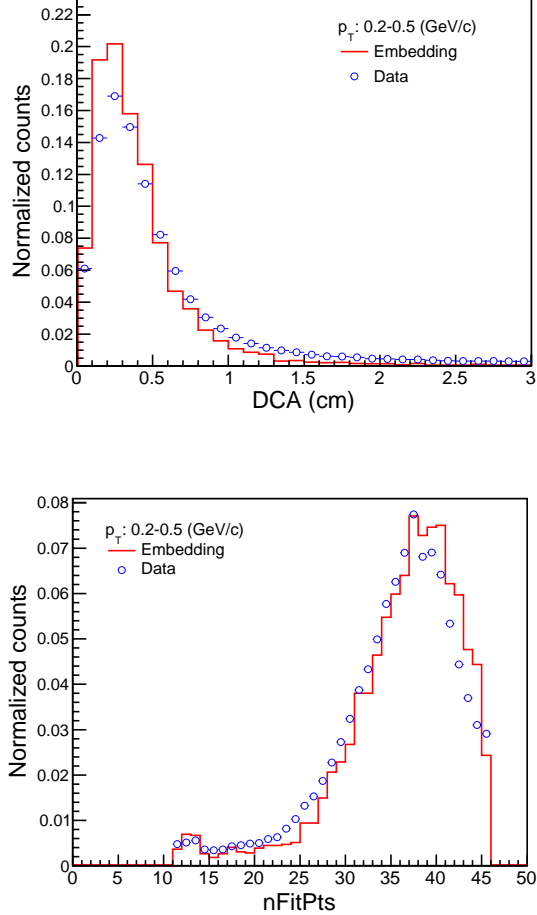


FIG. 6: Top: Distribution of distance of closest approach of pion tracks to the primary vertex. The embedded tracks are compared to the ones in real data at $0.2 < p_T < 0.5$ GeV/c at midrapidity ($|y| < 0.1$) in Au+Au collisions at $\sqrt{s_{NN}} = 7.7$ GeV. Bottom: Comparison between the distributions of number of fit points for pions from embedding and from real data for $0.2 < p_T < 0.5$ GeV/c at midrapidity in Au+Au collisions at $\sqrt{s_{NN}} = 7.7$ GeV.

from z distributions can be found in Ref. [43].

The raw yields from the TOF are obtained using the variable mass-square (m^2), given by

$$m^2 = p^2 \left(\frac{T^2 c^2}{L^2} - 1 \right), \quad (2)$$

where, p , T , L , and c are the momentum, time-of-travel by the particle, path length, and speed of light, respectively. The m^2 distributions are obtained for rapidity $|y| < 0.1$ for all particles in different p_T ranges as shown by the black histograms in Fig. 5. Since the m^2 distributions are not exactly Gaussian, we use the predicted m^2 distributions to fit these distributions to extract the raw yields. The predicted m^2 distributions can be obtained

using

$$m_{\text{predicted}}^2 = p^2 \left(\frac{c^2 T_{\text{predicted}}^2}{L^2} - 1 \right). \quad (3)$$

Here $T_{\text{predicted}}$ is the predicted time-of-flight based on the random shift to the expected time-of-flight distributions for a given particle, i.e. $T_{\text{predicted}} = T_{\text{expected}} + t_{\text{random}}$, where t_{random} represents the random time shift based on the $\Delta T (= T_{\text{measured}} - T_{\text{expected}})$ distribution for a given particle. Here, T_{measured} represents the experimentally measured time-of-flight and T_{expected} is the expected time-of-flight for a given hadron obtained using its known mass in Eq. (2). The $m_{\text{predicted}}^2$ distributions are fitted to measured m^2 distributions, simultaneously for pions (dashed-red), kaons (dashed-green), and protons (dashed-blue) as shown in Fig. 5. Using χ^2 -minimization, the raw yield for a given hadron in a given p_T range is obtained.

III. CORRECTION FACTORS

A. TPC Tracking Efficiency and Acceptance

The principal correction to the raw spectra accounts for the detector acceptance and for the efficiency of reconstructing particle tracks. These effects are determined together by embedding Monte Carlo tracks simulated using the GEANT [46] model of the STAR detector into real events at the raw data level. One important requirement is to have a match in the distributions of reconstructed embedded tracks and real data tracks for quantities reflecting track quality and used for track selection. Figure 6 shows the comparisons of DCA and number of fit points (for embedded pions) distributions, respectively, in the low p_T range $0.2 < p_T < 0.5$ GeV/c. Similar agreement as in Fig. 6 is observed between embedded tracks and real data in other measured p_T ranges and beam energies for all the identified hadrons presented here. The ratio of the distribution of reconstructed and original Monte Carlo tracks as a function of p_T gives the efficiency \times acceptance correction factor for the rapidity interval studied. The typical efficiency \times acceptance factors for pions (left), kaons (middle) and protons (right) at midrapidity ($|y| < 0.1$) in 0–5% Au+Au collisions at $\sqrt{s_{NN}} = 7.7$ GeV are shown in Fig. 7. The raw yields are scaled by the inverse of the efficiency \times acceptance factors to obtain the corrected yields.

B. TOF Matching Efficiency

The TPC and the TOF are separate detectors. While the TPC identifies low- p_T (< 1 GeV/c) particles well, the TOF gives better particle identification than the TPC at higher momenta. However, not all TPC tracks give a hit in the TOF, so there is an extra correction called the

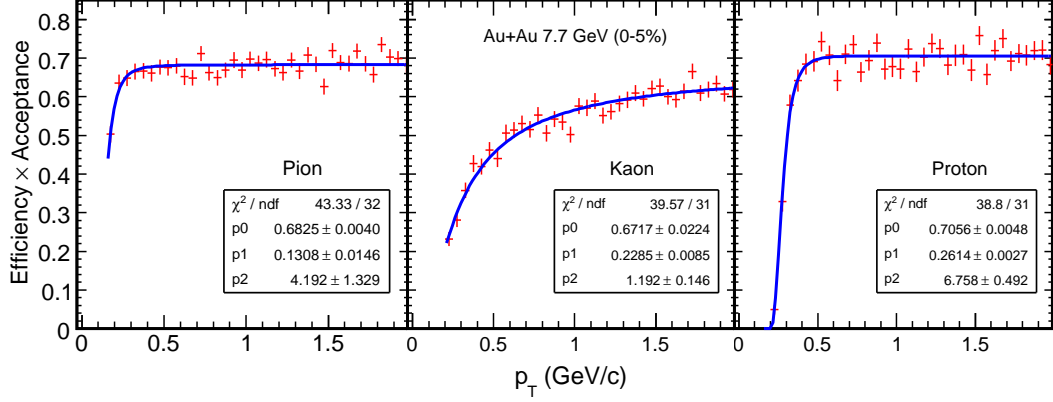


FIG. 7: Efficiency \times acceptance obtained from Monte Carlo embedding for reconstructed pions (left), kaons (middle) and protons (right) in the TPC as a function of p_T at midrapidity ($|y| < 0.1$) for 0-5% Au+Au collisions at $\sqrt{s_{NN}} = 7.7$ GeV. The curves represent the functional fit of the form $p_0 \exp[-(p_1/p_T)^{p_2}]$.

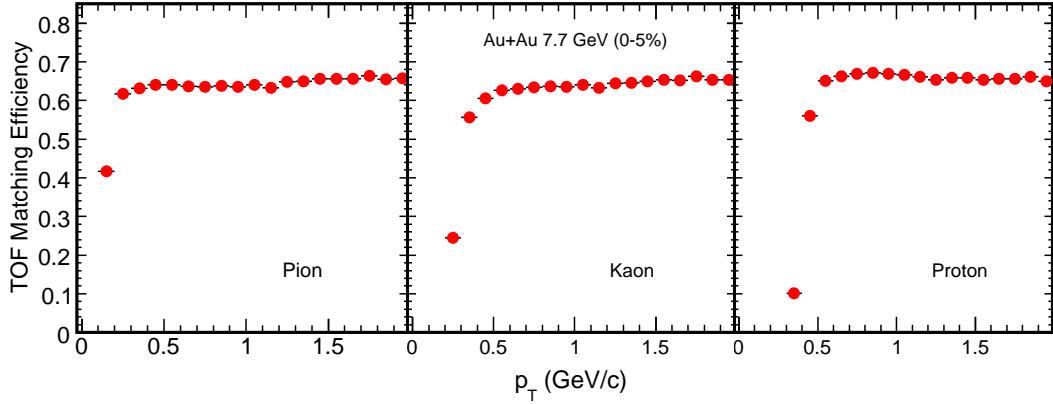


FIG. 8: TOF matching efficiency for pions (left), kaons (middle), and protons (right) as a function of p_T at midrapidity ($|y| < 0.1$) for 0-5% Au+Au collisions at $\sqrt{s_{NN}} = 7.7$ GeV.

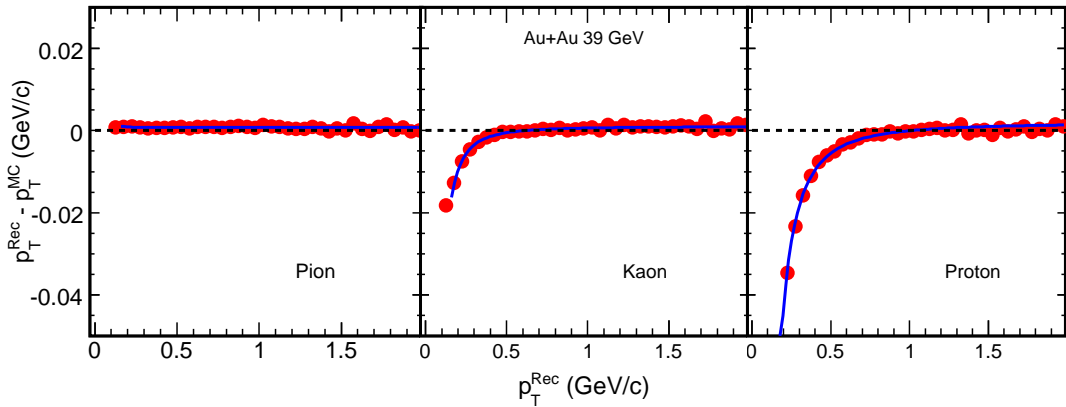


FIG. 9: The p_T difference between reconstructed and embedded tracks plotted as a function of the p_T of the reconstructed track for pions (left), kaons (middle), and protons (right) at midrapidity ($|y| < 0.1$) in Au+Au collisions at $\sqrt{s_{NN}} = 39$ GeV. This difference is due to particle energy loss in the detector material, which is already corrected in the tracking algorithm for pions, but only partially for kaons and protons.

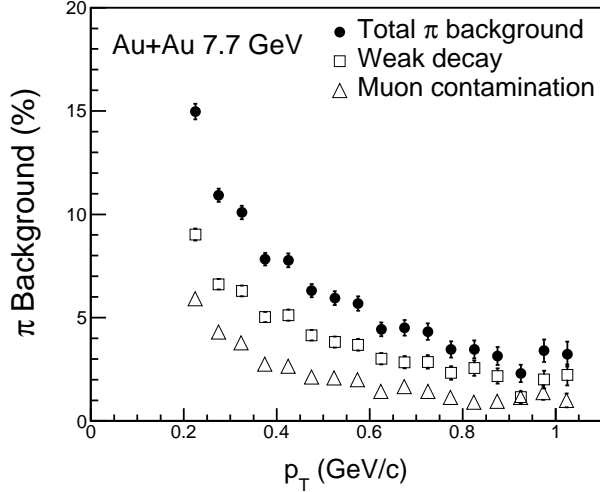


FIG. 10: Percentage of pion background contribution estimated from HIJING+GEANT simulation as a function of p_T at midrapidity ($|y| < 0.1$) in 0–5% Au+Au collisions at $\sqrt{s_{NN}} = 7.7$ GeV. The contributions from different sources are shown separately, as well as the total background.

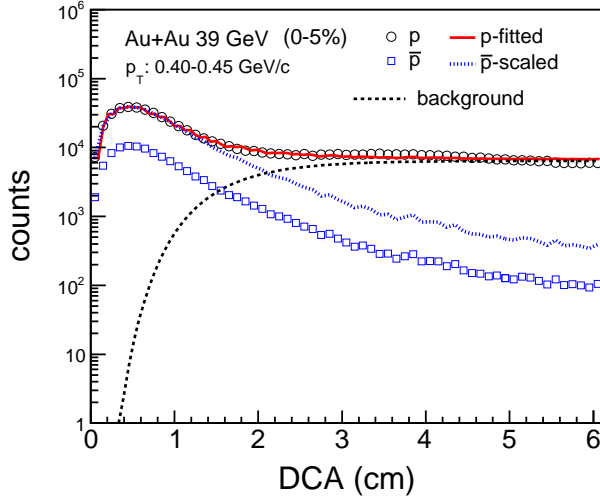


FIG. 11: The DCA distributions of protons and antiprotons for $0.40 < p_T < 0.45$ GeV/c at midrapidity ($|y| < 0.1$) in 0–5% Au+Au collisions at $\sqrt{s_{NN}} = 39$ GeV. The dashed curve is the fitted proton background; the dotted histogram is the \bar{p} distribution scaled by the p/\bar{p} ratio; and the solid histogram is the fit given by Eq. (6).

TOF matching efficiency correction needed for the spectra obtained using the TOF detector. This is done with a data driven technique. The TOF matching efficiency for a given particle species is defined as the ratio of the number of tracks detected in the TOF to the number of the total tracks in the TPC within the same acceptance. Figure 8 represents the typical TOF matching efficiencies

TABLE IV: Fit parameters for the energy loss of kaons and protons obtained using Eq. 4.

Values	Kaons	Protons
A_e	$9.7 \times 10^{-4} \pm 9.5 \times 10^{-5}$	0.0012 ± 0.0001
B_e	$-2.8 \times 10^{-6} \pm 8.3 \times 10^{-6}$	$-7.2 \times 10^{-6} \pm 2.3 \times 10^{-6}$
C_e	89.6 ± 70.2	98.4 ± 88.1
D_e	1.07 ± 0.04	1.13 ± 0.02
χ^2/NDF	43/36	43/34

for pions (left), kaons (middle), and protons (right) for 0–5% Au+Au collisions at $\sqrt{s_{NN}} = 7.7$ GeV. The raw yields obtained from the TOF are scaled by the inverse of the TOF matching efficiency to obtain the corrected yields.

C. Energy Loss Correction

Low momentum particles lose significant energy while traversing the detector material. The track reconstruction algorithm takes into account the Coulomb scattering and energy loss assuming the pion mass for each particle. Therefore, a correction for the energy loss by heavier particles is needed. This correction is obtained from embedding Monte Carlo simulations, in which the p_T difference between reconstructed and embedded tracks is plotted as a function of p_T of the reconstructed track.

Figure 9 shows the energy loss as a function of p_T for pions (left), kaons (middle), and protons (right). The blue curves represent the function fitted to the data points [43]

$$f(p_T) = A_e + B_e \left(1 + \frac{C_e}{p_T^2} \right)^{D_e}, \quad (4)$$

where A_e , B_e , C_e and D_e are the fit parameters. Table IV shows the values of these fit parameters obtained for kaons and protons. The energy loss for a given particle is independent of beam energy and collision centrality. For the results presented here, the track p_T is corrected for this energy loss effect.

D. Pion Background Subtraction

The charged pion spectra are corrected for feed-down contribution from weak decays, muon contamination, and background pions produced in the detector materials. These corrections are obtained from Monte Carlo simulations of HIJING events at $\sqrt{s_{NN}} = 7.7$ –39 GeV, with the STAR geometry for these data and a realistic description of the detector response implemented in GEANT. The simulated events are reconstructed in the same way as the real data. The weak-decay daughter pions are mainly from K_S^0 and Λ , and are identified by

the parent particle information accessible from the simulation. The muons from pion decays can be misidentified as primordial pions due to their similar masses. This contamination is obtained from Monte Carlo simulations by identifying the decay, which is accessible in the simulation. The weak-decay pion background and muon contamination obtained from the simulation are shown in Fig. 10, as a function of simulated pion p_T for 0–5% central Au+Au collisions at $\sqrt{s_{NN}} = 7.7$ GeV. The total pion background contribution from weak-decays decreases with increasing p_T . This contribution has been estimated for beam energies $\sqrt{s_{NN}} = 7.7$ –39 GeV. The background percentage for different energies and centralities is of similar order. The final pion spectra at different energies are corrected for this background effect.

E. Proton Background Subtraction

The STAR experiment has previously observed that proton yields have significant contamination from secondary protons, due to interactions of energetic particles produced in collisions with detector materials [43, 47]. As these secondary, so-called knock-out protons are produced away from the primary interaction point, they appear as a long tail in the DCA distribution of protons.

To estimate this proton background, a comparison between the shapes of DCA distributions of protons and anti-protons is done [43, 47]. Figure 11 shows the DCA distributions of protons and antiprotons for $0.40 < p_T < 0.45$ (GeV/ c) in 0–5% Au+Au collisions at $\sqrt{s_{NN}} = 39$ GeV. The protons and antiprotons are selected using a dE/dx cut of $|n_{\sigma_p}| < 2$, where $n_{\sigma_p} = z_p/\sigma_p$, σ_p being the relative dE/dx resolution of the TPC which is track length dependent. The long and flat DCA tail in the proton distribution comes mainly from knock-out background protons. Antiprotons do not have this background and hence no flat tail in their DCA distributions. To correct for the knock-out background protons, DCA dependence at $DCA < 3$ cm is needed for knock-out protons. It is obtained from MC simulation [43, 47] and is given by

$$N_p^{\text{bkgd}}(DCA) \propto [1 - \exp(-DCA/DCA_0)]^\alpha, \quad (5)$$

where DCA_0 and α are fit parameters. It is assumed that the shape of the background-subtracted proton DCA distribution is identical to that of the anti-proton. This distribution can be fit by

$$N_p(DCA) = N_{\bar{p}}(DCA)/r_{\bar{p}/p} + FN_p^{\text{bkgd}}(DCA) \quad (6)$$

Here, $r_{\bar{p}/p}$ and F are the fit parameters. We used this functional form to fit the proton DCA distributions for every p_T bin in each centrality at each energy to obtain the fraction of proton background.

The proton background fraction decreases with increasing p_T . The fraction of proton background increases from central to peripheral collisions. In Au+Au collisions at $\sqrt{s_{NN}} = 39$ GeV, the background fraction at

$p_T=0.40$ – 0.45 GeV/ c is about 15% for 0–5% centrality and 30% for 70–80%, while at the lowest energy ($\sqrt{s_{NN}} = 7.7$ GeV), it is 2% and 10% for 0–5% and 70–80% centralities, respectively. The reason for variation of proton background fraction with centrality may be that the ratio of proton multiplicity to total particle multiplicity shows centrality dependence. The proton background fraction as a function of p_T is subtracted from the proton raw yields for each centrality and collision energy studied.

It may be noted that the results presented here for BES energies correspond to inclusive protons and anti-protons similar to those at higher RHIC energies [43] as the feed-down correction has large uncertainty and is very model dependent. The analysis cut ($DCA < 3$ cm) used for the identified particle studies rejects only a negligible fraction of daughter protons from the hyperon decays [48, 49]. Therefore, the (anti-) protons yields presented here are truly inclusive.

IV. SYSTEMATIC UNCERTAINTIES

Systematic uncertainties on the spectra are estimated by varying cuts, and by assessing the purity of identified hadron samples from dE/dx measurements. Details of various sources of systematic uncertainties on the pion, kaon and proton/anti-proton yields in Au+Au collisions at $\sqrt{s_{NN}} = 7.7$ GeV are given below. The systematic uncertainties for other energies are estimated in a similar manner and are of a similar order.

The systematic uncertainties are estimated, by varying the V_z range (from $|V_z| < 50$ cm to $|V_z| < 30$ cm). The track cuts are also varied such as the DCA (from 3 cm to 2 cm), number of fit points (from 25 to 20), number of dE/dx points (from 15 to 10), PID cut i.e. $|n_\sigma|$, for the purity of a hadron used to obtain predicted m^2 distributions (from $|n_\sigma| < 2$ to $|n_\sigma| < 1$), and range of Gaussian fits to normalized dE/dx distributions. Combined systematic uncertainties due to all these analysis cut variations are of the order of 4%, 3%, and 6% for pions, kaons, and protons, respectively. The systematic uncertainty due to track reconstruction efficiency and acceptance estimates is of the order of 5% which is obtained by varying parameters in the MC simulation.

The p_T -integrated particle yield dN/dy and $\langle p_T \rangle$ are obtained from the p_T spectra using data in the measured p_T ranges and extrapolations assuming certain functional forms for the unmeasured p_T ranges [43]. The percentage contribution to the yields from extrapolation are about 20–30%. The extrapolation of yields to the unmeasured regions in p_T is an additional source of systematic error. This is estimated by comparing the extrapolations using different fit functions to the p_T spectra. For pions, the default function used to obtain dN/dy is the Bose-Einstein function and the systematic error is obtained by changing the functional form to the p_T -exponential function. For kaons, the m_T -exponential function is used for dN/dy and the Boltzmann function for the systematic er-

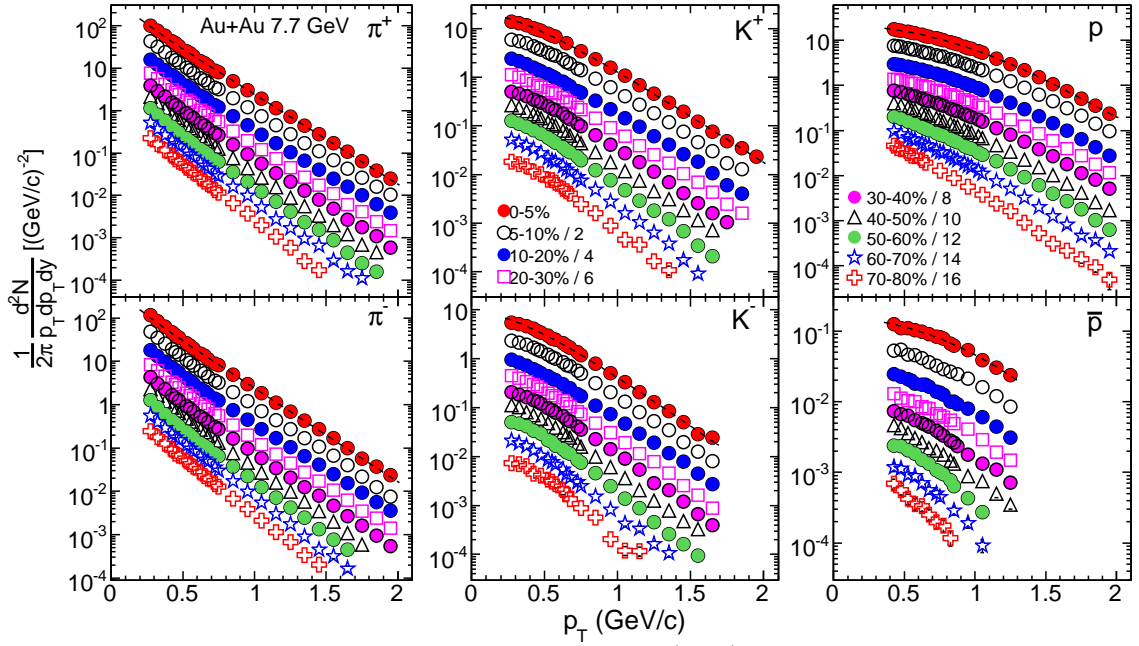


FIG. 12: Mid-rapidity ($|y| < 0.1$) transverse momentum spectra for π^\pm , K^\pm , p and \bar{p} in Au+Au collisions at $\sqrt{s_{NN}} = 7.7$ GeV for different centralities. The spectra for centralities other than 0–5% are scaled for clarity as shown in figure. The curves represent the Bose-Einstein, m_T -exponential, and double-exponential function fits to 0–5% central data for pions, kaons, and protons-antiprotons, respectively. The uncertainties are statistical and systematic added in quadrature.

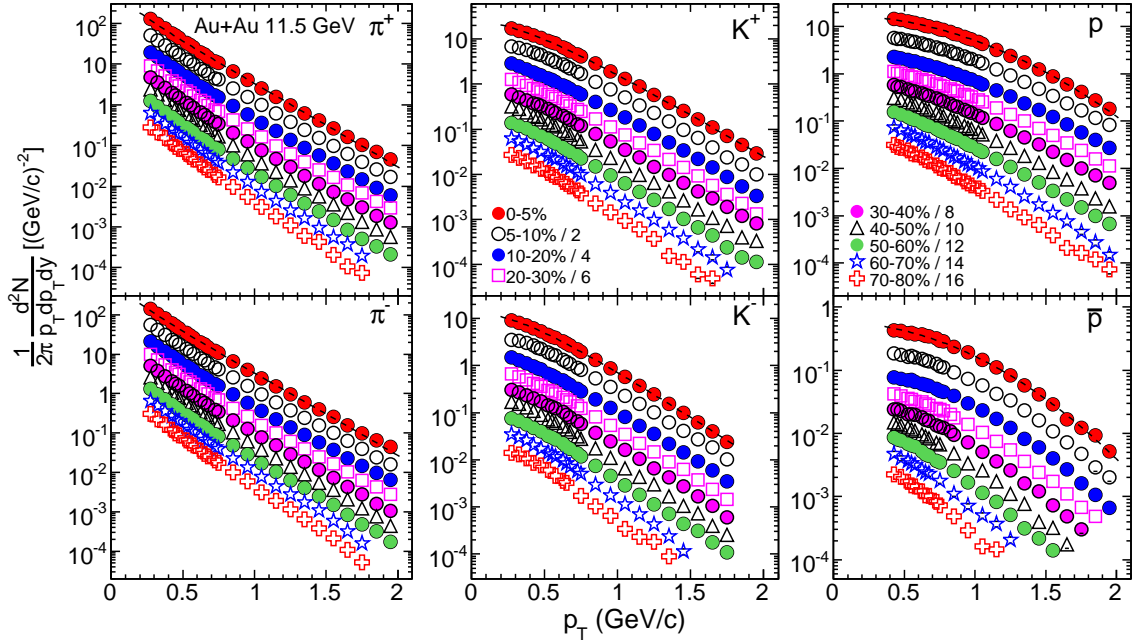


FIG. 13: Same as Fig. 12 but for Au+Au collisions at $\sqrt{s_{NN}} = 11.5$ GeV.

ror. Here $m_T = \sqrt{m^2 + p_T^2}$ represents the particle transverse mass. For protons, the double-exponential function is used for dN/dy and the m_T -exponential function is used to obtain the systematic error. The functional form of these functions are

- Bose-Einstein: $\propto 1/(e^{m_T/T} - 1)$,

- p_T -exponential: $\propto e^{-p_T/T}$,

- m_T -exponential: $\propto e^{-(m_T - m)/T}$,

- Boltzmann: $\propto m_T e^{-m_T/T}$,

- Double-exponential: $A_1 e^{-p_T^2/T_1^2} + A_2 e^{-p_T^2/T_2^2}$.

Systematic uncertainties due to extrapolation to unmeasured p_T region is estimated to be of the order of 6-9% for pions, 4-8% for kaons, and 10-12% for protons and anti-protons.

The systematic uncertainties arising due to the pion and proton background are also studied. The systematic uncertainty due to pion background is found to be negligible. However, the uncertainty due to the proton background is about 6-7% (39–19.6 GeV) and 2-4% (7.7–11.5 GeV). In addition, the systematic uncertainties due to energy loss estimation (discussed previously) for kaons and protons are found to be of the order of 3% and 2%, respectively.

The total systematic uncertainties are obtained by adding the contribution from different sources in quadrature and are found to be of the order of 9-11% for pions, 8-10% for kaons, 11-13% for protons and 12-13% for anti-protons for all energies. The results presented here are quadrature sums of these systematic uncertainties and statistical uncertainties, the latter being negligible. Table V gives a summary of various sources of systematic uncertainties for all energies.

The systematic uncertainties on particle ratios are obtained using the uncertainties on particle yields, but excluding correlated uncertainties i.e. from efficiency. In addition, the extrapolation and energy loss uncertainties are canceled to a large extent in the antiparticle to particle ratios.

The systematic uncertainties for $\langle p_T \rangle$ come mainly from the extrapolations as discussed above. The $\langle p_T \rangle$ also depends on the range used for fitting to the p_T spectra. The variations in the $\langle p_T \rangle$ values due to different fitting ranges are included in the systematic uncertainties. The total systematic uncertainties on $\langle p_T \rangle$ for pions, kaons, and protons-antiprotons are 5-6%, 4-6%, and 6-11%, respectively, across all beam energies.

Chemical freeze-out parameters (chemical freeze-out temperature T_{ch} , μ_B , μ_S , γ_S , and radius R) are extracted from the measured particle yields or ratios fitted in the THERMUS model [50]. The systematic uncertainties on the yields are treated as independent, and are propagated to the systematic uncertainties on chemical freeze-out parameters. We have also estimated the effect of correlated uncertainties in particle ratios used to extract the chemical freeze-out parameters. The effect arises because the pion yield is used for constructing many particle ratios. The effect of this on freeze-out parameters is estimated by varying the uncertainties on pion yields and extracting the freeze-out parameters for a large sample of pion yields. We have found that the effect is within 3% for the extracted freeze-out parameters.

The kinetic freeze-out parameters are extracted from the simultaneous fitting of π^\pm , K^\pm , and protons and anti-protons spectra with the blast-wave model [51]. The extracted fit parameters are kinetic freeze-out temperature T_{kin} , average radial flow velocity $\langle \beta \rangle$, and the flow velocity profile exponent n . The point-to-point systematic uncertainties on the spectra are included in the blast-

TABLE V: Sources of percentage systematic uncertainties for pions, kaons, and (anti-) protons yields at all energies.

Sources	π	K	p (\bar{p})
Cuts	4%	3%	6%
Tracking eff.	5%	5%	5%
Energy Loss	–	3%	2%
Extrapolation	6–9%	4–8%	10–12%
Total	9–11%	8–10%	11–13%

wave fits. The measured pions contain large contributions from resonance decays which vary as a function of p_T . Since the default blast-wave model does not include resonance decays, in order to reduce the systematic error due to resonance decays, the low p_T part (< 0.5 GeV/ c) of the pion spectra are excluded from the blast-wave fit. The results from the blast-wave fits are sensitive to the range of p_T used for fitting the spectra. The effect on the extracted kinetic freeze-out parameters due to different p_T ranges used for fitting is estimated. These variations are included in the systematic uncertainties for kinetic freeze-out parameters.

V. RESULTS AND DISCUSSIONS

A. Transverse Momentum Spectra

Figure 12 shows the transverse momentum spectra for π^\pm , K^\pm , and p (\bar{p}), in Au+Au collisions at $\sqrt{s_{NN}} = 7.7$ GeV. The results are shown for the collision centrality classes of 0–5%, 5–10%, 10–20%, 20–30%, 30–40%, 40–50%, 50–60%, 60–70%, and 70–80%. The p_T spectra for 11.5, 19.6, 27, and 39 GeV are shown in Figs. 13, 14, 15, and 16, respectively. The inverse slopes of the identified hadron spectra follow the order $\pi < K < p$. The spectra can be further characterized by the dN/dy and $\langle p_T \rangle$ or $\langle m_T \rangle - m$ for the produced hadrons, where m is the mass of the hadron and m_T is its transverse mass.

B. Centrality Dependence of Particle Production

1. Particle yields (dN/dy)

Figure 17 shows the comparison of collision centrality dependence of dN/dy of π^\pm , K^\pm , p and \bar{p} , normalized by $\langle N_{\text{part}} \rangle / 2$, among the results at $\sqrt{s_{NN}} = 7.7, 11.5, 19.6, 27$, and 39 GeV, and previously published results at $\sqrt{s_{NN}} = 62.4$ and 200 GeV from the STAR experiment [11–14, 43, 48]. The yields of charged pions, kaons, and anti-protons decrease with decreasing collision energy. However, the yield of protons is the highest for the lowest energy of 7.7 GeV, which indicates the highest baryon density at mid-rapidity at this energy. Proton yield decreases from 7.7 GeV through 11.5, 19.5, 27,

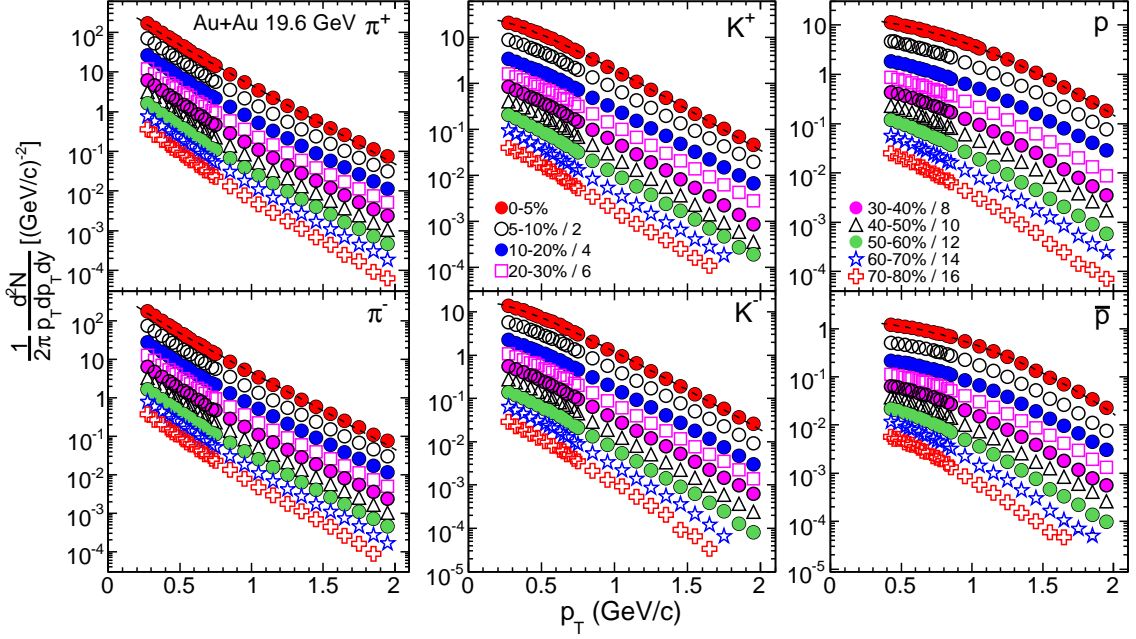


FIG. 14: Same as Fig. 12 but for Au+Au collisions at $\sqrt{s_{NN}} = 19.6$ GeV.

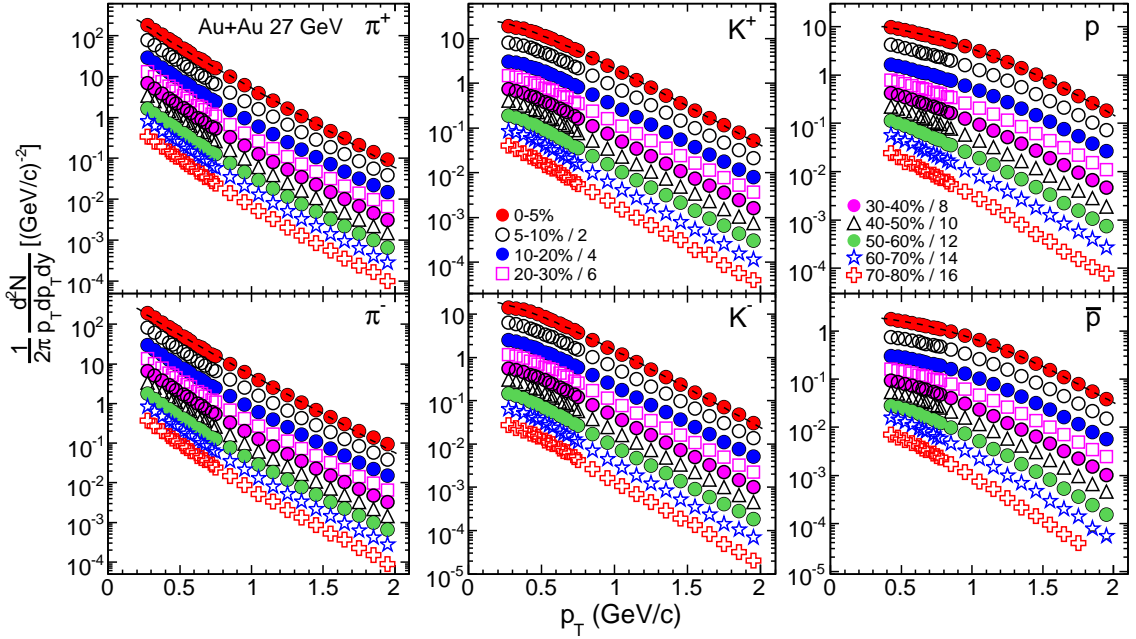


FIG. 15: Same as Fig. 12 but for Au+Au collisions at $\sqrt{s_{NN}} = 27$ GeV.

and 39 GeV, lowest being at 39 GeV. Then it again increases at 62.4 GeV up to 200 GeV. The proton yields come from two mechanisms: pair production and baryon transport [52]. The energy dependence trend observed here for the proton yield is due to interplay of these two mechanisms. The collision centrality dependence for the BES results is similar to that at higher beam energies. The normalized yields decrease from central to peripheral collisions for π^\pm , K^\pm , and p . However, the central-

ity dependence of normalized yields for \bar{p} is weak. The dN/dy values for π^\pm , K^\pm , p and \bar{p} in different centralities at various BES energies are listed in Table VI.

2. Average Transverse Momentum p_T ($\langle p_T \rangle$)

Figure 18 shows the comparison of $\langle p_T \rangle$ as a function of $\langle N_{part} \rangle$ for π^\pm , K^\pm , p and \bar{p} , in Au+Au collisions

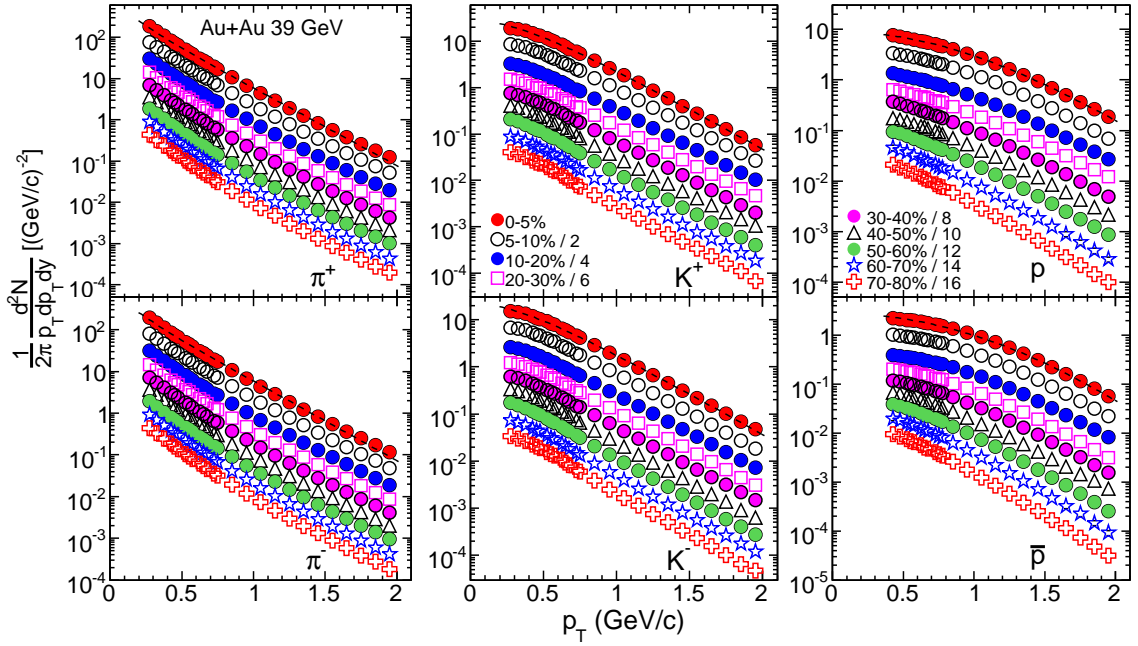


FIG. 16: Same as Fig. 12 but for Au+Au collisions at $\sqrt{s_{NN}} = 39$ GeV.

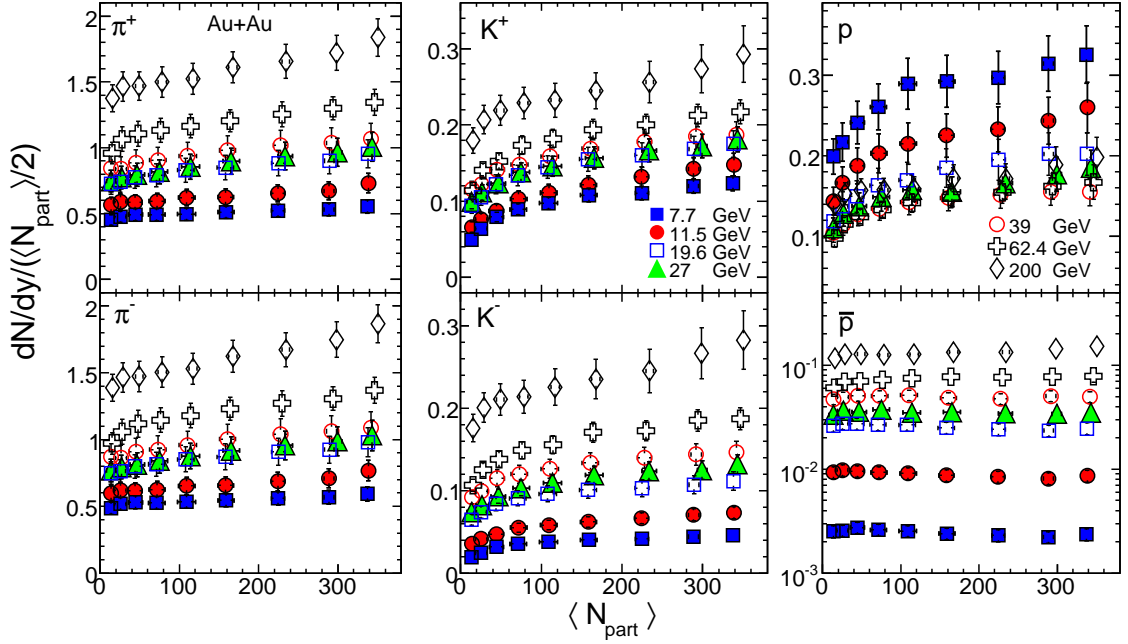


FIG. 17: Centrality dependence of dN/dy normalized by $\langle N_{\text{part}} \rangle / 2$ for π^\pm (left panels), K^\pm (middle panels), p and \bar{p} (right panels) at midrapidity ($|y| < 0.1$) in Au+Au collisions at $\sqrt{s_{NN}} = 7.7, 11.5, 19.6, 27$, and 39 GeV. Results are compared with published results in Au+Au collisions at $\sqrt{s_{NN}} = 62.4$ and 200 GeV [43, 48]. Errors shown are the quadrature sum of statistical and systematic uncertainties. For clarity, $\langle N_{\text{part}} \rangle$ uncertainties are not added in quadrature.

at $\sqrt{s_{NN}} = 7.7, 11.5, 19.6, 27$, and 39 GeV. Results are compared with the published results in Au+Au collisions at $\sqrt{s_{NN}} = 62.4$ and 200 GeV [11–14, 43, 48]. The dependences of $\langle p_T \rangle$ on $\langle N_{\text{part}} \rangle$ at BES energies are similar to those at $\sqrt{s_{NN}} = 62.4$ and 200 GeV. An increase in $\langle p_T \rangle$ with increasing hadron mass is observed at

all BES energies. A similar dependence is also observed for $\sqrt{s_{NN}} = 62.4$ and 200 GeV. The mass dependence of $\langle p_T \rangle$ reflects collective expansion in the radial direction, although it also includes the temperature component. The differences in central values of $\langle p_T \rangle$ between protons and pions/kaons are smaller at lower energies

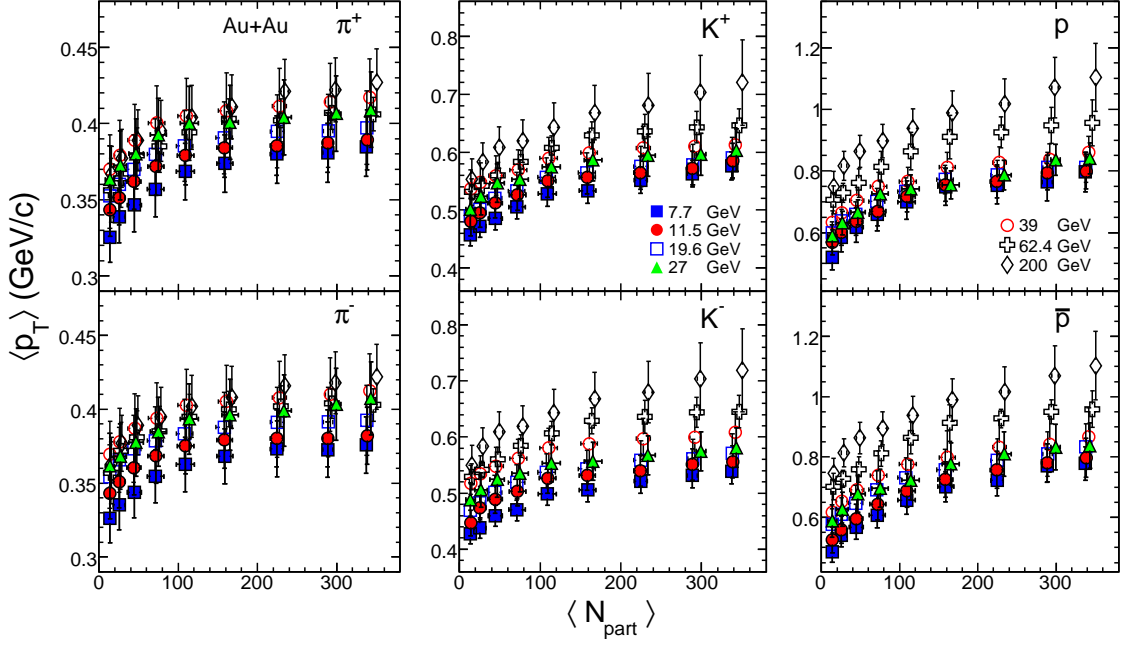


FIG. 18: Centrality dependences of $\langle p_T \rangle$ for π^\pm (left panels), K^\pm (middle panels), p and \bar{p} (right panels) at midrapidity ($|y| < 0.1$) in Au+Au collisions at $\sqrt{s_{NN}} = 7.7, 11.5, 19.6, 27$, and 39 GeV. Results are compared with published results in Au+Au collisions at $\sqrt{s_{NN}} = 62.4$ and 200 GeV [43, 48]. Errors shown are quadrature sum of statistical and systematic uncertainties where the latter dominates.

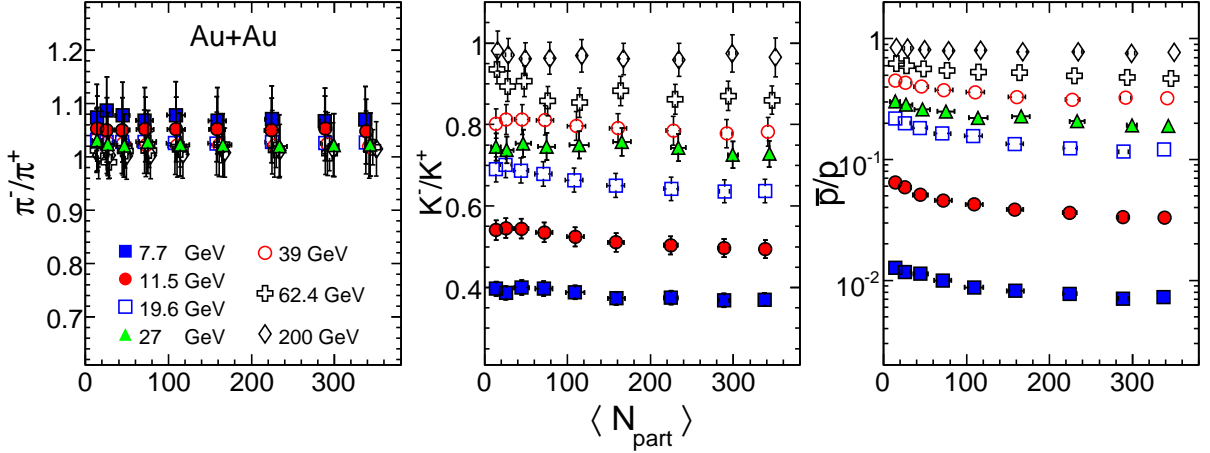


FIG. 19: Variation of π^-/π^+ (left), K^-/K^+ (middle), and \bar{p}/p (right) ratios as a function of $\langle N_{part} \rangle$ at midrapidity ($|y| < 0.1$) in Au+Au collisions at all BES energies. Also shown for comparison are the corresponding results in Au+Au collisions at $\sqrt{s_{NN}} = 62.4$ and 200 GeV [11–14, 43]. Errors shown are the quadrature sum of statistical and systematic uncertainties where the latter dominates.

compared to those at higher beam energies. This suggests that the average collective velocity in the radial direction is smaller at lower energies. The $\langle p_T \rangle$ values for π^\pm , K^\pm , p and \bar{p} in different centralities at various BES energies are listed in Table VII.

3. Particle Ratios

Figure 19 shows the various anti-particle to particle ratios (π^-/π^+ , K^-/K^+ , \bar{p}/p) as a function of collision centrality expressed as $\langle N_{part} \rangle$ in Au+Au collisions at all BES energies. Corresponding results from Au+Au collisions at $\sqrt{s_{NN}} = 62.4$ and 200 GeV [11–14, 43, 48] are

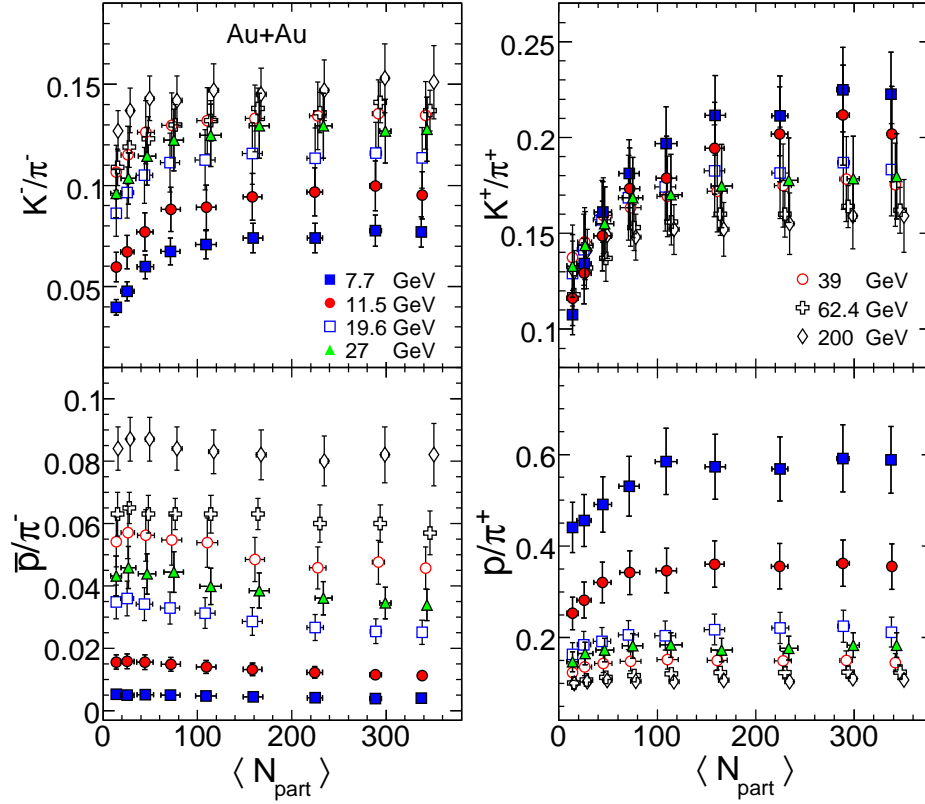


FIG. 20: Variation of K^-/π^- , K^+/π^+ , \bar{p}/π^- , and p/π^+ ratios as a function of $\langle N_{\text{part}} \rangle$ at midrapidity ($|y| < 0.1$) in Au+Au collisions at all BES energies. Also shown for comparison are the corresponding results in Au+Au collisions at $\sqrt{s_{NN}} = 62.4$ and 200 GeV [11–14, 43]. Errors shown are the quadrature sum of statistical and systematic uncertainties where the latter dominates.

also shown. The π^-/π^+ ratio is close to unity for most of the energies. However, a slight energy dependence is observed for lower energies. The lowest energy of 7.7 GeV has a larger π^-/π^+ ratio than those at the other energies due to isospin and significant contributions from resonance decays (such as Δ baryons). The K^-/K^+ ratio increases with increasing energy, and shows very little centrality dependence. The increase in K^-/K^+ ratio with energy shows the increasing contribution to kaon production due to pair production. However, at lower energies, associated production dominates. Associated production refers to reactions such as $NN \rightarrow KYN$ and $\pi N \rightarrow KY$, where N is a nucleon and Y a hyperon. The \bar{p}/p ratio increases with increasing energy. The ratio increases from central to peripheral collisions. This increase in \bar{p}/p ratio from central to peripheral collisions reflects a higher baryon density (baryon stopping) at mid-rapidity in central collisions compared to peripheral collisions.

Figure 20 shows the centrality dependence of mixed ratios (K^-/π^- , K^+/π^+ , \bar{p}/π^- , and p/π^+). These results are also compared with corresponding results at $\sqrt{s_{NN}} = 62.4$ and 200 GeV. The K^-/π^- ratio increases with increasing energy, and also increases from peripheral to central collisions. However, the K^+/π^+ ratio is maximal at 7.7 GeV and then decreases with increasing energy.

This is due to the associated production dominance at lower energies as the baryon stopping is large. The centrality dependence of K^+/π^+ is observed at all energies, i.e., the ratio increases from peripheral to central collisions. This increase from peripheral to central collisions is much greater at 7.7 GeV than at the higher BES energies. This may be due to large baryon stopping at midrapidity at the lower energy of 7.7 GeV. This baryon stopping is centrality dependent, i.e. higher in more central collisions as also reflected by the \bar{p}/p ratio. The \bar{p}/π^- ratio increases with increasing beam energy and shows little centrality dependence. The p/π^+ ratio decreases with increasing energy. As discussed above, this is a consequence of the higher baryon stopping at lower energies. The ratio increases from peripheral to central collisions and becomes almost constant after $\langle N_{\text{part}} \rangle > 100$.

C. Energy Dependence of Particle Production

1. Particle yields (dN/dy)

Figure 21 shows the dN/dy of π^\pm , K^\pm , and p/\bar{p} , at midrapidity normalized by $\langle N_{\text{part}} \rangle / 2$ as a function of

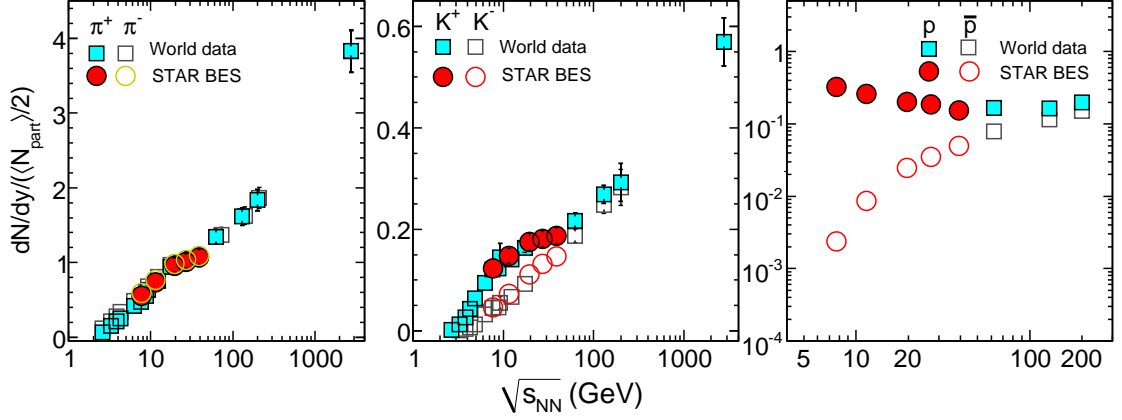


FIG. 21: The midrapidity ($|y| < 0.1$) dN/dy normalized by $\langle N_{\text{part}} \rangle / 2$ as a function of $\sqrt{s_{NN}}$ for π^\pm (left), K^\pm (middle), and p and \bar{p} (right). Results in 0–5% Au+Au collisions at BES energies are compared to previous results from AGS [53–60], SPS [61–64], RHIC [27, 43, 65], and LHC [66]. AGS results correspond to 0–5%, SPS to 0–7%, top RHIC to 0–5% (62.4 and 200 GeV) and 0–6% (130 GeV), and LHC to 0–5% central collisions. Errors shown are the quadrature sum of statistical and systematic uncertainties where the latter dominates.

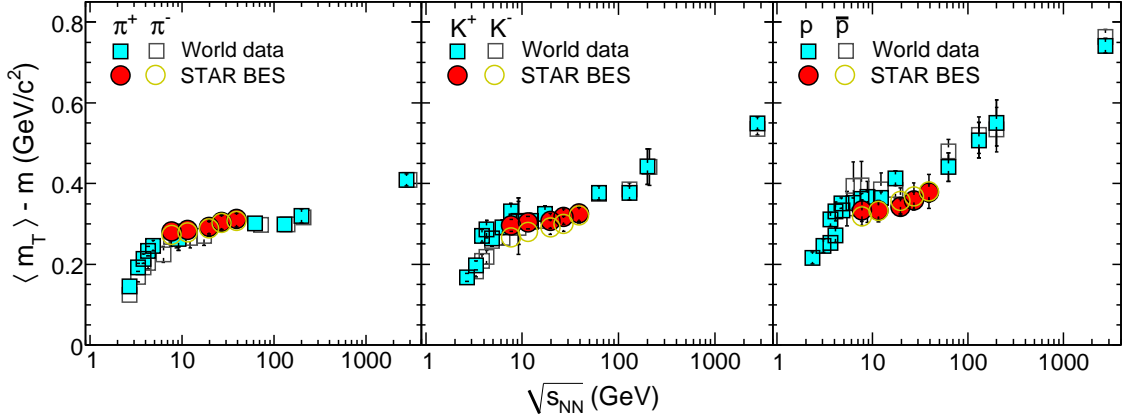


FIG. 22: $\langle m_T \rangle - m$ of π^\pm (left), K^\pm (middle), and p and \bar{p} (right) as a function of $\sqrt{s_{NN}}$. Midrapidity ($|y| < 0.1$) results are shown for 0–5% central Au+Au collisions at BES energies, and are compared to previous results from AGS [53–60], SPS [61–64], RHIC [43], and LHC [66]. AGS results correspond to 0–5%, SPS to 0–7%, top RHIC to 0–5% (62.4 and 200 GeV) and 0–6% (130 GeV), and LHC to 0–5% central collisions. The errors shown are the quadrature sum of statistical and systematic uncertainties where the latter dominates.

$\sqrt{s_{NN}}$. The results from 0–5% central Au+Au collisions at the BES are in agreement with the general energy dependence trend observed at the AGS [53–60], SPS [61–64], RHIC [27, 43, 65], and LHC [66]. It may be noted that the energy dependence of pion yields show a linear increase as a function of collision energy, but exhibit a kink structure around 19.6 GeV. This may suggest a change in the particle production mechanism around $\sqrt{s_{NN}} = 19.6$ GeV.

The energy dependence of kaon yields shows an interesting trend. There is a significant difference between K^+ and K^- production at beam energies from AGS to BES. At these energies, K^+ production is a result of an interplay between associated production and pair production, while K^- production is dominated by pair production.

The associated production dominates at the low end of this range, while pair production becomes more important at the upper end.

The energy dependence of proton yields reflects the increase in baryon density due to baryon stopping at lower energies. At top RHIC energies, the proton and anti-proton yields are of similar order, which is expected from pair production mechanism. At lower energies, protons have a contribution due to baryon stopping also, leading to higher yields at 7.7 GeV compared to 200 GeV. The anti-proton yields show an increase with increasing energy.

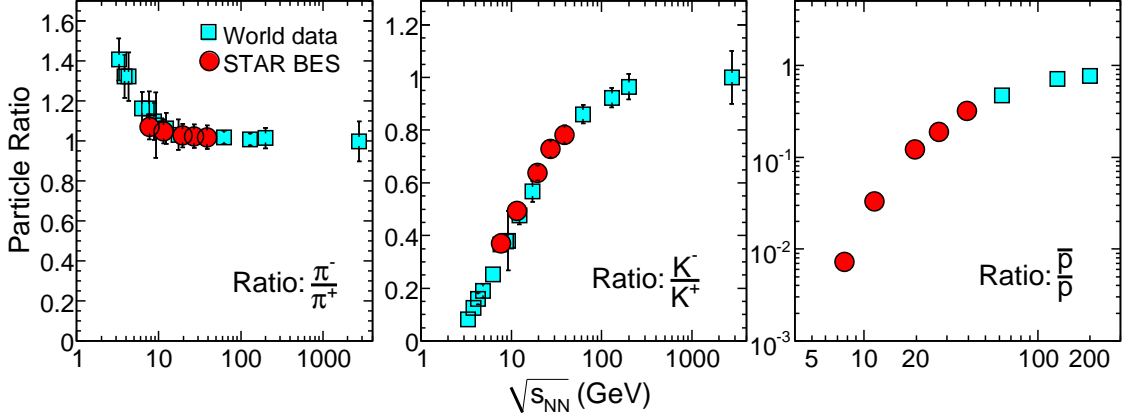


FIG. 23: π^-/π^+ (left), K^-/K^+ (middle), and \bar{p}/p (right) ratios at midrapidity ($|y| < 0.1$) in central 0–5% Au+Au collisions at $\sqrt{s_{NN}} = 7.7, 11.5, 19.6, 27$, and 39 GeV, compared to previous results from AGS [53–60], SPS [61–64], RHIC [27, 43], and LHC [66]. AGS results correspond to 0–5%, SPS to 0–7%, top RHIC to 0–5% (62.4 and 200 GeV) and 0–6% (130 GeV), and LHC to 0–5% central collisions. Errors shown are the quadrature sum of statistical and systematic uncertainties where the latter dominates.

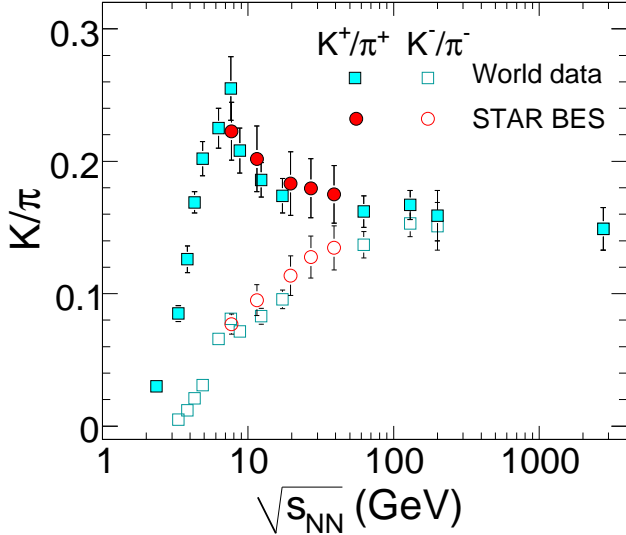


FIG. 24: K/π ratio at midrapidity ($|y| < 0.1$) for central 0–5% Au+Au collisions at $\sqrt{s_{NN}} = 7.7, 11.5, 19.6, 27$, and 39 GeV, compared to previous results from AGS [53–60], SPS [61–64], RHIC [27, 43], and LHC [66]. AGS results correspond to 0–5%, SPS to 0–7%, top RHIC to 0–5% (62.4 and 200 GeV) and 0–6% (130 GeV), and LHC to 0–5% central collisions. Errors shown are the quadrature sum of statistical and systematic uncertainties where the latter dominates.

2. Mean Transverse Mass ($\langle m_T \rangle$)

Figure 22 shows the energy dependence of $\langle m_T \rangle - m$ for π^\pm , K^\pm , p , and \bar{p} . Results are shown for 0–5% central Au+Au collisions at BES energies, and are compared to previous results from AGS [53–60], SPS [61–64], RHIC [43], and LHC [66]. The $\langle m_T \rangle - m$ values increase

with $\sqrt{s_{NN}}$ at lower AGS energies, stay independent of $\sqrt{s_{NN}}$ at the higher SPS and BES energies, then tend to rise further with increasing $\sqrt{s_{NN}}$ at the higher beam energies at RHIC and LHC. For a thermodynamic system, $\langle m_T \rangle - m$ can be an approximate representation of the temperature of the system, and $dN/dy \propto \ln(\sqrt{s_{NN}})$ may represent its entropy [67–69]. In such a scenario, the energy dependence of $\langle m_T \rangle - m$ could reflect the characteristic signature of a first order phase transition, as proposed by Van Hove [69]. Then the constant value of $\langle m_T \rangle - m$ vs. $\sqrt{s_{NN}}$ around BES energies could be interpreted as reflecting the formation of a mixed phase of a QGP and hadrons during the evolution of the heavy-ion system. However, there could be several other effects to which $\langle m_T \rangle - m$ is sensitive, which also need to be understood for proper interpretation of the data [70].

3. Particle Ratios

Figure 23 shows the collision energy dependence of the particle ratios π^-/π^+ , K^-/K^+ , and \bar{p}/p , in central heavy-ion collisions. The new results from Au+Au collisions at BES energies follow the $\sqrt{s_{NN}}$ trend established by previous measurements from AGS [53–60], SPS [61–64], RHIC [43], and LHC [66]. The p_T -integrated π^-/π^+ ratios at very low beam energies have values larger than unity, which is likely due to significant contributions from resonance decays (such as from Δ baryons). The K^-/K^+ ratios at BES energies are much less than unity, indicating a significant contribution to K^+ production from associated production at lower collision energies. With increasing $\sqrt{s_{NN}}$, the K^-/K^+ ratio approaches unity, indicating dominance of kaon pair production. The lower values of the \bar{p}/p ratios at BES energies indicates large values of net-protons ($p - \bar{p}$) and large baryon stopping

in these collisions. The \bar{p}/p ratio increases with increasing collision energy and approaches unity for top RHIC energies. This indicates that at higher beam energies the collisions have a larger degree of transparency, and the p (\bar{p}) production at midrapidity is dominated by pair production.

Figure 24 shows the energy dependence of K/π particle ratio. BES results are compared with those from AGS [53–60], SPS [61–64], RHIC [43], and LHC [66]. The K/π ratio is of interest, as it reflects the strangeness content relative to entropy in heavy-ion collisions. An enhancement in K/π ratio in heavy-ion collisions compared to $p+p$ collisions has been taken previously as an indication of QGP formation [64]. The increase in K^+/π^+ ratio with beam energies up to $\sqrt{s_{NN}} = 7.7$ GeV at SPS and the subsequent decrease and possible saturation with increasing beam energies has been a subject of intense theoretical debate [52, 61–64, 71–75]. The discussions mainly focus on the question of the relevant degrees of freedom that are necessary to explain the energy dependence of the K/π ratio. Our new results from BES Au+Au collisions are found to be consistent with the previously observed energy dependence. The peak position (usually called the “horn”) in energy dependence of K^+/π^+ has been suggested as the signature of a phase transition from hadron gas to a QGP while going from lower to higher energies. However, various models that do not include such a phase transition could also explain this type of energy dependence of the K^+/π^+ ratio. It may be noted that the peak position around 7.7 GeV corresponds to an energy where the maximum baryon density is predicted to be achieved in heavy-ion collisions [52, 76].

VI. FREEZE-OUT PARAMETERS

The integrated invariant yields and p_T spectra of hadrons provide information about the system at freeze-out. Two types of freeze-out are commonly discussed in heavy-ion collisions — chemical freeze-out and kinetic freeze-out. The state when the inelastic interactions among the particles stop is referred to as chemical freeze-out. The yields of the produced particles become fixed at chemical freeze-out. Statistical thermal models have successfully described the chemical freeze-out stage with system parameters such as chemical freeze-out temperature, T_{ch} , and baryon chemical potential, μ_B [4, 50, 77].

After chemical freeze-out, elastic interactions among the particles are still ongoing which lead to changes in the momenta of the particles. When the average inter-particle distance becomes so large that elastic interactions stop, the system is said to have undergone kinetic freeze-out. At this stage, the transverse momentum spectra of the produced particles become fixed. Hydrodynamics inspired models such as the Blast Wave Model [4, 43, 51] have described the kinetic freeze-out scenario with a common temperature T_{kin} and average transverse radial flow velocity $\langle\beta\rangle$ which reflects the ex-

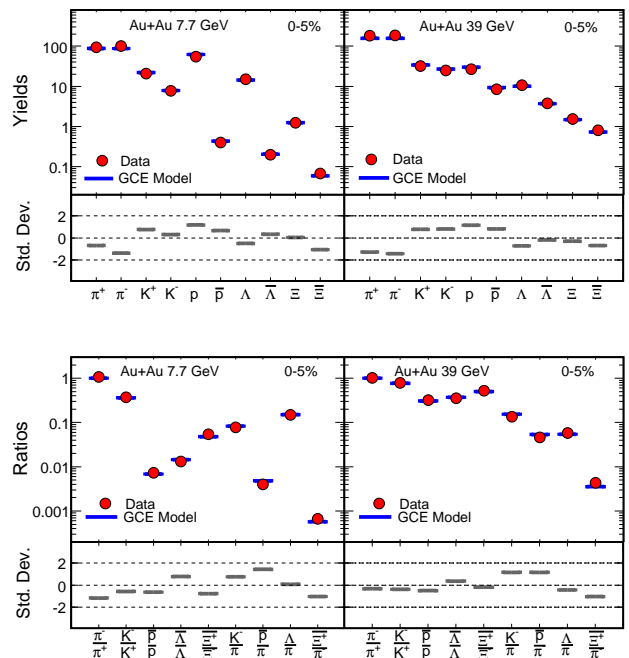


FIG. 25: The GCE model fits shown along with standard deviations for Au+Au 7.7 and 39 GeV in 0–5% central collisions. Top panel is for the particle yields fit and lower panel is for the particle ratios fit. Uncertainties on experimental data represent statistical and systematic uncertainties added in quadrature. Here, the uncertainties are smaller than the symbol size.

pansion in the transverse direction. In the following subsections, we discuss these freeze-out parameters in detail.

A. Chemical Freeze-out

The chemical freeze-out parameters are obtained from statistical thermal model analyses of the produced particles using the THERMUS package [50]. Two approaches are used to obtain the chemical freeze-out parameters: Grand-Canonical Ensemble (GCE) and Strangeness Canonical Ensemble (SCE). In the GCE, the energy and quantum numbers, or particle numbers, are conserved on average through the temperature and chemical potentials. This is reasonable if the number of particles carrying the quantum number is large. GCE is widely used in high-energy heavy-ion collisions. For the SCE, the strangeness (S) in the system is fixed exactly by its initial value of S , while the baryon and charge contents are treated grand-canonically. At lower energies, low production of strange particles requires a canonical treatment of strangeness [78]. Since the BES data cover a wide range of energies from low to high, both GCE and SCE approaches are studied here.

In addition, different approaches have been proposed to fit the data, i.e. whether particle yields or the particle ratios should be used in the fit. The fitting of particle

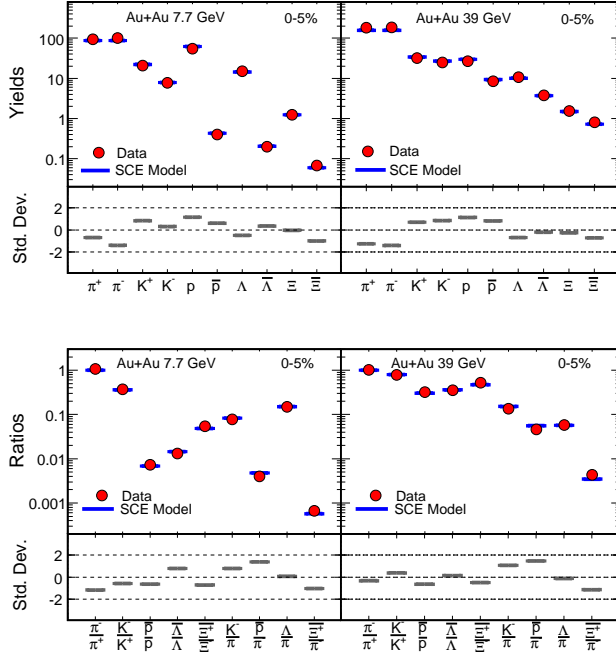


FIG. 26: The SCE model fits shown along with standard deviations for Au+Au 7.7 and 39 GeV in 0–5% central collisions. Top panel is for the particle yields fit and lower panel is for particle ratios fit. Uncertainties on experimental data represent statistical and systematic uncertainties added in quadrature. Here, the uncertainties are smaller than the symbol size.

ratios leads to the cancellation of a volume factor, thus getting rid of an extra parameter. However, a possible disadvantage is the use of a common particle to construct different ratios, leading to correlated uncertainties. We investigate the difference between these two approaches by fitting both the particle ratios and particle yields in THERMUS.

Since the freeze-out parameters represent collision system properties, it is better to also include the other strange particles in the THERMUS fitting. The results presented here for particle yields are obtained using yields of π^\pm , K^\pm , p , \bar{p} , Λ , $\bar{\Lambda}$, Ξ , and $\bar{\Xi}$. The corresponding results for particle ratios are obtained by using the ratios π^-/π^+ , K^-/K^+ , \bar{p}/p , $\bar{\Lambda}/\Lambda$, $\bar{\Xi}/\Xi$, K^-/π^- , \bar{p}/π^- , Λ/π^- , and $\bar{\Xi}/\pi^-$. The dN/dy of Λ , $\bar{\Lambda}$, Ξ and $\bar{\Xi}$ are obtained from the measured p_T spectra within $|y| < 0.5$, and a follow-up paper on the p_T spectra of these particles is in preparation (the technical details are currently available in Ref. [81]). As mentioned earlier, the (anti-) proton yields reported here by STAR are inclusive. The corresponding yields in the THERMUS model are treated in the same manner as in data i.e. all inclusive. The fraction of weak-decay feed-down contribution (from Λ , Σ , and Ξ) to proton yield from THERMUS is found to be 18% at 7.7 GeV and up to 29% at 39 GeV. The weak-decay feed-down contribution to anti-proton yield is found to be up to 50% at 7.7 GeV and 37% at 39 GeV. It may be noted

that the strange particle yields (Λ , $\bar{\Lambda}$, Ξ , and $\bar{\Xi}$) used here are measured for $|y| < 0.5$ while the light hadron yields (π^\pm , K^\pm , p , and \bar{p}) are measured for $|y| < 0.1$. The uncertainty due to this difference is not considered in the extraction of chemical freeze-out parameters.

Considering the grand canonical case, for a hadron gas of volume V and temperature T , the logarithm of the total partition function is given by [50],

$$\ln Z^{GC}(T, V, \{\mu_i\}) = \sum_{\text{species } i} \frac{g_i V}{(2\pi)^3} \int d^3p \ln(1 \pm e^{-\beta(E_i - \mu_i)})^{\pm 1} \quad (7)$$

where, g_i and μ_i are degeneracy and chemical potential of hadron species i respectively, $\beta = 1/T$, and $E_i = \sqrt{p^2 + m_i^2}$, m_i being the mass of particle. The plus sign corresponds to fermions and minus sign to bosons. The chemical potential for particle species i in this case is given by

$$\mu_i = B_i \mu_B + Q_i \mu_Q + S_i \mu_S, \quad (8)$$

where B_i , S_i , and Q_i are the baryon number, strangeness, and charge number, respectively, of hadron species i , and μ_B , μ_Q , and μ_S are the respective chemical potentials. The particle multiplicities are given by

$$N_i^{GC} = T \frac{\partial \ln Z^{GC}}{\partial \mu_i} = \frac{g_i V}{2\pi^2} \sum_{k=1}^{\infty} (\mp 1)^{k+1} \frac{m_i^2 T}{k} K_2 \left(\frac{k m_i}{T} \right) \times e^{\beta k \mu_i} \quad (9)$$

where K_2 is the Bessel function of second order. In the strangeness or mixed canonical ensemble, the partition function for a Boltzmann hadron gas is given by

$$Z_S = \frac{1}{2\pi} \int_{-\pi}^{\pi} d\phi_S e^{-i S \phi_S} \exp \left[\sum_{\text{hadrons } i} \frac{g_i V}{(2\pi)^3} \int d^3p e^{-\beta(E_i - \mu_i)} e^{i S_i \phi_S} \right] \quad (10)$$

In this case, the chemical potential of hadron species i is given by

$$\mu_i = B_i \mu_B + Q_i \mu_Q \quad (11)$$

and particle multiplicities are given by

$$N_i^S = \left(\frac{Z_{S-S_i}}{Z_S} \right) N_i^{GC} \Big|_{\mu_S=0} \quad (12)$$

The main fit parameters obtained are chemical freeze-out temperature T_{ch} , baryon chemical potential μ_B , strange chemical potential μ_S , strangeness suppression factor γ_S (to account for observed deviation from chemical equilibrium in the strangeness sector) [81–86], and (canonical) radius parameter (R_C) R . For fitting in strangeness canonical ensemble, we have fixed $R_C = R$. The results presented here are obtained with fixed $\mu_Q = 0$. Tables VIII and IX show the fit parameters obtained in

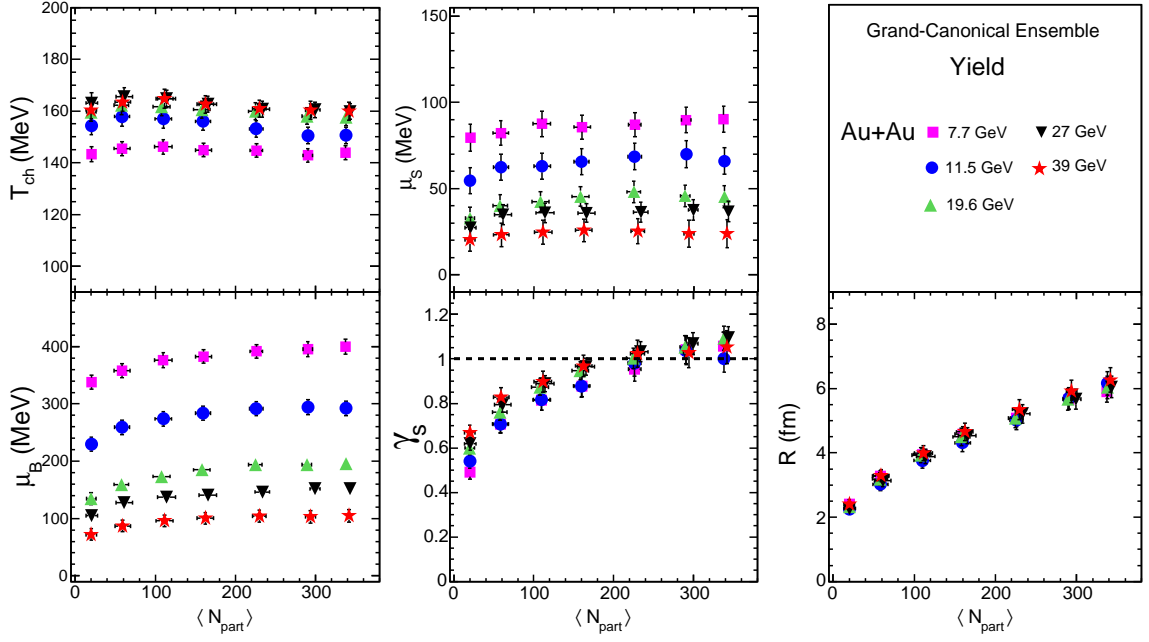


FIG. 27: Chemical freeze-out parameters (T_{ch} , μ_B , μ_S , γ_S , and R) plotted versus $\langle N_{\text{part}} \rangle$ in GCE for particle yields fit. Uncertainties represent systematic errors.

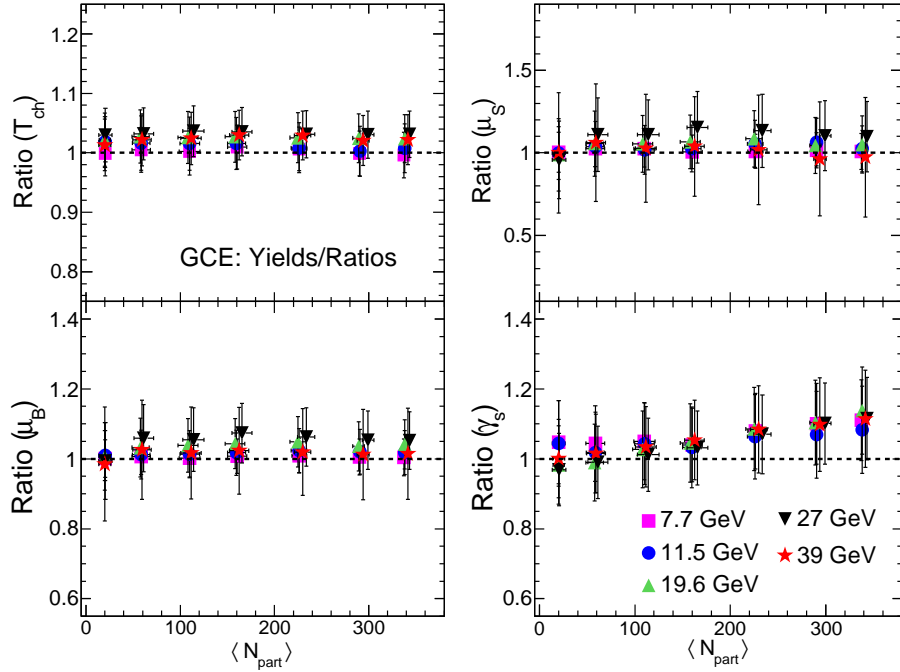


FIG. 28: Ratio of chemical freeze-out parameters (T_{ch} , μ_B , μ_S , and γ_S) between results from particle yield fits to particle ratio fits in GCE plotted versus $\langle N_{\text{part}} \rangle$. Uncertainties represent systematic errors.

Au+Au collisions at $\sqrt{s_{NN}} = 7.7, 11.5, 19.6, 27, 39, 62.4$, and 200 GeV, in various centralities for GCE and SCE, respectively.

Figures 25 and 26 show the GCE and SCE model fits along with standard deviations for Au+Au 7.7 and 39 GeV in 0–5% central collisions, respectively. Upper panels are for the particle yields and lower panels are for particle ratios fit. The plots show that fits for particle yields and ratios are within 2 standard deviations.

Figure 27 shows the extracted chemical freeze-out parameters (T_{ch} , μ_B , μ_S , γ_S , and R) plotted versus $\langle N_{\text{part}} \rangle$ in GCE for particle yields fit. The results are shown for 7.7, 11.5, 19.6, 27, and 39 GeV. We observe that T_{ch} increases from 7.7 to 19.6 GeV and then remains almost constant. For a given energy, the value of T_{ch} is almost the same for all centralities. Baryon chemical potential μ_B decreases with increasing energy and shows centrality dependence for a given energy. The centrality dependence

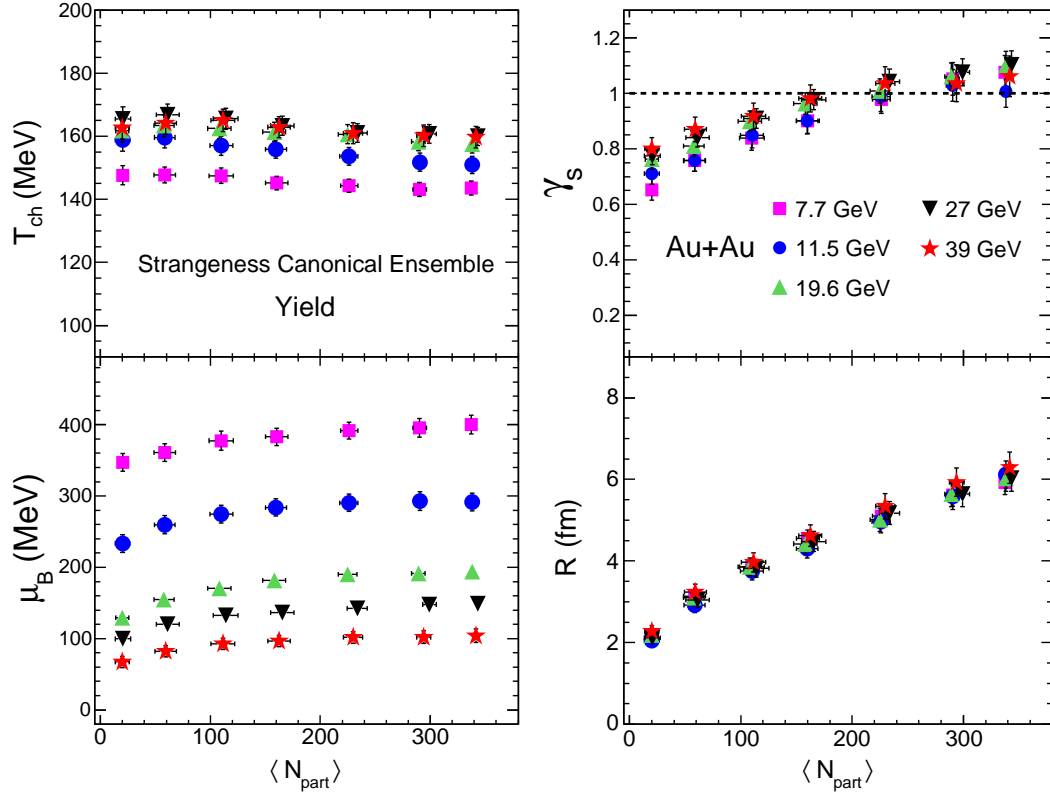


FIG. 29: Chemical freeze-out parameters (T_{ch} , μ_B , γ_S , and R) plotted versus $\langle N_{\text{part}} \rangle$ in SCE for particle yields fit. Uncertainties represent systematic errors.

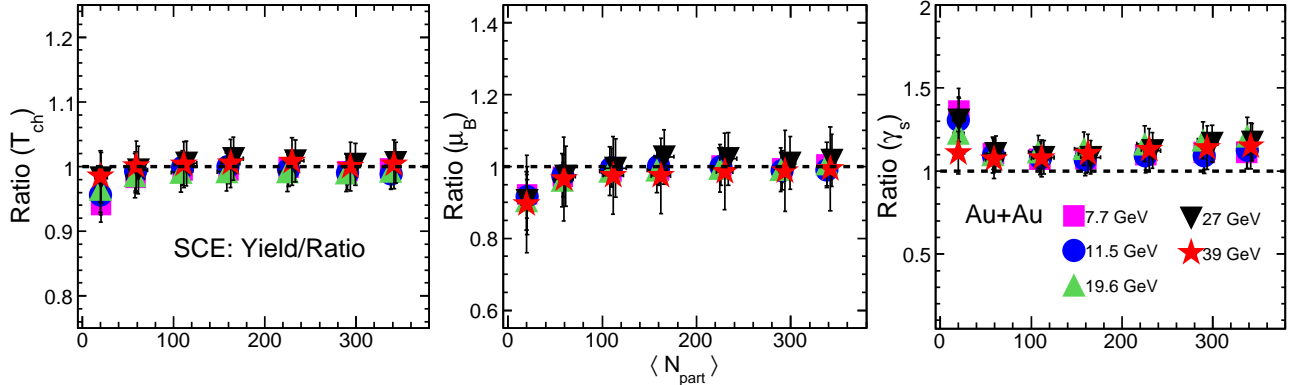


FIG. 30: Ratio of chemical freeze-out parameters (T_{ch} , μ_B , and γ_S) between yield and ratio fits in SCE plotted versus $\langle N_{\text{part}} \rangle$. Uncertainties represent systematic errors.

dence of μ_B is more significant at lower energies (7.7–19.6 GeV). The μ_B increases from peripheral to central collisions. This behavior is likely due to the stronger baryon stopping at lower energies which may also be centrality dependent. The strangeness chemical potential μ_S decreases with increasing energy and also shows a weak increase from peripheral to central collisions. The strangeness suppression factor γ_S accounts for the possible deviations of strange particle abundances from chemical equilibrium; γ_S equal to unity means chemical equilibration of strange particles. The strangeness suppression factor γ_S for central collisions is almost the same and close to unity for all the energies. However, for peripheral

collisions, it is less than unity and shows a slight energy dependence, i.e. decreases with decreasing energy. For a given energy, it increases from peripheral to central collisions. The radius parameter R is related to the volume of the fireball at chemical freeze-out and is obtained for the yield fit case. For the BES energy range, the radius parameter shows no energy dependence. We note a similar energy dependence of the volume at chemical freeze-out per unit of rapidity dV/dy for the energy range similar to BES, as discussed in Ref. [7]. For higher energies, the dV/dy increases. The radius parameter shows centrality dependence for a given energy, increasing from peripheral to central collisions.

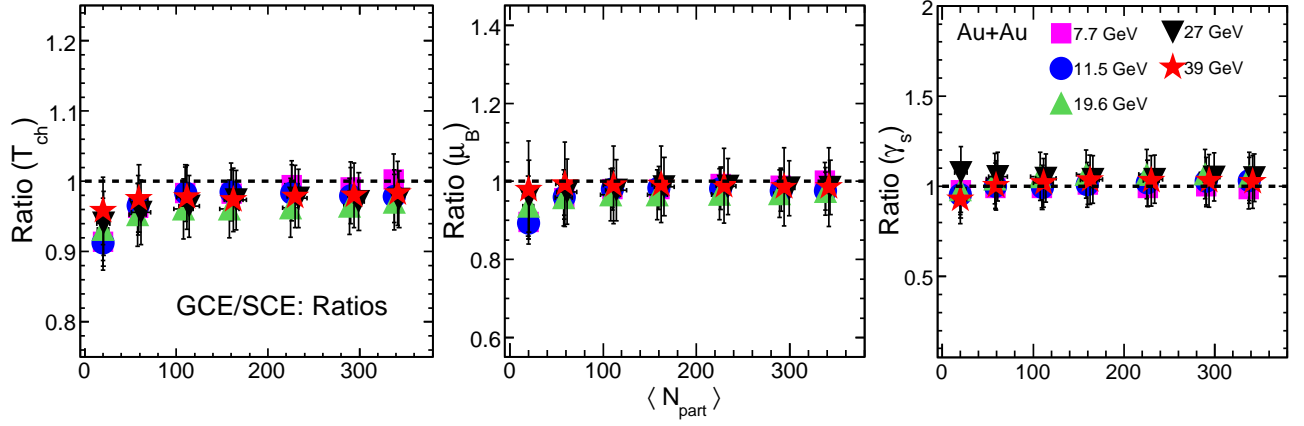


FIG. 31: Ratio of chemical freeze-out parameters (T_{ch} , μ_B , and γ_S) between GCE and SCE results using particle ratios in fits plotted versus $\langle N_{\text{part}} \rangle$. Uncertainties represent systematic errors.

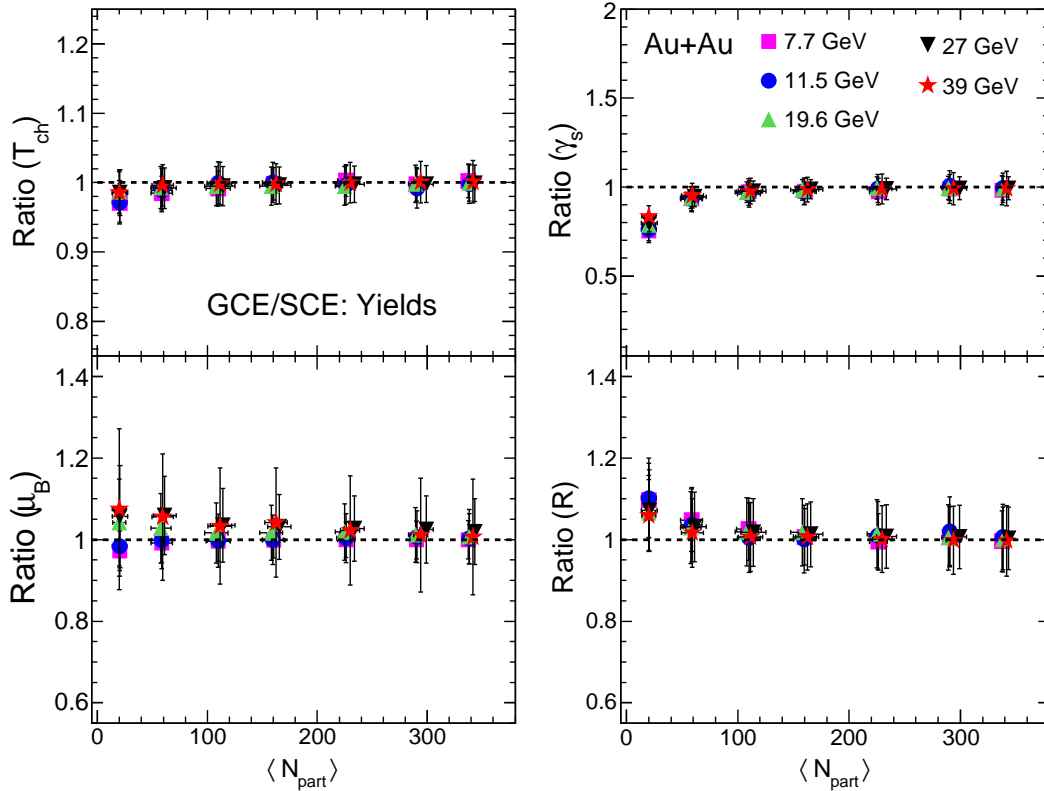


FIG. 32: Ratio of chemical freeze-out parameters (T_{ch} , μ_B , γ_S , and R) between GCE and SCE results using particle yields in fits plotted versus $\langle N_{\text{part}} \rangle$. Uncertainties represent systematic errors.

Figure 28 shows the ratio of chemical freeze-out parameters (T_{ch} , μ_B , μ_S , γ_S , and R) between results from yield fits to ratio fits in GCE plotted versus $\langle N_{\text{part}} \rangle$. We observe that the extracted freeze-out parameters for GCE using ratio and yield fits are consistent with each other within uncertainties. We found that the results using particle ratios in the fits have large uncertainties compared to those using particle yields. This may be because the particle ratios used for fitting are constructed mostly using common particle yields, say e.g. pions, which leads to correlated uncertainties, but we treated all the ratio uncertainties as independent in our fit.

Figure 29 shows the chemical freeze-out parameters (T_{ch} , μ_B , γ_S , and R) plotted versus $\langle N_{\text{part}} \rangle$ in SCE for particle yields fit. The behavior of the freeze-out parameters is generally similar to what we discussed above for GCE. However, T_{ch} in SCE seems to be higher in peripheral collisions, but the centrality dependence is still weak. Figure 30 shows the ratio of chemical freeze-out parameters (T_{ch} , μ_B , and γ_S) between yield and ratio fits in SCE plotted versus $\langle N_{\text{part}} \rangle$. We observe that within uncertainties, the results using yield and ratio fits are similar except for γ_S in the most peripheral collision.

Figure 31 shows the ratio of chemical freeze-out pa-

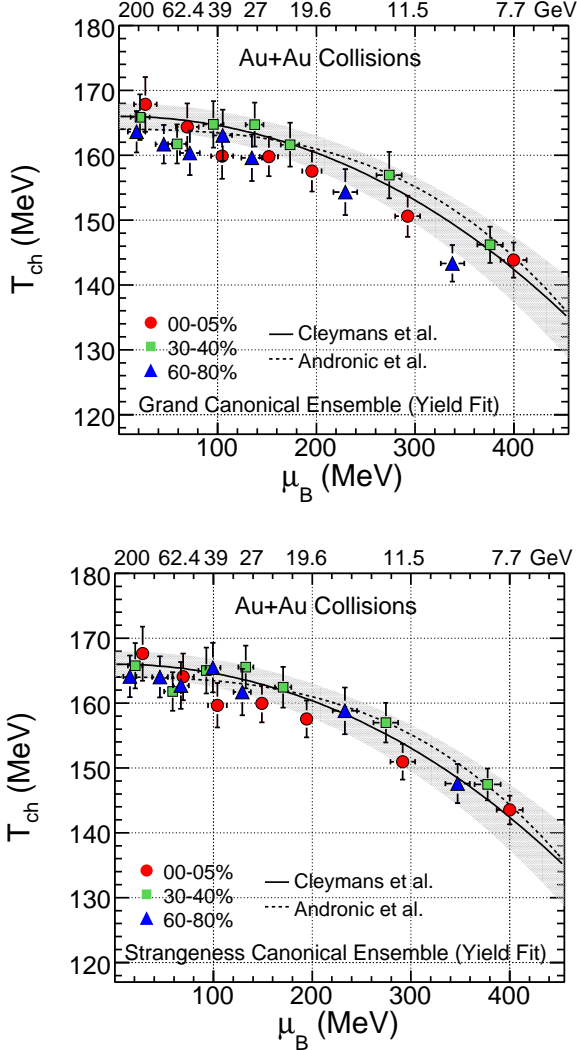


FIG. 33: Extracted chemical freeze-out temperature versus baryon chemical potential for GCE (top panel) and SCE (bottom panel) cases using particle yields as input for fitting. Curves represent two model predictions [79, 80]. Uncertainties represent systematic errors.

rameters (T_{ch} , μ_B , and γ_S) between GCE and SCE results obtained using the particle ratio fit plotted versus $\langle N_{\text{part}} \rangle$. Similarly, Fig. 32 shows the ratio of chemical freeze-out parameters (T_{ch} , μ_B , γ_S , and R) between GCE and SCE results obtained using particle yields fit plotted versus $\langle N_{\text{part}} \rangle$. We observe that the results are consistent within uncertainties for GCE and SCE using both the ratio and yield fits, except for γ_S in the most peripheral collision in case of yields fit.

Figure 33 shows the variation of chemical freeze-out temperature with baryon chemical potential at various energies and for three centralities 0–5%, 30–40% and 60–80%. For 62.4 GeV, the three centralities shown are 0–5%, 20–40% and 60–80%. The results are shown for both GCE (top panel) and SCE (bottom panel) cases obtained using particle yields fit. The curves represent two model predictions [79, 80]. In general, the behavior

is the same for the two cases, i.e. a centrality dependence of baryon chemical potential is observed which is significant at lower energies.

Next, we test the robustness of our results by comparing to results obtained with different constraints and using more particles in the fit.

1. Choice on Constraints

The results presented here are obtained assuming $\mu_Q = 0$. However, we have checked the results by constraining μ_Q to the initial baryon-to-charge ratio for Au+Au collisions, i.e. $B/2Q=1.25$. We have also checked the results by applying both constraints, i.e. μ_Q constrained to 1.25 as well as μ_S constrained to initial strangeness density, i.e. 0. Figure 34 shows the extracted chemical freeze-out temperature (upper panels) and baryon chemical potential (lower panels) in Au+Au collisions at $\sqrt{s_{NN}}=7.7$, 19.6, and 39 GeV for GCE using particle yields as input to the fit, for the three conditions mentioned above. It is observed that these three different conditions have negligible effect ($< 1\%$) on the final extracted T_{ch} and μ_B . The extracted parameters are similar for these different cases. Similarly, μ_S , the radius parameter, γ_S , and χ^2/NDF (plots not shown here), all show similar results for the three cases discussed above. The same exercise was repeated for the SCE case and the conclusion remains the same.

2. Choice on Including More Particles

For the default results discussed above, the particles included in the THERMUS fit are: π , K , p , \bar{p} , Λ , and Ξ . It is interesting to compare the freeze-out parameters extracted using different particles sets in the thermal fit. Figure 35 shows the comparison of extracted freeze-out parameters in Au+Au collisions at $\sqrt{s_{NN}} = 39$ GeV for GCE using yields as input to the fit. Results are compared for four different sets of particle yields used as input for fitting. When only π , K and p yields are used in fit, the temperature obtained is lower compared to other sets that include strange hadron yields. Also, γ_S is less than unity, even for central collisions. It can be seen that for all other cases, the results are similar within uncertainties. However, the χ^2/NDF increases with increasing number of particles used for fitting.

B. Kinetic Freeze-out

The kinetic freeze-out parameters are obtained by fitting the spectra with a blast wave model. The model assumes that the particles are locally thermalized at a kinetic freeze-out temperature and are moving with a common transverse collective flow velocity [43, 51]. Assuming a radially boosted thermal source, with a kinetic

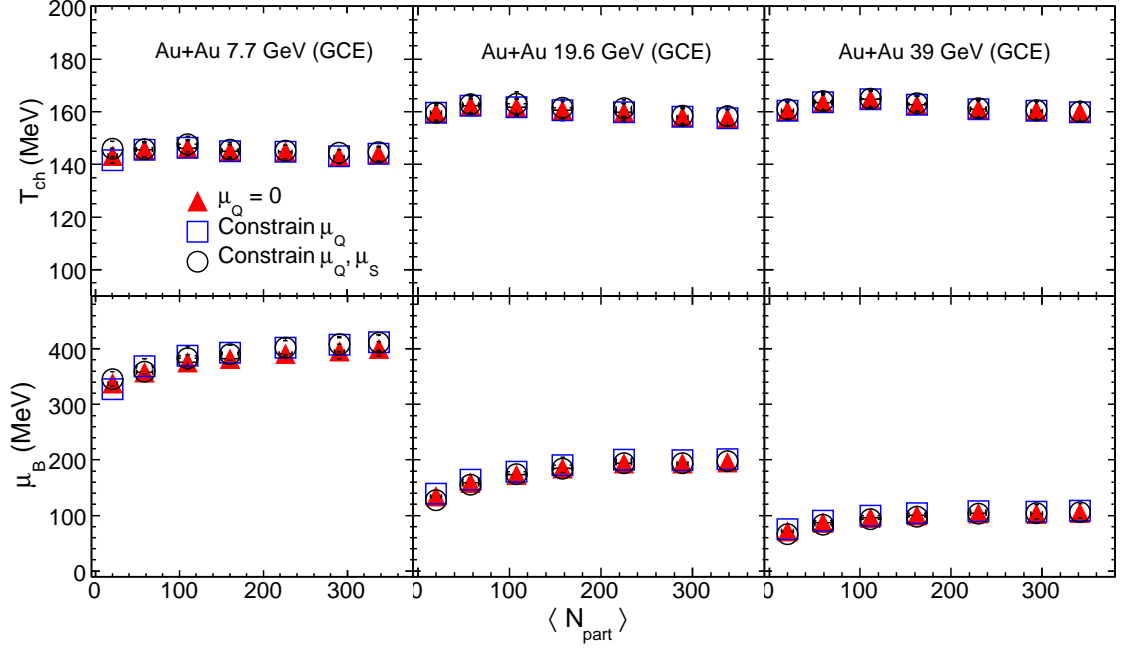


FIG. 34: *Choice on constraints*: Extracted chemical freeze-out temperature (top panels) and baryon chemical potential (bottom panels) for GCE using particle yields as input for fitting. Results are compared for Au+Au collisions at $\sqrt{s_{NN}} = 7.7, 19.6$, and 39 GeV for three initial conditions: $\mu_Q = 0$, μ_Q constrained to $B/2Q$ value, and μ_Q constrained to $B/2Q$ along with μ_S constrained to 0. Uncertainties represent systematic errors.

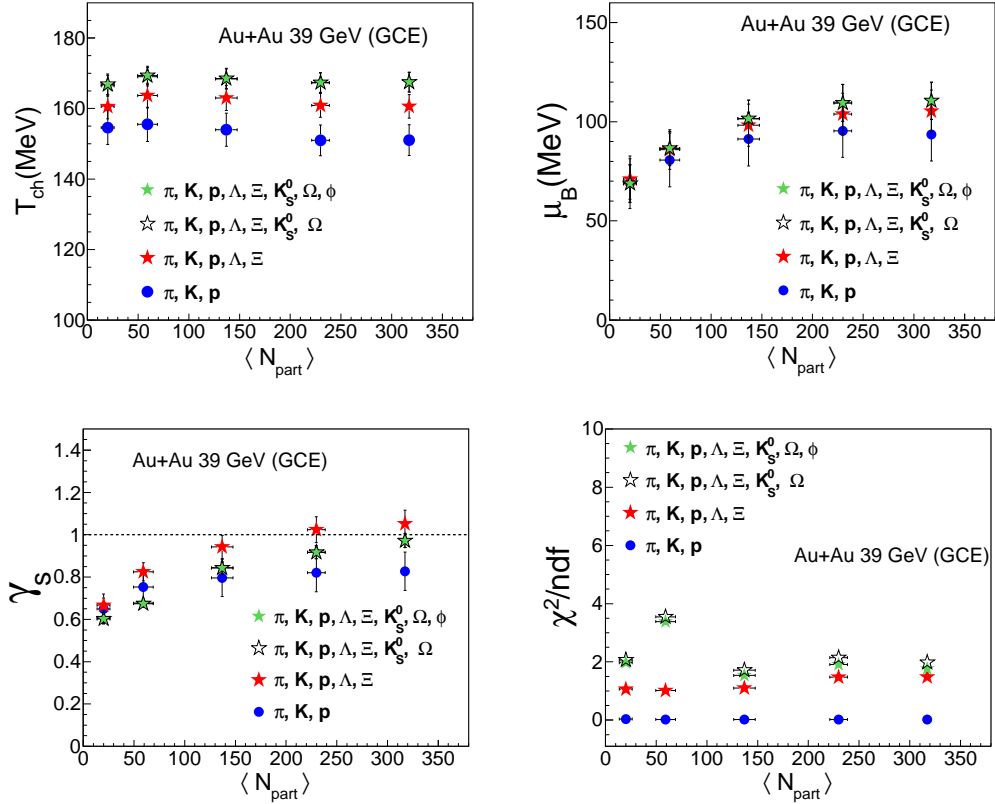


FIG. 35: *Choice on including more particles*: Extracted chemical freeze-out parameters for GCE using particle yields as input for fitting. Results are compared for Au+Au collisions at $\sqrt{s_{NN}} = 39$ GeV for four different sets of particle yields used in fitting. Uncertainties represent systematic errors.

freeze-out temperature T_{kin} and a transverse radial flow velocity β , the p_T distribution of the particles is given by [51]

$$\frac{dN}{p_T dp_T} \propto \int_0^R r dr m_T I_0 \left(\frac{p_T \sinh \rho(r)}{T_{\text{kin}}} \right) \times K_1 \left(\frac{m_T \cosh \rho(r)}{T_{\text{kin}}} \right), \quad (13)$$

where m_T is the transverse mass of a hadron, $\rho(r) = \tanh^{-1} \beta$, and I_0 and K_1 are the modified Bessel functions. We use a radial flow velocity profile of the form

$$\beta = \beta_S (r/R)^n, \quad (14)$$

where β_S is the surface velocity, r/R is the relative radial position in the thermal source, and n is the exponent of flow velocity profile. Average transverse radial flow velocity $\langle \beta \rangle$ can then be obtained from $\langle \beta \rangle = \frac{2}{2+n} \beta_S$. Usually π^\pm , K^\pm , p , and \bar{p} particle spectra are fitted simultaneously with the blast-wave model. Including more particles such as multi-strange hadrons in the fit would amount to forcing all the species to freeze-out at the same time which may not be true. It has been shown at top RHIC energy that the spectra of multi-strange particles reflect a higher kinetic freeze-out temperature [4, 87]. This can be interpreted as diminished hadronic interactions with the expanding bulk matter after chemical freeze-out. For the results presented here for kinetic freeze-out, we use π^\pm , K^\pm , p , and \bar{p} spectra in the blast-wave model fit. We also note the recent study of separate fit of positively and negatively charged particles v_2 using a blast wave model [88, 89].

Figure 36 shows the blast wave model fits of π^\pm , K^\pm , and p and (\bar{p}) p_T spectra in 0–5% central Au+Au collisions at $\sqrt{s_{NN}} = 7.7, 11.5, 19.6, 27$, and 39 GeV. The model describes well the p_T spectra of π^\pm, K^\pm, p , and \bar{p} at all energies studied. The fit parameters are T_{kin} , $\langle \beta \rangle$, and n . The low p_T part of the pion spectra is affected by resonance decays, and consequently the pion spectra are fitted only for $p_T > 0.5$ GeV/c. The blast wave model is hydrodynamics-motivated which provides a good description of data at low p_T , but is not suited for describing hard processes at high p_T [90]. Thus the blast wave model results are sensitive to the p_T fit ranges used for fitting [66]. The results presented here use similar values of low p_T as were used in previous studies by STAR and ALICE [43, 66]. We keep consistent p_T ranges for simultaneous fitting of the π^\pm, K^\pm, p , and \bar{p} spectra across all the BES energies as shown in Fig. 36. The extracted kinetic freeze-out parameters for the BES energies are listed in Table X.

Figure 37 shows the variation of T_{kin} with $\langle \beta \rangle$ for different energies and centralities. The $\langle \beta \rangle$ decreases from central to peripheral collisions indicating more rapid expansion in central collisions. On the other hand, T_{kin} increases from central to peripheral collisions, consistent with the expectation of a shorter-lived fireball in

peripheral collisions [91]. Furthermore, we observe that these parameters show a two-dimensional anti-correlation band. Higher values of T_{kin} correspond to lower values of $\langle \beta \rangle$ and vice-versa.

Figure 38 (upper panel) shows the energy dependence of kinetic and chemical freeze-out temperatures for central heavy-ion collisions. We observe that the values of kinetic and chemical freeze-out temperatures are similar around $\sqrt{s_{NN}} = 4 - 5$ GeV. If the collision energy is increased, the chemical freeze-out temperature increases and becomes constant after $\sqrt{s_{NN}} = 11.5$ GeV. On the other hand, T_{kin} is almost constant around the 7.7–39 GeV and then decreases up to LHC energies. The separation between T_{ch} and T_{kin} increases with increasing energy. This might suggest the effect of increasing hadronic interactions between chemical and kinetic freeze-out at higher energies [4]. Figure 38 (lower panel) shows the average transverse radial flow velocity plotted as a function of $\sqrt{s_{NN}}$. The $\langle \beta \rangle$ shows a rapid increase at very low energies, then a steady increase up to LHC energies. The $\langle \beta \rangle$ is almost constant for the lowest three BES energies.

VII. SUMMARY AND CONCLUSIONS

We have presented measurements of identified particles π, K, p , and \bar{p} at midrapidity ($|y| < 0.1$) in Au+Au collisions at $\sqrt{s_{NN}} = 7.7, 11.5, 19.6, 27$, and 39 GeV from the beam energy scan program at RHIC. The transverse momentum spectra of pions, kaons, protons, and anti-protons are presented for 0–5%, 5–10%, 10–20%, 20–30%, 30–40%, 40–50%, 50–60%, 60–70%, and 70–80% collision centrality classes. The bulk properties are studied by measuring the identified hadron $dN/dy, \langle p_T \rangle$, particle ratios, and freeze-out parameters. The results are compared with corresponding published results from other energies and experiments.

The yields of charged pions, kaons, and anti-protons decrease with decreasing collision energy. However, the yield of protons is higher for the lowest energy of 7.7 GeV which suggests high baryon stopping at mid-rapidity at lower energies. The yields decrease from central to peripheral collisions for π^\pm, K^\pm , and p . However, the centrality dependence of yields for \bar{p} is weak. The energy dependence of pion yields changes slope as a function of beam energy. The slope above 19.6 GeV is different when compared to that at lower energies. This may suggest a change in particle production mechanism below 19.6 GeV.

The π^-/π^+ ratio is close to unity for most of the energies. The lowest energy of 7.7 GeV has a greater π^-/π^+ ratio than at other energies due to isospin and significant contributions from resonance decays (such as Δ baryons). The K^-/K^+ ratio increases with increasing energy, and shows very little centrality dependence. The increase in K^-/K^+ ratio with energy shows the increasing contribution to kaon production due to pair production. The K^+/π^+ ratio shows a maximum at 7.7 GeV and then

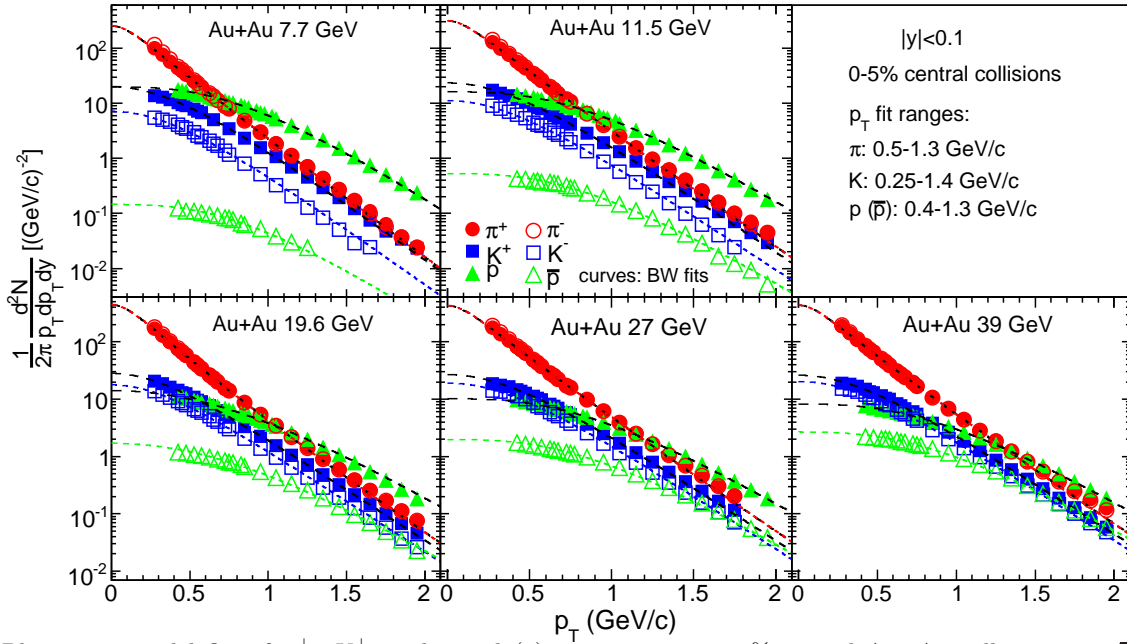


FIG. 36: Blast wave model fits of π^\pm , K^\pm , and p and \bar{p} p_T spectra in 0-5% central Au+Au collisions at $\sqrt{s_{NN}} = 7.7, 11.5, 19.6, 27$, and 39 GeV. Uncertainties on experimental data represent statistical and systematic uncertainties added in quadrature. Here, the uncertainties are smaller than the symbol size.

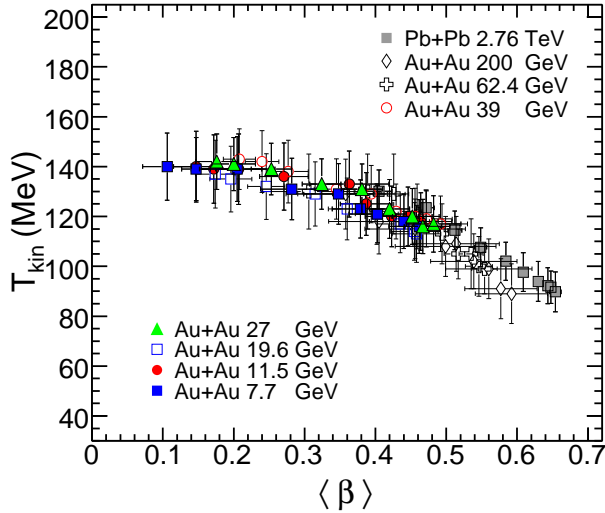


FIG. 37: Variation of T_{kin} with $\langle\beta\rangle$ for different energies and centralities. The centrality increases from left to right for a given energy. The data points other than BES energies are taken from Refs. [43, 66]. Uncertainties represent systematic uncertainties.

decreases with increasing energy. This is due to the associated production dominance at lower energies as the baryon stopping is large. This maximum corresponds to the maximum baryon density predicted to be achieved in heavy-ion collisions. The centrality dependence is similar at all energies, increasing from peripheral to central collisions. The \bar{p}/p ratio increases with increasing energy. The ratio increases from central to peripheral collisions. The results reflect the large baryon stopping at

mid-rapidity at lower energies in central collisions. The p/π^+ ratio decreases with increasing energy and is larger at $\sqrt{s_{NN}} = 7.7$ GeV. This is again a consequence of the higher degree of baryon stopping for the collisions at lower energies compared to $\sqrt{s_{NN}} = 62.4$ and 200 GeV.

The $\langle m_T \rangle - m$ values increase with $\sqrt{s_{NN}}$ at lower AGS energies, stay independent of $\sqrt{s_{NN}}$ at the SPS and BES energies, then tend to rise further with increasing $\sqrt{s_{NN}}$ at the higher beam energies at RHIC. The constant value of $\langle m_T \rangle - m$ vs. $\sqrt{s_{NN}}$ around BES energies could be interpreted as reflecting the formation of a mixed phase of a QGP and hadrons during the evolution of the heavy-ion system.

The chemical freeze-out parameters are extracted from a thermal model fit to the data at midrapidity. The GCE and SCE approaches are studied by fitting the particle yields as well as the particle ratios. The results for particle yield fits compared to particle ratio fits are consistent within uncertainties for both GCE and SCE. The GCE and SCE results are also consistent with each other for either ratio or yield fits. The SCE results obtained by fitting particle yields seem to give slightly higher temperature towards peripheral collisions compared to that in 0-5% central collisions. The chemical freeze-out parameter T_{ch} increases from 7.7 to 19.6 GeV; after that it remains almost constant. For a given energy, the value of T_{ch} is similar for all centralities. In all the cases studied, the centrality dependence of baryon chemical potential is observed which is significant at lower energies.

The kinetic freeze-out parameters are extracted from a blast-wave model fit to pion, kaon, proton, and anti-proton p_T spectra. T_{kin} increases from central to peripheral collisions suggesting a longer lived fireball in central

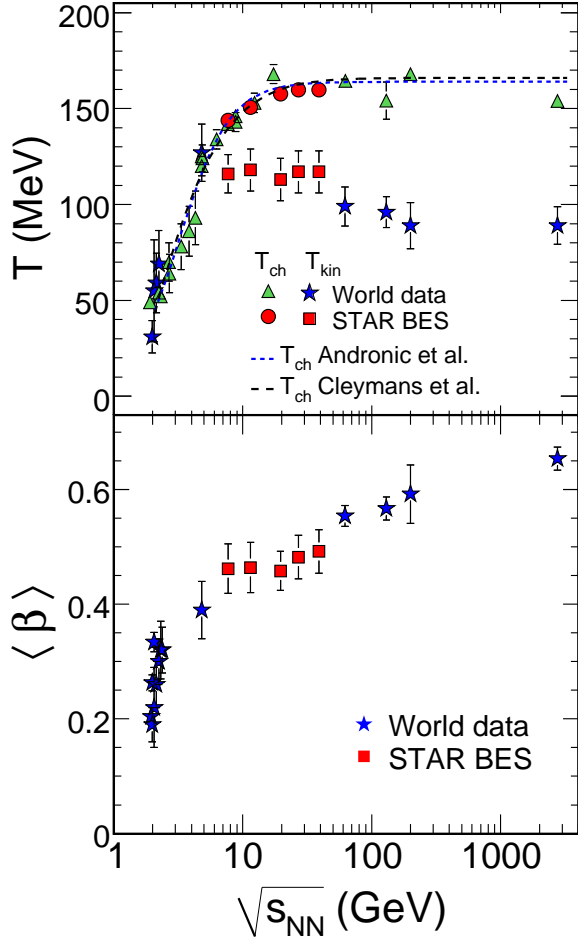


FIG. 38: Top: Energy dependence of kinetic and chemical freeze-out temperatures for central heavy-ion collisions. The curves represent various theoretical predictions [79, 80]. Bottom: Energy dependence of average transverse radial flow velocity for central heavy-ion collisions. The data points other than BES energies are taken from Refs. [43, 53–64, 66] and references therein. The BES data points are for 0–5% central collisions, AGS energies are mostly for 0–5%, SPS energies for mostly 0–7%, and top RHIC and LHC energies for 0–5% central collisions. Uncertainties represent systematic uncertainties.

collisions, while $\langle\beta\rangle$ decreases from central to peripheral collisions suggesting stronger expansion in central collisions. Furthermore, we observe that these parameters show a two-dimensional anti-correlation band. Higher values of T_{kin} correspond to lower values of $\langle\beta\rangle$ and vice-versa. The separation between T_{ch} and T_{kin} increases

with increasing energy. This might suggest the effect of increasing hadronic interactions between chemical and kinetic freeze-out at higher energies. The $\langle\beta\rangle$ shows a rapid increase at very low energies, then a slow increase across the BES energies, after which it again increases steadily up to LHC energies.

In conclusion we have studied the bulk properties of matter in the Beam Energy Scan program at RHIC. The BES program covers the energy range from 7.7 GeV to 39 GeV which along with top RHIC energy corresponds to the baryon chemical potential region of 20–400 MeV. The mid-rapidity yields of identified hadrons have been presented. They show the expected signatures of a high-baryon stopping region at lower energies. At high energies, the pair production mechanism dominates the particle production. At intermediate energies there is clearly a transition between these two regions, which is explored by the BES Program.

The data have been used to analyse both chemical and kinetic freeze-out parameters. The chemical freeze-out was studied using both GCE and SCE approaches, and the fits were performed using both particle yields and particle ratios. The results show no significant difference between these approaches, but indicate in heavy-ion collisions a clear centrality dependence of the baryon chemical potential at lower energies. The centrality dependence of the freeze-out parameters provides an opportunity for the BES program at RHIC to enlarge the (T, μ_B) region of the phase diagram to search for the QCD critical point. The difference between chemical and kinetic freeze-out increases with increasing energy suggesting increasing hadronic interactions after chemical freeze-out at higher energies. We thank the RHIC Operations Group and RCF at BNL, the NERSC Center at LBNL, and the Open Science Grid consortium for providing resources and support. This work was supported in part by the Office of Nuclear Physics within the U.S. DOE Office of Science, the U.S. National Science Foundation, the Ministry of Education and Science of the Russian Federation, National Natural Science Foundation of China, Chinese Academy of Science, the Ministry of Science and Technology of China and the Chinese Ministry of Education, the National Research Foundation of Korea, GA and MSMF of the Czech Republic, Department of Atomic Energy and Department of Science and Technology of the Government of India; the National Science Centre of Poland, National Research Foundation, the Ministry of Science, Education and Sports of the Republic of Croatia, RosAtom of Russia and German Bundesministerium für Bildung, Wissenschaft, Forschung und Technologie (BMBF) and the Helmholtz Association.

[1] I. Arsene *et al.* (BRAHMS Collaboration), Nucl. Phys. **A 757**, 1 (2005).

[2] K. Adcox *et al.* (PHENIX Collaboration), Nucl. Phys. **A 757**, 184 (2005).

- [3] B. B. Back *et al.* (PHOBOS Collaboration), Nucl. Phys. **A 757**, 28 (2005).
- [4] J. Adams *et al.* (STAR Collaboration), Nucl. Phys. **A 757**, 102 (2005).
- [5] J. Cleymans and K. Redlich, Phys. Rev. **C 60**, 054908 (1999).
- [6] F. Becattini, J. Manninen, and M. Gazdzicki, Phys. Rev. **C 73**, 044905 (2006).
- [7] A. Andronic, P. Braun-Munzinger, and J. Stachel, Nucl. Phys. **A 772**, 167 (2006).
- [8] K. Rajagopal and F. Wilczek, arXiv hep-ph/0011333 (2000).
- [9] E. Laermann and O. Philipsen, Ann. Rev. Nucl. Part. Sci. **53**, 163 (2003).
- [10] M. Stephanov, PoS **LAT2006**, 024 (2006).
- [11] J. Adams *et al.* (STAR Collaboration), Phys. Rev. Lett. **91**, 072304 (2003).
- [12] J. Adams *et al.* (STAR Collaboration), Phys. Rev. Lett. **91**, 172302 (2003).
- [13] B. Abelev *et al.* (STAR Collaboration), Phys. Rev. Lett. **97**, 152301 (2006).
- [14] B. Abelev *et al.* (STAR Collaboration), Phys. Lett. **B 655**, 104 (2007).
- [15] B. Abelev *et al.* (STAR Collaboration), Phys. Rev. Lett. **99**, 112301 (2007).
- [16] B. Abelev *et al.* (STAR Collaboration), Phys. Rev. **C 77**, 054901 (2008).
- [17] J. Adams *et al.* (STAR Collaboration), Phys. Rev. Lett. **95**, 122301 (2005).
- [18] Y. Aoki, G. Endrodi, Z. Fodor, S. Katz, and K. Szabo, Nature **443**, 675 (2006).
- [19] M. Cheng *et al.*, Phys. Rev. **D 77**, 014511 (2008).
- [20] S. Ejiri, Phys. Rev. **D 78**, 074507 (2008).
- [21] M. Asakawa and K. Yazaki, Nucl. Phys. **A 504**, 668 (1989).
- [22] A. Barducci, R. Casalbuoni, S. De Curtis, R. Gatto, and G. Pettini, Phys. Lett. **B 231**, 463 (1989).
- [23] A. Barducci, R. Casalbuoni, S. De Curtis, R. Gatto, and G. Pettini, Phys. Rev. **D 41**, 1610 (1990).
- [24] M. A. Stephanov, Prog. Theor. Phys. Suppl. **153**, 139 (2004).
- [25] Z. Fodor and S. Katz, JHEP **04**, 050 (2004).
- [26] R. Gavai and S. Gupta, Phys. Rev. **D 78**, 114503 (2008).
- [27] B. Abelev *et al.* (STAR Collaboration), Phys. Rev. **C 81**, 024911 (2010).
- [28] B. Mohanty, Nucl. Phys. **A 830**, 899c (2009).
- [29] M. Aggarwal *et al.* (STAR Collaboration), arXiv: p. 1007.2613 (2010).
- [30] L. Kumar (STAR Collaboration), Nucl. Phys. **A 904**, 256c (2013).
- [31] L. Kumar, Mod. Phys. Lett. **A 28**, 1330033 (2013).
- [32] M. A. Stephanov, Phys. Rev. Lett. **102**, 032301 (2009).
- [33] M. M. Aggarwal *et al.* (STAR Collaboration), Phys. Rev. Lett. **105**, 022302 (2010).
- [34] F. Karsch and K. Redlich, Phys. Lett. **B 695**, 136 (2011).
- [35] S. Gupta, X. Luo, B. Mohanty, H. G. Ritter, and N. Xu, Science **332**, 1525 (2011).
- [36] K. Ackermann *et al.* (STAR Collaboration), Nucl. Instrum. Meth. **A 499**, 624 (2003).
- [37] C. Adler *et al.*, Nucl. Instrum. Meth. **A 470**, 488 (2001).
- [38] W. Llope *et al.*, Nucl. Instrum. Meth. **A 522**, 252 (2004).
- [39] F. Bieser *et al.*, Nucl. Instrum. Meth. **A 499**, 766 (2003).
- [40] C. A. Whitten, Amer. Inst. Phys. Conf. Ser. **980**, 390 (2008).
- [41] M. Anderson *et al.*, Nucl. Instrum. Meth. **A 499**, 659 (2003).
- [42] W. Llope, Nucl. Instrum. Meth. **B 241**, 306 (2005).
- [43] B. Abelev *et al.* (STAR Collaboration), Phys. Rev. **C 79**, 034909 (2009).
- [44] H. Bichsel, Nucl. Instrum. Meth. **A 562**, 154 (2006).
- [45] M. Aguilar-Benitez *et al.*, Z. Phys. **C 50**, 405 (1991).
- [46] V. Fine and P. Nevski, Proc. CHEP **2000**, 143 (2000).
- [47] J. Adams *et al.* (STAR Collaboration), Phys. Rev. **C 70**, 041901 (2004).
- [48] J. Adams *et al.* (STAR Collaboration), Phys. Rev. Lett. **92**, 112301 (2004).
- [49] M. M. Aggarwal *et al.* (STAR), Phys. Rev. **C83**, 034910 (2011), 1008.3133.
- [50] S. Wheaton, J. Cleymans, and M. Hauer, Comput. Phys. Commun. **180**, 84 (2009).
- [51] E. Schnedermann, J. Sollfrank, and U. W. Heinz, Phys. Rev. **C 48**, 2462 (1993).
- [52] J. Cleymans, H. Oeschler, K. Redlich, and S. Wheaton, Eur. Phys. J. **A 29**, 119 (2006).
- [53] Y. Akiba *et al.* (E802 Collaboration), Nucl. Phys. **A 610**, 139c (1996).
- [54] L. Ahle *et al.* (E802 Collaboration), Phys. Rev. **C 57**, 466 (1998).
- [55] L. Ahle *et al.* (E866 Collaboration, E917 Collaboration), Phys. Lett. **B 476**, 1 (2000).
- [56] J. Barrette *et al.* (E877 Collaboration), Phys. Rev. **C 62**, 024901 (2000).
- [57] L. Ahle *et al.* (E802 Collaboration), Phys. Rev. **C 60**, 064901 (1999).
- [58] L. Ahle *et al.* (E802 Collaboration, E866 Collaboration), Phys. Rev. **C 60**, 044904 (1999).
- [59] L. Ahle *et al.* (E866 Collaboration, E917 Collaborations), Phys. Lett. **B 490**, 53 (2000).
- [60] J. Klay *et al.* (E895 Collaboration), Phys. Rev. Lett. **88**, 102301 (2002).
- [61] S. Afanasiev *et al.* (NA49 Collaboration), Phys. Rev. **C 66**, 054902 (2002).
- [62] T. Anticic *et al.* (NA49 Collaboration), Phys. Rev. **C 69**, 024902 (2004).
- [63] C. Alt *et al.* (NA49 Collaboration), Phys. Rev. **C 73**, 044910 (2006).
- [64] C. Alt *et al.* (NA49 Collaboration), Phys. Rev. **C 77**, 024903 (2008).
- [65] S. Adler *et al.* (PHENIX Collaboration), Phys. Rev. **C 71**, 034908 (2005).
- [66] B. Abelev *et al.* (ALICE Collaboration), Phys. Rev. **C 88**, 044910 (2013).
- [67] L. D. Landau and I. Pomeranchuk, Dokl. Akad. Nauk Ser. Fiz. **92**, 735 (1953).
- [68] Y. Hama and F. S. Navarra, Phys. Lett. **B 129**, 251 (1983).
- [69] L. Van Hove, Phys. Lett. **B 118**, 138 (1982).
- [70] B. Mohanty, J.-e. Alam, S. Sarkar, T. K. Nayak, and B. K. Nandi, Phys. Rev. **C 68**, 021901 (2003).
- [71] J. K. Nayak, J.-e. Alam, P. Roy, A. K. Dutt-Mazumder, and B. Mohanty, Acta Phys. Slov. **56**, 27 (2006).
- [72] B. Tomasik and E. E. Kolomeitsev, Eur. Phys. J. **C 49**, 115 (2007).
- [73] A. Andronic, P. Braun-Munzinger, and J. Stachel, Phys. Lett. **B 673**, 142 (2009).
- [74] J. Rafelski, I. Kuznetsova, and J. Letessier, J. Phys. **G 35**, 044011 (2008).
- [75] S. Chatterjee, R. Godbole, and S. Gupta, Phys. Rev. **C**

- 81**, 044907 (2010).
- [76] W. Busza and A. S. Goldhaber, Phys. Lett. **B 139**, 235 (1984).
 - [77] A. Andronic, F. Beutler, P. Braun-Munzinger, K. Redlich, and J. Stachel, Phys. Lett. **B 675**, 312 (2009).
 - [78] J. Cleymans, D. Elliott, A. Keranen, and E. Suhonen, Phys. Rev. **C 57**, 3319 (1998).
 - [79] J. Cleymans, H. Oeschler, K. Redlich, and S. Wheaton, Phys. Rev. **C 73**, 034905 (2006).
 - [80] A. Andronic, P. Braun-Munzinger, and J. Stachel, Nucl. Phys. **A 834**, 237c (2010).
 - [81] F. Becattini, M. Gazdzicki, and J. Sollfrank, Eur. Phys. J. **C 5**, 143 (1998).
 - [82] F. Becattini, M. Gazdzicki, A. Keranen, J. Manninen, and R. Stock, Phys. Rev. **C 69**, 024905 (2004).
 - [83] I. Bearden *et al.* (NA44 Collaboration), Phys. Rev. **C 66**, 044907 (2002).
 - [84] J. Cleymans, B. Kampfer, and S. Wheaton, Phys. Rev. **C 65**, 027901 (2002).
 - [85] J. Cleymans, B. Kampfer, and S. Wheaton, Nucl. Phys. **A 715**, 553 (2003).
 - [86] J. Cleymans, B. Kampfer, P. Steinberg, and S. Wheaton, J. Phys. **G 30**, S595 (2004).
 - [87] N. Xu and M. Kaneta, Nucl. Phys. **A 698**, 306 (2002).
 - [88] X. Sun, H. Masui, A. M. Poskanzer, and A. Schmah, Phys. Rev. **C 91**, 024903 (2015).
 - [89] L. Adamczyk *et al.* (STAR Collaboration), Phys. Rev. **C 93**, 014907 (2016).
 - [90] G. Wilk and Z. Wlodarczyk, Phys. Rev. Lett. **84**, 2770 (2000).
 - [91] U. W. Heinz, arXiv hep-ph/0407360 (2004).

TABLE VI: Extracted dN/dy values for $|y| < 0.1$ in Au+Au collisions at $\sqrt{s_{NN}} = 7.7, 11.5, 19.6, 27,$ and 39 GeV. Quoted errors in parenthesis are the combined statistical and systematic uncertainties.

$\sqrt{s_{NN}}$ (GeV)	% cross-section	π^+	π^-	K^+	K^-	p	\bar{p}
7.7	00-05	93.4 (8.4)	100 (9.0)	20.8 (1.7)	7.7 (0.6)	54.9 (6.1)	0.39 (0.05)
	05-10	76.8 (6.9)	81.9 (7.4)	17.3 (1.4)	6.4 (0.5)	45.4 (5.0)	0.32 (0.04)
	10-20	58.7 (5.3)	62.9 (5.7)	12.4 (1.0)	4.7 (0.4)	33.4 (3.7)	0.26 (0.03)
	20-30	40.5 (3.7)	43.3 (3.9)	8.6 (0.7)	3.2 (0.3)	23.2 (2.6)	0.19 (0.02)
	30-40	26.9 (2.4)	29.1 (2.6)	5.3 (0.4)	2.1 (0.2)	15.8 (1.7)	0.14 (0.02)
	40-50	17.6 (1.6)	18.8 (1.7)	3.2 (0.3)	1.3 (0.1)	9.3 (1.0)	0.09 (0.01)
	50-60	10.9 (0.9)	11.8 (1.1)	1.8 (0.1)	0.71 (0.06)	5.4 (0.6)	0.06 (0.01)
	60-70	6.1 (0.6)	6.6 (0.6)	0.82 (0.07)	0.32 (0.03)	2.8 (0.3)	0.033 (0.004)
	70-80	3.1 (0.3)	3.4 (0.3)	0.33 (0.03)	0.13 (0.01)	1.4 (0.2)	0.018 (0.002)
11.5	00-05	123.9 (12.4)	129.8 (13.0)	25.0 (2.5)	12.3 (1.2)	44.0 (5.3)	1.5 (0.2)
	05-10	97.1 (9.7)	102.3 (10.3)	20.6 (2.1)	10.2 (1.0)	35.2 (4.2)	1.2 (0.2)
	10-20	73.4 (7.4)	77.0 (7.7)	14.8 (1.5)	7.5 (0.7)	26.1 (3.1)	0.9 (0.1)
	20-30	49.5 (4.9)	52.0 (5.2)	9.6 (1.0)	4.9 (0.5)	17.8 (2.1)	0.7 (0.1)
	30-40	33.9 (3.4)	35.7 (3.6)	6.1 (0.6)	3.2 (0.3)	11.8 (1.4)	0.5 (0.1)
	40-50	21.3 (2.1)	22.5 (2.3)	3.7 (0.4)	1.9 (0.2)	7.3 (0.9)	0.33 (0.04)
	50-60	12.9 (1.3)	13.6 (1.4)	1.9 (0.2)	1.0 (0.1)	4.2 (0.5)	0.21 (0.03)
	60-70	7.6 (0.8)	7.9 (0.8)	0.98 (0.09)	0.53 (0.05)	2.1 (0.3)	0.13 (0.02)
	70-80	3.9 (0.4)	4.2 (0.4)	0.46 (0.05)	0.25 (0.03)	1.0 (0.1)	0.07 (0.01)
19.6	00-05	161.4 (17.8)	165.8 (18.3)	29.6 (2.9)	18.8 (1.9)	34.2 (4.5)	4.2 (0.5)
	05-10	130.3 (14.4)	133.7 (14.7)	24.3 (2.4)	15.5 (1.6)	29.3 (3.8)	3.4 (0.4)
	10-20	99.3 (10.9)	102.1 (11.3)	18.0 (1.8)	11.6 (1.2)	21.9 (2.9)	2.7 (0.4)
	20-30	67.1 (7.4)	68.8 (7.6)	12.3 (1.2)	7.9 (0.8)	14.6 (1.9)	1.9 (0.3)
	30-40	44.8 (4.9)	46.0 (5.1)	7.8 (0.8)	5.2 (0.5)	9.2 (1.2)	1.4 (0.2)
	40-50	28.1 (3.1)	28.9 (3.2)	4.7 (0.5)	3.2 (0.3)	5.8 (0.8)	0.95 (0.1)
	50-60	17.1 (1.9)	17.6 (1.9)	2.7 (0.3)	1.8 (0.2)	3.3 (0.4)	0.6 (0.1)
	60-70	9.5 (1.0)	9.7 (1.1)	1.3 (0.1)	0.9 (0.1)	1.8 (0.2)	0.35 (0.05)
	70-80	5.0 (0.6)	5.2 (0.6)	0.65 (0.06)	0.45 (0.04)	0.8 (0.1)	0.18 (0.02)
27	00-05	172.9 (19.1)	177.1 (19.5)	31.1 (2.8)	22.6 (2.0)	31.7 (3.8)	6.0 (0.7)
	05-10	144.3 (15.9)	147.5 (16.3)	25.8 (2.3)	18.7 (1.7)	26.5 (3.2)	5.1 (0.6)
	10-20	109.4 (12.1)	111.6 (12.3)	19.4 (1.8)	14.5 (1.3)	19.4 (2.3)	4.0 (0.5)
	20-30	74.3 (8.2)	75.9 (8.4)	12.9 (1.2)	9.8 (0.9)	12.9 (1.5)	2.9 (0.3)
	30-40	48.8 (5.4)	49.9 (5.5)	8.3 (0.8)	6.2 (0.6)	8.9 (1.1)	2.0 (0.2)
	40-50	30.7 (3.4)	31.5 (3.5)	5.2 (0.5)	3.9 (0.3)	5.6 (0.7)	1.4 (0.2)
	50-60	18.6 (2.0)	18.9 (2.1)	2.9 (0.3)	2.2 (0.2)	3.2 (0.4)	0.8 (0.1)
	60-70	10.4 (1.1)	10.6 (1.2)	1.5 (0.1)	1.1 (0.1)	1.7 (0.2)	0.49 (0.05)
	70-80	5.1 (0.6)	5.3 (0.6)	0.68 (0.06)	0.51 (0.05)	0.8 (0.1)	0.23 (0.03)
39	00-05	182.3 (20.1)	185.8 (20.5)	32.0 (2.9)	25.0 (2.3)	26.5 (2.9)	8.5 (1.0)
	05-10	151.4 (16.7)	155.0 (17.1)	27.0 (2.4)	21.0 (1.9)	22.7 (2.5)	7.4 (0.9)
	10-20	115.9 (12.8)	118.4 (13.1)	20.3 (1.8)	15.9 (1.4)	17.3 (1.9)	5.4 (0.7)
	20-30	78.9 (8.7)	80.7 (8.9)	13.6 (1.2)	10.7 (1.0)	11.9 (1.3)	3.9 (0.5)
	30-40	51.8 (5.7)	52.9 (5.8)	8.8 (0.8)	7.0 (0.6)	7.9 (0.9)	2.8 (0.3)
	40-50	32.9 (3.6)	33.7 (3.7)	5.4 (0.5)	4.4 (0.4)	4.9 (0.5)	1.8 (0.2)
	50-60	20.1 (2.2)	20.6 (2.2)	3.2 (0.3)	2.6 (0.2)	2.9 (0.3)	1.2 (0.1)
	60-70	11.0 (1.2)	11.3 (1.2)	1.6 (0.1)	1.3 (0.1)	1.5 (0.2)	0.64 (0.08)
	70-80	5.9 (0.7)	6.1 (0.7)	0.8 (0.07)	0.7 (0.1)	0.7 (0.1)	0.33 (0.04)

TABLE VII: Extracted average transverse momentum $\langle p_T \rangle$ values for for $|y| < 0.1$ in Au+Au collisions at $\sqrt{s_{NN}} = 7.7, 11.5, 19.6, 27,$ and 39 GeV. Quoted errors in parenthesis are the combined statistical and systematic uncertainties.

$\sqrt{s_{NN}}$ (GeV)	% cross-section	π^+	π^-	K^+	K^-	p	\bar{p}
7.7 GeV	00–05	0.385 (0.019)	0.376 (0.019)	0.576 (0.024)	0.539 (0.022)	0.797 (0.064)	0.779 (0.055)
	05–10	0.381 (0.019)	0.373 (0.019)	0.563 (0.023)	0.532 (0.022)	0.764 (0.061)	0.770 (0.054)
	10–20	0.380 (0.019)	0.373 (0.019)	0.552 (0.023)	0.521 (0.021)	0.754 (0.060)	0.722 (0.051)
	20–30	0.374 (0.019)	0.368 (0.019)	0.533 (0.022)	0.506 (0.021)	0.745 (0.060)	0.702 (0.049)
	30–40	0.368 (0.019)	0.363 (0.018)	0.528 (0.022)	0.499 (0.021)	0.699 (0.056)	0.657 (0.046)
	40–50	0.357 (0.018)	0.354 (0.018)	0.505 (0.021)	0.470 (0.019)	0.659 (0.053)	0.608 (0.043)
	50–60	0.346 (0.018)	0.344 (0.017)	0.485 (0.020)	0.460 (0.019)	0.617 (0.050)	0.567 (0.040)
	60–70	0.339 (0.017)	0.335 (0.017)	0.472 (0.019)	0.438 (0.018)	0.585 (0.047)	0.541 (0.038)
	70–80	0.325 (0.016)	0.326 (0.017)	0.457 (0.019)	0.427 (0.018)	0.520 (0.042)	0.486 (0.034)
11.5 GeV	00–05	0.389 (0.020)	0.382 (0.019)	0.585 (0.030)	0.556 (0.028)	0.798 (0.056)	0.798 (0.064)
	05–10	0.387 (0.020)	0.380 (0.019)	0.572 (0.029)	0.551 (0.028)	0.794 (0.056)	0.781 (0.063)
	10–20	0.385 (0.020)	0.380 (0.019)	0.564 (0.029)	0.540 (0.028)	0.766 (0.054)	0.757 (0.061)
	20–30	0.384 (0.019)	0.379 (0.019)	0.557 (0.028)	0.532 (0.027)	0.755 (0.053)	0.726 (0.059)
	30–40	0.379 (0.019)	0.375 (0.019)	0.550 (0.028)	0.527 (0.027)	0.717 (0.050)	0.688 (0.055)
	40–50	0.372 (0.019)	0.368 (0.019)	0.526 (0.027)	0.503 (0.026)	0.670 (0.047)	0.644 (0.052)
	50–60	0.362 (0.018)	0.360 (0.018)	0.512 (0.027)	0.489 (0.025)	0.636 (0.045)	0.595 (0.048)
	60–70	0.351 (0.018)	0.351 (0.018)	0.495 (0.026)	0.474 (0.024)	0.600 (0.042)	0.559 (0.045)
	70–80	0.343 (0.017)	0.343 (0.017)	0.480 (0.025)	0.447 (0.023)	0.568 (0.040)	0.526 (0.042)
19.6 GeV	00–05	0.397 (0.024)	0.392 (0.024)	0.590 (0.036)	0.571 (0.035)	0.812 (0.049)	0.834 (0.076)
	05–10	0.395 (0.024)	0.391 (0.024)	0.578 (0.035)	0.562 (0.034)	0.811 (0.049)	0.810 (0.073)
	10–20	0.395 (0.024)	0.391 (0.024)	0.575 (0.035)	0.559 (0.034)	0.787 (0.047)	0.789 (0.071)
	20–30	0.390 (0.024)	0.388 (0.023)	0.565 (0.034)	0.543 (0.033)	0.772 (0.047)	0.758 (0.069)
	30–40	0.385 (0.023)	0.383 (0.023)	0.557 (0.034)	0.537 (0.033)	0.733 (0.044)	0.732 (0.066)
	40–50	0.380 (0.023)	0.379 (0.023)	0.533 (0.032)	0.519 (0.032)	0.700 (0.042)	0.692 (0.063)
	50–60	0.370 (0.022)	0.373 (0.023)	0.520 (0.032)	0.501 (0.030)	0.659 (0.040)	0.647 (0.059)
	60–70	0.360 (0.022)	0.366 (0.022)	0.502 (0.031)	0.483 (0.029)	0.637 (0.038)	0.610 (0.055)
	70–80	0.352 (0.021)	0.354 (0.021)	0.490 (0.030)	0.469 (0.029)	0.599 (0.036)	0.577 (0.052)
27 GeV	00–05	0.409 (0.025)	0.407 (0.025)	0.603 (0.037)	0.581 (0.035)	0.841 (0.051)	0.838 (0.076)
	05–10	0.406 (0.025)	0.403 (0.024)	0.596 (0.036)	0.575 (0.035)	0.836 (0.050)	0.833 (0.075)
	10–20	0.404 (0.024)	0.399 (0.024)	0.594 (0.036)	0.567 (0.035)	0.787 (0.047)	0.810 (0.073)
	20–30	0.401 (0.024)	0.396 (0.024)	0.586 (0.036)	0.556 (0.034)	0.755 (0.046)	0.777 (0.070)
	30–40	0.400 (0.024)	0.393 (0.024)	0.575 (0.035)	0.553 (0.034)	0.742 (0.045)	0.723 (0.065)
	40–50	0.393 (0.024)	0.385 (0.023)	0.553 (0.034)	0.535 (0.033)	0.726 (0.044)	0.696 (0.063)
	50–60	0.380 (0.023)	0.378 (0.023)	0.547 (0.033)	0.524 (0.032)	0.666 (0.040)	0.678 (0.061)
	60–70	0.372 (0.023)	0.368 (0.022)	0.523 (0.032)	0.506 (0.031)	0.631 (0.038)	0.627 (0.057)
	70–80	0.363 (0.022)	0.362 (0.022)	0.505 (0.031)	0.488 (0.030)	0.589 (0.036)	0.588 (0.053)
39 GeV	00–05	0.417 (0.025)	0.413 (0.025)	0.613 (0.037)	0.608 (0.037)	0.860 (0.052)	0.867 (0.096)
	05–10	0.414 (0.025)	0.410 (0.025)	0.610 (0.037)	0.599 (0.036)	0.838 (0.051)	0.842 (0.093)
	10–20	0.411 (0.025)	0.408 (0.025)	0.607 (0.037)	0.597 (0.036)	0.828 (0.050)	0.832 (0.092)
	20–30	0.408 (0.025)	0.405 (0.025)	0.599 (0.036)	0.588 (0.036)	0.812 (0.049)	0.799 (0.088)
	30–40	0.405 (0.025)	0.403 (0.024)	0.590 (0.036)	0.580 (0.035)	0.766 (0.046)	0.776 (0.086)
	40–50	0.400 (0.024)	0.394 (0.024)	0.569 (0.035)	0.562 (0.034)	0.750 (0.045)	0.739 (0.082)
	50–60	0.389 (0.024)	0.387 (0.023)	0.559 (0.034)	0.548 (0.033)	0.704 (0.042)	0.691 (0.076)
	60–70	0.379 (0.023)	0.378 (0.023)	0.548 (0.033)	0.534 (0.032)	0.665 (0.040)	0.654 (0.072)
	70–80	0.370 (0.022)	0.370 (0.022)	0.537 (0.033)	0.518 (0.031)	0.633 (0.038)	0.617 (0.068)

TABLE VIII: Extracted chemical freeze-out parameters for Grand Canonical Ensemble using both yield (GCEY) and ratio (GCER) fits at different centralities in Au+Au collisions at $\sqrt{s_{NN}} = 7.7, 11.5, 19.6, 27, 39, 62.4$, and 200 GeV. Errors in parenthesis are systematic uncertainties.

$\sqrt{s_{NN}}$ (GeV)	% cross section	T_{ch} (MeV)		μ_B (MeV)		μ_S (MeV)		γ_S		R (fm)	χ^2/NDF	
		GCER	GCEY	GCER	GCEY	GCER	GCEY	GCER	GCEY	GCEY	GCER	GCEY
7.7	00–05	144.3 (4.8)	143.8 (2.7)	398.2 (16.4)	399.8 (13.3)	89.5 (6.0)	90.2 (7.6)	0.95 (0.08)	1.05 (0.06)	5.89 (0.33)	1.4	1.3
	05–10	143.0 (4.7)	142.9 (2.6)	393.5 (15.6)	395.6 (13.0)	88.5 (5.7)	89.8 (7.5)	0.95 (0.08)	1.04 (0.06)	5.65 (0.31)	1.2	1.0
	10–20	143.8 (4.6)	144.7 (2.6)	388.0 (14.9)	391.6 (12.1)	86.4 (5.4)	87.1 (7.0)	0.88 (0.07)	0.95 (0.05)	5.08 (0.27)	0.9	1.1
	20–30	143.5 (4.5)	144.9 (2.6)	379.5 (14.4)	382.4 (11.8)	85.2 (5.2)	85.7 (7.0)	0.85 (0.07)	0.88 (0.05)	4.58 (0.24)	0.6	1.0
	30–40	145.9 (4.9)	146.2 (2.8)	375.4 (15.3)	376.1 (12.9)	85.5 (5.7)	87.6 (7.4)	0.78 (0.07)	0.82 (0.05)	3.95 (0.22)	0.9	0.6
	40–60	144.7 (4.7)	145.5 (2.7)	355.6 (13.9)	357.8 (12.0)	80.3 (5.2)	82.2 (7.0)	0.68 (0.06)	0.71 (0.04)	3.28 (0.17)	0.7	0.9
	60–80	143.4 (4.7)	143.3 (2.8)	337.5 (13.7)	337.8 (12.0)	79.3 (5.5)	79.5 (8.0)	0.47 (0.04)	0.49 (0.03)	2.40 (0.13)	1.0	0.7
11.5	00–05	149.4 (5.2)	150.6 (3.2)	287.3 (12.5)	292.5 (12.6)	64.5 (4.7)	66.0 (7.6)	0.92 (0.09)	1.00 (0.06)	6.16 (0.36)	1.0	1.1
	05–10	150.1 (5.4)	150.5 (3.2)	288.9 (12.9)	294.6 (13.1)	65.8 (4.9)	70.0 (7.8)	0.96 (0.09)	1.04 (0.06)	5.69 (0.34)	1.4	1.3
	10–20	151.8 (5.4)	153.1 (3.2)	284.9 (12.7)	291.6 (12.4)	65.1 (4.9)	68.6 (7.7)	0.92 (0.09)	0.98 (0.06)	5.02 (0.30)	1.2	1.3
	20–30	153.5 (5.7)	155.9 (3.4)	278.7 (12.8)	283.6 (12.3)	63.9 (5.0)	65.6 (7.5)	0.85 (0.08)	0.88 (0.05)	4.31 (0.27)	0.7	1.2
	30–40	154.6 (5.8)	156.9 (3.6)	270.1 (12.8)	273.8 (12.7)	61.9 (5.0)	62.9 (7.6)	0.78 (0.08)	0.82 (0.05)	3.76 (0.24)	0.7	1.2
	40–60	155.3 (5.9)	157.9 (3.7)	256.0 (12.4)	259.2 (12.6)	60.2 (5.0)	62.5 (7.6)	0.69 (0.07)	0.71 (0.04)	3.02 (0.19)	0.7	1.3
	60–80	151.6 (5.4)	154.3 (3.5)	227.3 (10.8)	229.4 (12.2)	54.6 (4.4)	54.6 (7.6)	0.52 (0.05)	0.54 (0.03)	2.26 (0.14)	0.5	0.8
19.6	00–05	153.9 (5.2)	157.5 (3.1)	187.9 (8.6)	195.6 (9.7)	43.2 (3.8)	45.3 (6.3)	0.96 (0.09)	1.09 (0.05)	6.04 (0.35)	1.3	1.9
	05–10	154.2 (5.3)	158.0 (3.2)	187.2 (8.6)	193.9 (9.7)	43.9 (3.8)	45.8 (6.3)	0.95 (0.09)	1.05 (0.05)	5.67 (0.33)	0.9	1.4
	10–20	155.9 (5.6)	159.8 (3.3)	184.9 (8.8)	193.9 (9.7)	44.4 (3.9)	48.1 (6.2)	0.92 (0.09)	1.00 (0.05)	5.08 (0.30)	1.0	1.4
	20–30	156.4 (5.7)	160.6 (3.3)	177.2 (8.5)	184.9 (9.0)	42.6 (3.7)	45.5 (5.6)	0.91 (0.09)	0.95 (0.04)	4.49 (0.27)	0.7	1.2
	30–40	157.5 (5.9)	161.6 (3.4)	166.9 (8.5)	173.3 (9.3)	40.3 (3.7)	42.4 (5.7)	0.85 (0.08)	0.87 (0.04)	3.93 (0.24)	0.7	1.2
	40–60	157.9 (6.0)	162.72(3.5)	154.4 (8.2)	159.4 (9.8)	38.0 (3.8)	40.1 (6.3)	0.77 (0.08)	0.76 (0.04)	3.19 (0.19)	0.4	1.2
	60–80	156.2 (5.9)	159.6 (3.6)	133.7 (7.7)	134.6 (10.4)	33.3 (3.6)	32.9 (6.4)	0.61 (0.06)	0.60 (0.03)	2.33 (0.14)	0.3	0.9
27.0	00–05	155.0 (5.1)	159.8 (3.0)	144.4 (7.2)	151.9 (9.3)	33.5 (3.6)	36.7 (6.0)	0.98 (0.10)	1.09 (0.05)	6.05 (0.33)	1.3	1.7
	05–10	155.6 (5.2)	160.4 (3.1)	143.9 (7.2)	151.6 (9.3)	34.1 (3.6)	37.6 (6.0)	0.96 (0.10)	1.07 (0.05)	5.67 (0.31)	1.3	1.7
	10–20	155.8 (5.2)	160.7 (3.0)	137.7 (7.0)	146.3 (8.8)	32.0 (3.6)	36.3 (5.8)	0.96 (0.09)	1.03 (0.05)	5.22 (0.29)	1.2	1.6
	20–30	157.1 (5.4)	162.7 (3.1)	131.0 (6.9)	140.6 (8.3)	31.0 (3.5)	35.8 (5.4)	0.94 (0.09)	0.97 (0.04)	4.53 (0.25)	1.2	1.7
	30–40	158.9 (5.7)	164.7 (3.4)	130.3 (7.2)	137.4 (9.1)	32.4 (3.6)	35.9 (5.6)	0.88 (0.09)	0.89 (0.04)	3.89 (0.23)	1.0	1.4
	40–60	160.4 (5.9)	165.5 (3.5)	120.4 (7.1)	127.5 (8.9)	31.4 (3.6)	34.9 (5.7)	0.81 (0.08)	0.79 (0.03)	3.13 (0.18)	0.6	1.2
	60–80	158.3 (5.8)	163.1 (3.9)	105.8 (6.8)	105.2 (9.5)	28.6 (3.4)	27.4 (5.9)	0.65 (0.07)	0.62 (0.03)	2.27 (0.15)	0.4	1.5
39.0	00–05	156.4 (5.7)	159.9 (3.5)	103.2 (7.4)	104.7 (11.2)	24.5 (3.8)	23.8 (8.1)	0.94 (0.10)	1.05 (0.07)	6.27 (0.39)	0.9	1.6
	05–10	157.0 (5.9)	160.3 (3.4)	101.9 (7.2)	103.1 (10.9)	24.8 (3.7)	23.9 (7.8)	0.94 (0.10)	1.03 (0.07)	5.92 (0.35)	0.7	1.2
	10–20	156.3 (5.7)	160.9 (3.4)	101.9 (6.9)	103.8 (10.5)	24.9 (3.7)	25.3 (7.3)	0.94 (0.09)	1.02 (0.06)	5.35 (0.31)	0.8	1.5
	20–30	157.9 (5.9)	162.6 (3.4)	98.2 (6.7)	100.5 (10.1)	24.9 (3.6)	25.8 (6.5)	0.92 (0.09)	0.97 (0.05)	4.65 (0.27)	0.8	1.4
	30–40	160.8 (6.4)	164.8 (3.6)	94.2 (6.6)	95.8 (10.3)	24.0 (3.7)	24.7 (6.9)	0.87 (0.09)	0.90 (0.05)	3.99 (0.24)	0.5	0.9
	40–60	160.0 (6.4)	163.5 (3.5)	84.6 (6.6)	86.8 (9.9)	21.9 (3.6)	23.2 (6.7)	0.82 (0.08)	0.83 (0.04)	3.29 (0.19)	0.4	1.1
	60–80	158.3 (6.2)	160.4 (3.4)	73.0 (6.5)	71.9 (10.0)	20.3 (3.5)	20.3 (6.5)	0.67 (0.07)	0.67 (0.03)	2.41 (0.14)	0.3	1.1
62.4	00–05	160.3 (4.9)	164.3 (3.6)	69.8 (5.6)	69.2 (11.4)	16.7 (3.3)	15.8 (6.8)	0.86 (0.06)	0.91 (0.05)	6.62 (0.36)	2.1	3.7
	05–10	158.4 (4.4)	160.0 (3.2)	66.1 (5.3)	63.8 (9.9)	15.7 (3.4)	16.1 (6.8)	0.87 (0.06)	0.91 (0.05)	6.62 (0.34)	1.7	2.9
	10–20	159.0 (4.3)	161.4 (3.1)	65.4 (5.2)	63.7 (9.3)	15.4 (3.3)	13.6 (6.3)	0.84 (0.06)	0.92 (0.05)	5.84 (0.29)	1.8	3.4
	20–40	159.8 (4.2)	161.7 (2.9)	60.7 (5.2)	58.9 (9.1)	15.3 (3.2)	13.7 (6.3)	0.84 (0.06)	0.91 (0.05)	4.86 (0.24)	2.1	3.1
	40–60	158.1 (4.3)	160.1 (2.8)	54.1 (5.2)	53.7 (8.0)	12.1 (3.2)	10.1 (6.3)	0.76 (0.06)	0.84 (0.04)	3.72 (0.19)	1.8	3.8
	60–80	157.4 (4.2)	161.7 (2.9)	44.6 (5.9)	45.4 (8.3)	10.3 (3.2)	11.5 (6.2)	0.69 (0.05)	0.74 (0.04)	2.49 (0.13)	1.6	4.1
	60–80	157.4 (4.2)	161.7 (2.9)	44.6 (5.9)	45.4 (8.3)	10.3 (3.2)	11.5 (6.2)	0.69 (0.05)	0.74 (0.04)	2.49 (0.13)	1.6	4.1
200	00–05	164.3 (5.3)	167.8 (4.2)	28.4 (5.8)	27.0 (11.4)	5.6 (3.9)	5.6 (6.8)	0.93 (0.08)	0.95 (0.06)	7.13 (0.46)	1.2	2.7
	05–10	163.5 (4.5)	168.5 (4.0)	28.4 (5.5)	25.7 (10.9)	5.0 (3.6)	4.2 (6.8)	0.95 (0.08)	0.97 (0.05)	6.50 (0.41)	1.4	2.9
	10–20	162.4 (4.4)	167.8 (3.8)	27.7 (5.1)	23.2 (10.2)	5.9 (3.2)	3.0 (6.3)	0.94 (0.07)	0.99 (0.05)	5.91 (0.35)	2.0	3.9
	20–30	163.9 (4.3)	167.5 (3.5)	27.4 (4.9)	23.3 (9.5)	6.4 (2.9)	4.1 (6.3)	0.90 (0.06)	0.95 (0.04)	5.28 (0.29)	1.8	3.4
	30–40	161.6 (3.9)	165.9 (3.5)	23.9 (4.8)	21.5 (9.7)	6.0 (3.1)	5.6 (6.3)	0.90 (0.06)	0.93 (0.04)	4.73 (0.26)	1.9	3.2
	40–60	162.3 (3.9)	165.8 (3.3)	22.9 (4.9)	21.3 (9.2)	5.8 (3.2)	4.8 (6.3)	0.84 (0.06)	0.88 (0.04)	3.85 (0.21)	1.2	2.0
	60–80	161.3 (3.8)	163.6 (3.2)	18.2 (4.5)	18.0 (8.9)	5.4 (3.3)	6.3 (6.2)	0.76 (0.05)	0.76 (0.03)	2.81 (0.14)	0.7	1.1

TABLE IX: Extracted chemical freeze-out parameters for Strangeness Canonical Ensemble using both ratio (SCER) and yield (SCEY) fit at different centralities in Au+Au collisions at $\sqrt{s_{NN}} = 7.7, 11.5, 19.6, 27, 39, 62.4$, and 200 GeV. Errors in parenthesis are systematic uncertainties.

$\sqrt{s_{NN}}$ (GeV)	% cross section	T_{ch} (MeV)		μ_B (MeV)		γ_S		R (fm)	χ^2/NDF	
		SCER	SCEY	SCER	SCEY	SCER	SCEY	SCEY	SCER	SCEY
7.7	00–05	143.9 (2.0)	143.5 (2.2)	397.5 (8.9)	400.1 (13.2)	0.97 (0.07)	1.08 (0.06)	5.92 (0.29)	1.4	1.0
	05–10	144.2 (2.1)	143.2 (2.2)	397.7 (8.8)	395.9 (13.1)	0.95 (0.07)	1.05 (0.06)	5.62 (0.28)	1.2	0.9
	10–20	144.6 (2.0)	144.3 (2.1)	390.8 (8.4)	391.8 (12.0)	0.89 (0.06)	0.98 (0.05)	5.11 (0.23)	0.9	0.9
	20–30	146.0 (1.9)	145.2 (2.1)	387.3 (8.0)	383.0 (11.9)	0.84 (0.05)	0.91 (0.05)	4.55 (0.21)	0.7	0.8
	30–40	148.4 (2.3)	147.5 (2.4)	383.0 (8.8)	377.6 (13.1)	0.78 (0.06)	0.84 (0.04)	3.85 (0.20)	0.9	0.6
	40–60	150.4 (2.4)	147.7 (2.5)	371.7 (8.7)	361.0 (12.3)	0.68 (0.05)	0.76 (0.04)	3.13 (0.16)	0.9	0.8
	60–80	156.9 (3.2)	147.6 (3.0)	376.5 (10.2)	347.4 (12.3)	0.48 (0.04)	0.65 (0.04)	2.19 (0.13)	2.6	1.5
11.5	00–05	152.7 (2.4)	151.0 (2.7)	294.6 (7.1)	291.7 (12.5)	0.90 (0.07)	1.0 (0.06)	6.12 (0.33)	1.1	0.9
	05–10	153.2 (2.9)	151.8 (2.9)	295.8 (9.2)	292.7 (13.1)	0.94 (0.08)	1.03 (0.06)	5.58 (0.32)	1.5	1.2
	10–20	154.3 (2.9)	153.6 (2.8)	290.4 (9.0)	290.6 (12.3)	0.91 (0.07)	0.99 (0.05)	4.97 (0.28)	1.2	1.1
	20–30	155.9 (3.0)	155.9 (2.9)	283.6 (9.0)	283.8 (12.1)	0.84 (0.06)	0.90 (0.05)	4.31 (0.23)	0.7	0.9
	30–40	157.2 (2.6)	157.0 (3.1)	275.5 (7.5)	274.6 (12.6)	0.79 (0.06)	0.85 (0.05)	3.75 (0.21)	0.7	0.9
	40–60	160.8 (3.5)	159.6 (3.4)	266.5 (9.3)	259.7 (12.8)	0.69 (0.06)	0.76 (0.04)	2.91 (0.18)	0.9	0.9
	60–80	166.1 (3.9)	158.8 (3.6)	254.3 (9.8)	233.2 (12.4)	0.54 (0.05)	0.71 (0.04)	2.05 (0.13)	2.2	1.3
19.6	00–05	158.6 (3.5)	157.6 (2.8)	192.9 (8.2)	194.2 (8.4)	0.91 (0.07)	1.1 (0.05)	6.03 (0.33)	1.3	1.6
	05–10	159.8 (3.7)	158.3 (2.9)	193.3 (8.3)	191.7 (8.4)	0.89 (0.07)	1.06 (0.05)	5.64 (0.31)	1.0	1.1
	10–20	161.9 (4.0)	160.6 (3.0)	191.3 (9.2)	190.3 (8.7)	0.87 (0.07)	1.00 (0.04)	5.01 (0.29)	1.1	1.3
	20–30	162.8 (3.8)	161.4 (3.0)	183.5 (8.3)	181.8 (8.2)	0.85 (0.07)	0.96 (0.04)	4.42 (0.24)	0.9	1.0
	30–40	163.9 (4.0)	162.4 (3.1)	172.8 (8.3)	170.6 (8.4)	0.81 (0.06)	0.90 (0.04)	3.86 (0.22)	0.8	1.0
	40–60	165.7 (4.6)	163.3 (3.4)	161.2 (8.4)	155.1 (8.6)	0.74 (0.06)	0.81 (0.04)	3.1 (0.19)	0.8	0.9
	60–80	167.6 (4.9)	161.7 (3.6)	142.8 (8.4)	129.1 (8.7)	0.62 (0.06)	0.76 (0.04)	2.19 (0.14)	1.3	0.7
27.0	00–05	159.0 (4.1)	160.0 (2.9)	146.6 (7.4)	149.1 (7.5)	0.94 (0.08)	1.1 (0.05)	6.03 (0.32)	1.5	1.4
	05–10	160.2 (4.2)	160.8 (3.0)	146.5 (7.5)	147.9 (7.7)	0.92 (0.08)	1.08 (0.05)	5.64 (0.30)	1.6	1.4
	10–20	159.6 (4.2)	161.1 (3.0)	139.5 (7.3)	142.5 (7.1)	0.93 (0.08)	1.04 (0.05)	5.17 (0.28)	1.4	1.4
	20–30	161.4 (4.3)	163.3 (3.0)	132.8 (7.3)	136.4 (6.8)	0.90 (0.08)	0.98 (0.04)	4.48 (0.25)	1.4	1.5
	30–40	164.7 (4.6)	165.6 (3.3)	133.3 (7.7)	132.8 (7.6)	0.84 (0.07)	0.91 (0.04)	3.82 (0.22)	1.4	1.3
	40–60	167.7 (5.2)	166.8 (3.4)	123.7 (7.8)	120.4 (7.0)	0.76 (0.07)	0.84 (0.03)	3.04 (0.18)	1.2	1.1
	60–80	168.4 (5.5)	165.5 (3.8)	110.0 (7.8)	99.5 (7.6)	0.59 (0.05)	0.78 (0.03)	2.12 (0.14)	1.8	0.9
39.0	00–05	159.1 (4.9)	159.6 (3.4)	104.6 (8.4)	104.0 (9.6)	0.92 (0.09)	1.06 (0.07)	6.29 (0.38)	1.1	1.3
	05–10	160.2 (5.0)	160.2 (3.4)	103.3 (8.5)	102.0 (9.0)	0.91 (0.09)	1.04 (0.07)	5.93 (0.35)	0.9	0.9
	10–20	159.7 (4.8)	160.9 (3.3)	102.9 (8.3)	101.5 (8.4)	0.92 (0.08)	1.03 (0.06)	5.34 (0.31)	1.1	1.2
	20–30	162.1 (5.0)	162.9 (3.3)	99.0 (8.5)	96.4 (7.7)	0.89 (0.08)	0.98 (0.05)	4.63 (0.26)	1.2	1.2
	30–40	164.5 (4.7)	165.0 (3.5)	95.1 (8.5)	92.7 (7.9)	0.85 (0.07)	0.92 (0.05)	3.96 (0.23)	0.7	0.8
	40–60	164.0 (5.3)	164.1 (3.5)	85.3 (8.4)	82.3 (7.6)	0.81 (0.08)	0.87 (0.04)	3.24 (0.19)	0.8	0.9
	60–80	165.2 (5.5)	162.7 (3.6)	74.6 (8.1)	66.9 (7.9)	0.72 (0.08)	0.80 (0.04)	2.27 (0.14)	1.3	0.8
62.4	00–05	161.6 (4.4)	164.1 (3.6)	70.3 (5.7)	69.2 (10.9)	0.86 (0.06)	0.92 (0.05)	6.65 (0.36)	2.1	3.7
	05–10	159.5 (4.0)	160.0 (3.2)	66.4 (5.4)	62.6 (9.5)	0.87 (0.06)	0.92 (0.05)	6.63 (0.34)	1.8	2.9
	10–20	160.1 (3.9)	161.3 (3.0)	65.6 (5.3)	63.9 (8.8)	0.85 (0.05)	0.93 (0.05)	5.85 (0.29)	1.8	3.4
	20–40	161.3 (3.9)	161.7 (2.9)	61.0 (5.3)	58.5 (8.5)	0.84 (0.05)	0.92 (0.05)	4.85 (0.24)	2.2	3.1
	40–60	159.1 (4.0)	160.5 (2.9)	54.4 (5.2)	54.5 (7.4)	0.78 (0.06)	0.87 (0.05)	3.69 (0.19)	1.8	3.8
	60–80	159.3 (4.0)	164.0 (3.1)	45.6 (6.1)	45.8 (7.9)	0.73 (0.05)	0.84 (0.04)	2.37 (0.13)	1.9	4.1
200	00–05	163.8 (5.2)	167.6 (4.2)	28.9 (5.5)	28.1 (8.4)	0.94 (0.08)	0.95 (0.05)	7.15 (0.46)	0.9	2.2
	05–10	162.9 (4.8)	168.2 (4.0)	29.2 (5.1)	28.5 (7.9)	0.97 (0.08)	0.98 (0.05)	6.53 (0.41)	1.1	2.5
	10–20	162.2 (4.3)	167.4 (3.7)	27.8 (4.8)	26.9 (7.5)	0.95 (0.07)	0.99 (0.05)	5.94 (0.35)	1.6	3.2
	20–30	163.9 (4.2)	167.2 (3.5)	27.2 (4.6)	25.9 (6.6)	0.91 (0.06)	0.96 (0.04)	5.29 (0.29)	1.5	2.8
	30–40	161.8 (3.9)	165.8 (3.5)	23.6 (4.7)	20.7 (7.4)	0.91 (0.06)	0.94 (0.04)	4.73 (0.26)	1.6	2.6
	40–60	162.6 (3.8)	164.5 (3.5)	22.7 (4.9)	25.9 (8.1)	0.86 (0.06)	0.91 (0.04)	3.91 (0.21)	1.0	1.4
	60–80	162.2 (3.7)	164.1 (3.2)	17.4 (4.2)	15.3 (6.6)	0.80 (0.05)	0.83 (0.04)	2.76 (0.14)	0.8	0.9

TABLE X: Extracted kinetic freeze-out parameters in Au+Au collisions at $\sqrt{s_{NN}} = 7.7, 11.5, 19.6, 27,$ and 39 GeV. Quoted errors in parenthesis are the combined statistical and systematic uncertainties.

$\sqrt{s_{NN}}$ (GeV)	% cross-section	T_{kin} (MeV)	$\langle\beta\rangle c$	n	χ^2/NDF
7.7	00-05	116 (11)	0.462 (0.043)	0.5 (0.3)	0.52
	05-10	118 (11)	0.440 (0.048)	0.5 (0.3)	0.46
	10-20	121 (12)	0.403 (0.040)	0.8 (0.3)	0.39
	20-30	123 (12)	0.379 (0.040)	0.9 (0.3)	0.53
	30-40	129 (12)	0.348 (0.049)	0.8 (0.4)	0.61
	40-50	131 (12)	0.282 (0.044)	1.6 (0.6)	0.74
	50-60	139 (13)	0.205 (0.053)	2.0 (1.4)	1.25
	60-70	139 (13)	0.147 (0.020)	5.0 (4.8)	0.76
11.5	70-80	140 (13)	0.106 (0.035)	5.0 (3.4)	0.89
	00-05	118 (12)	0.464 (0.044)	0.5 (0.3)	0.26
	05-10	120 (12)	0.446 (0.046)	0.6 (0.3)	0.24
	10-20	120 (12)	0.423 (0.038)	0.9 (0.3)	0.23
	20-30	125 (13)	0.387 (0.037)	1.0 (0.3)	0.21
	30-40	133 (13)	0.363 (0.056)	0.8 (0.4)	0.22
	40-50	136 (13)	0.271 (0.034)	2.3 (0.5)	0.27
	50-60	139 (14)	0.207 (0.033)	4.1 (1.0)	0.33
19.6	60-70	139 (14)	0.172 (0.032)	5.0 (0.5)	0.32
	70-80	140 (14)	0.147 (0.032)	5.0 (0.3)	0.78
	00-05	113 (11)	0.458 (0.034)	0.9 (0.2)	0.19
	05-10	114 (12)	0.455 (0.033)	0.9 (0.2)	0.38
	10-20	117 (12)	0.435 (0.032)	1.1 (0.1)	0.30
	20-30	121 (12)	0.402 (0.030)	1.3 (0.2)	0.32
	30-40	123 (12)	0.360 (0.026)	1.7 (0.2)	0.40
	40-50	129 (13)	0.315 (0.024)	1.9 (0.2)	0.39
27.0	50-60	132 (13)	0.246 (0.026)	3.6 (0.4)	0.31
	60-70	135 (13)	0.196 (0.029)	5.0 (0.2)	0.51
	70-80	137 (14)	0.174 (0.028)	5.0 (0.2)	1.11
	00-05	117 (11)	0.482 (0.038)	0.6 (0.2)	0.33
	05-10	116 (11)	0.467 (0.026)	0.8 (0.2)	0.44
	10-20	120 (11)	0.452 (0.028)	0.8 (0.2)	0.46
	20-30	123 (12)	0.420 (0.028)	1.1 (0.2)	0.34
	30-40	131 (10)	0.381 (0.029)	1.2 (0.2)	0.28
39.0	40-50	133 (10)	0.324 (0.027)	2.0 (0.3)	0.22
	50-60	139 (10)	0.253 (0.028)	3.3 (0.6)	0.13
	60-70	141 (11)	0.200 (0.031)	5.0 (0.4)	0.17
	70-80	142 (11)	0.176 (0.029)	5.0 (0.3)	1.01
	00-05	117 (11)	0.492 (0.038)	0.7 (0.2)	0.18
	05-10	119 (11)	0.472 (0.036)	0.8 (0.2)	0.18
	10-20	120 (11)	0.456 (0.034)	1.0 (0.2)	0.15
	20-30	122 (11)	0.429 (0.036)	1.2 (0.2)	0.14
	30-40	129 (11)	0.394 (0.033)	1.4 (0.2)	0.11
	40-50	131 (12)	0.345 (0.031)	2.0 (0.3)	0.11
	50-60	138 (13)	0.277 (0.028)	3.1 (0.5)	0.10
	60-70	142 (12)	0.240 (0.023)	4.0 (0.6)	0.20
	70-80	143 (12)	0.208 (0.022)	5.0 (0.3)	0.39